

## LA-UR-15-25526

Approved for public release; distribution is unlimited.

Title: Crystalline and Crystalline International Disposal Activities

Author(s): Viswanathan, Hari S.  
Chu, Shaoping  
Reimus, Paul William  
Makedonska, Nataliia  
Hyman, Jeffrey De'Haven  
Karra, Satish  
Dittrich, Timothy M.

Intended for: Report

Issued: 2015-12-21 (rev.1)

---

**Disclaimer:**

Los Alamos National Laboratory, an affirmative action/equal opportunity employer, is operated by the Los Alamos National Security, LLC for the National Nuclear Security Administration of the U.S. Department of Energy under contract DE-AC52-06NA25396. By approving this article, the publisher recognizes that the U.S. Government retains nonexclusive, royalty-free license to publish or reproduce the published form of this contribution, or to allow others to do so, for U.S. Government purposes. Los Alamos National Laboratory requests that the publisher identify this article as work performed under the auspices of the U.S. Department of Energy. Los Alamos National Laboratory strongly supports academic freedom and a researcher's right to publish; as an institution, however, the Laboratory does not endorse the viewpoint of a publication or guarantee its technical correctness.

# ***Crystalline and Crystalline International Disposal Activities***

**Fuel Cycle Research & Development**

*Prepared for  
U.S. Department of Energy  
Used Fuel Disposition  
Hari Viswanathan,  
Shaoping Chu, Timothy Dittrich,  
Jeffrey Hyman, Satish Karra,  
Natallia Makendonska, Paul Reimus  
Los Alamos National Laboratory  
July 2015*

FCRD-UFD-2015-000602  
LA-UR-15-25526



**DISCLAIMER**

This information was prepared as an account of work sponsored by an agency of the U.S. Government. Neither the U.S. Government nor any agency thereof, nor any of their employees, makes any warranty, expressed or implied, or assumes any legal liability or responsibility for the accuracy, completeness, or usefulness, of any information, apparatus, product, or process disclosed, or represents that its use would not infringe privately owned rights. References herein to any specific commercial product, process, or service by trade name, trade mark, manufacturer, or otherwise, does not necessarily constitute or imply its endorsement, recommendation, or favoring by the U.S. Government or any agency thereof. The views and opinions of authors expressed herein do not necessarily state or reflect those of the U.S. Government or any agency thereof.

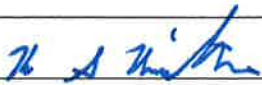
## FCT Quality Assurance Program Document

### Appendix E FCT Document Cover Sheet

Name/Title of Deliverable/Milestone LANL input to SNL L2 MS: Report entitled - "Crystalline and Crystalline International Disposal Activities"

Work Package Title and Number DR Crystalline Disposal R&D - LANL, FT-15LA080702

Work Package WBS Number 1.02.08.08

Responsible Work Package Manager Hari S. Viswanathan   
(Name/Signature)

Date Submitted July 2015

Quality Rigor Level for Deliverable/Milestone	<input type="checkbox"/> QRL-3	<input type="checkbox"/> QRL-2	<input type="checkbox"/> QRL-1 <input type="checkbox"/> Nuclear Data	<input checked="" type="checkbox"/> N/A*
---	--------------------------------	--------------------------------	---	--

This deliverable was prepared in accordance with Los Alamos National Laboratory  
(Participant/National Laboratory Name)

QA program which meets the requirements of  
 DOE Order 414.1       NQA-1-2000

**This Deliverable was subjected to:**

Technical Review

**Technical Review (TR)**

**Review Documentation Provided**

- Signed TR Report or,
- Signed TR Concurrence Sheet or,
- Signature of TR Reviewer(s) below

Name and Signature of Reviewers

Philip Stauffer 

Peer Review

**Peer Review (PR)**

**Review Documentation Provided**

- Signed PR Report or,
- Signed PR Concurrence Sheet or,
- Signature of PR Reviewer(s) below

\*Note: In some cases there may be a milestone where an item is being fabricated, maintenance is being performed on a facility, or a document is being issued through a formal document control process where it specifically calls out a formal review of the document. In these cases, documentation (e.g., inspection report, maintenance request, work planning package documentation or the documented review of the issued document through the document control process) of the completion of the activity along with the Document Cover Sheet is sufficient to demonstrate achieving the milestone. QRL for such milestones may be also be marked N/A in the work package provided the work package clearly specifies the requirement to use the Document Cover Sheet and provide supporting documentation.

This page left blank intentionally.

## CONTENTS

CONTENTS.....	v
FIGURES.....	vii
TABLES.....	xiii
EXECUTIVE SUMMARY.....	1-1
1. DEVELOPMENT AND DEMONSTRATION OF DISCRETE FRACTURE NETWORK MODEL.....	1-3
1.1 Introduction.....	1-3
1.2 DFNWORKS.....	1-3
1.2.1 Introduction.....	1-3
1.2.2 DFNWORKS Description.....	1-4
1.2.3 Remarks.....	1-16
1.3 Influence of Injection Mode.....	1-17
1.3.1 Introduction.....	1-17
1.3.2 Theory.....	1-19
1.3.3 Methods.....	1-20
1.3.4 Lagrangian Based Observations.....	1-24
1.3.5 Discussion.....	1-33
1.3.6 Conclusions.....	1-35
1.4 Effect of Internal Aperture Variability on Particle Tracking in DFN.....	1-36
1.4.1 Introduction.....	1-36
1.4.2 State of the Art.....	1-37
1.4.3 Results and Discussion.....	1-42
1.5 Concluding Remarks.....	1-48
1.6 References.....	1-48
2. LABORATORY INVESTIGATION OF COLLOID-FACILITATED TRANSPORT OF CESIUM BY BENTONITE COLLOIDS IN A CRYSTALLINE ROCK SYSTEM.....	2-1
2.1 Introduction.....	2-1
2.2 State of the Art.....	2-3
2.3 Technical Approaches (Materials and Methods).....	2-3
2.3.1 Groundwater.....	2-3
2.3.2 Geologic Media.....	2-4
2.3.3 Bentonite Colloids.....	2-7
2.3.4 Cesium and Tritiated Water.....	2-8
2.3.5 Analytical Measurements.....	2-9
2.3.6 Batch Experiments.....	2-9
2.3.7 Column Transport Experiments.....	2-10
2.3.8 Interpretive Modeling.....	2-11
2.4 Technical Results.....	2-14
2.4.1 Batch Experiment Results.....	2-14
2.4.2 Column Experiment Results.....	2-16
2.4.3 Implications for Repository Performance Assessments.....	2-24

2.5	Conclusions and Future Work.....	2-25
2.6	References.....	2-26



## FIGURES

- Figure 1-1. Sample fracture network and particle trajectories in a DFNWORKS simulation. The network is created and meshed using DFNGEN, which combines the feature rejection algorithm for meshing (Hyman et al. 2014) to stochastically generate three-dimensional DFNs on the basis of site specific data with the LAGRIT meshing toolbox to create a high resolution computational mesh representation of the DFN that conforms to the lines of intersections between fractures in an intrinsically parallel fashion. Constant pressure boundary conditions are applied to the left and right faces of the network to drive flow through the network, and steady-state conditions are determined by numerically integrating the governing flow equations using DFNFLOW, which utilizes the massively parallel subsurface flow and reactive transport code PFLOTTRAN. Transport through the DFN is simulated by adopting a Lagrangian approach within DFNTRANS, which is an extension of the of the WALKABOUT particle tracking method (Painter et al. 2012) to determine pathlines through the DFN. Particle trajectories, shown in orange and red, start from a short line source on a single fracture on the inlet plane and disperse from one another as they pass through the network, and exit the domain on numerous fractures..... 1-6
- Figure 1-2. DFNWORKS Workflow. From top: The input for DFNWORKS is a fractured site characterization that provides distributions of fracture orientations, radius, and spatial locations. DFNGEN: 1) FRAM - Create DFN: Using the fractured site characterization that networks are constructed using the feature rejection algorithm for meshing. 2) LAGRIT - Mesh DFN: The LAGRIT meshing tool box is used to create a conforming Delaunay triangulation of the network. DFNFLOW: 3) Convert Mesh to PFLOTTRAN input: Control volume information is formatted for pflotran. 4) Compute Pressure Solution: The steady-state pressure solution in the DFN is obtained using pflotran. dfnTrans: 5) Reconstruct Local Velocity Field: Darcy fluxes obtained using dfnFlow are used to reconstruct the local velocity field, which is used for particle tracking on the DFN. 6) Lagrangian Transport Simulation: An extension of the walkabout method is used to determine pathlines through the network and simulate transport..... 1-8
- Figure 1-3. Two fracture DFN demonstrating the utility of the DFNWORKS suite. (a) Conforming Delaunay mesh on the two fracture system. The fractures are colored by the distance of the computational cell from the line of intersection. Away from the intersection the mesh is coarsened to preserve computational resources. (b) Steady-state pressure solution, the gradient is aligned with the x-axis, and yellow lines are pressure contours. The pressure contours on the elliptical fracture show there is a pressure gradient and therefore flow is occurring on this dead-end fracture, it is not connect to the domain boundary (or another fracture other than principal fracture. (c) Fractures are colored by x coordinate of gradient of the pressure field, which is the fluid velocity in the x direction, and black lines are particle trajectories passing through the DFN. The non-uniformity of the trajectories results in a distribution of particle travel times that exhibits longitudinal dispersion. Using the simplifying pipe-network approximations, the breakthrough curve would be a step function with no dispersion or tail, which will lead to incorrect upscaled models for transport. .... 1-8
- Figure 1-4. Three intersecting fractures show the intersecting conforming Delaunay triangulations. Two of the fractures are colored by distance from lines of intersections (traces) between fractures, and the other is semi-transparent. The mesh is optionally coarsened away from intersections with pressure gradients will be lower. The inclusion

of the semi-transparent fracture illustrates how FRAM creates a mesh that adheres to multiple intersections on the surface of a single fracture. Two additional fractures intersect the elliptical fracture, and intersect one another on the surface of that fracture, as shown by the intersecting white colored regions. The inset shows that the Delaunay mesh conforms all of these lines of intersection.....1-10

Figure 1-5. Explicit grid format in PFLOTRAN that is used to read the DFN mesh.  $N$  is the number grid cells and  $M$  is the total number of internal connections between grid cells. In the first block under CELLS,  $idi$ ,  $x_i$ ,  $y_i$ ,  $z_i$  are the cell id,  $x$ -coordinate,  $y$ -coordinate and  $z$ -coordinate of the  $i$ -th grid cell, respectively. In the second block under CONNECTIONS,  $id_{up,j}$ ,  $id_{dn,j}$ ,  $x_j$ ,  $y_j$ ,  $z_j$ ,  $area_j$  are the upwind grid cell id of the  $j$ -th connection, downwind grid cell id of the  $j$ -th connection, Coordinates of the face between the  $j$ -th connection and the area of the face between the  $j$ -th connection, respectively.....1-11

Figure 1-6. Illustration of the technique used to reconstruct flow velocities along the line of intersection between two fractures. a) A control volume along a line of intersection between two fractures. Fluxes are defined on faces of the control volume cells. b) The control volume is spilt into four sub-polygons using the line of intersection. The green and orange sub-polygons are on one fracture and the blue and purple are on another. c) The flow velocities are reconstructed on each of the split polygons, here arrows indicate inflow/outflow. In this example, the flux into the control volume occurs through the purple sub-volume and outflow occurs through the remaining sub-polygons.....1-14

Figure 1-7. a) A DFN realization based upon the fractured granite at the Forsmark, Sweden site in a  $1 \text{ km}^3$  domain. The model consists of multiple sets of circular fractures whose orientations follow a Fisher distribution. The fracture diameters in each fracture set follow a truncated power-law distribution with lower cutoff at 15 meters. Fractures are colored by pressure. Dirichlet boundary conditions are imposed on the top (1 MPa) and bottom (2 MPa) of the domain to create a pressure gradient in the  $z$  direction, and no-flow boundary conditions are imposed along lateral boundaries. b) Two hundred particle trajectories within the DFN shown in Fig. 1-7. Particles are inserted uniformly along fractures on the bottom of the domain. Trajectories are overlaid on the networks shown in Fig. 1-7(a), but here fractures are colored by the permeability, to show how particles are drawn to larger fractures, which have higher permeabilities and offer less resistance than smaller fractures. Although particles are inserted uniformly along fractures in the inlet plane, they cluster on larger fractures as they exit the domain. This clustering suggests that transport only occurs within a small portion of the fracture network far away from the inlet plane. ....1-15

Figure 1-8. a) A DFN realization based upon the fractured granite at the Forsmark, Sweden site in a  $1 \text{ km}^3$  domain. The model consists of three sets of circular fractures whose orientations follow a Fisher distribution. The fracture diameters in each fracture set follow a truncated power-law distribution with lower cutoff at 15 m. Fractures are colored by permeability, which is based upon fracture radius. b) steady state pressure solution within the network shown in (a). Dirichlet boundary conditions are imposed on the top (1 MPa) and bottom (2 MPa) of the domain to create a pressure gradient in the  $z$  direction, and no-flow boundary conditions are imposed along lateral boundaries. ....1-23

Figure 1-9. Two hundred particle trajectories within the DFN shown in Fig. 1-8. Particles are inserted uniformly along fractures on the bottom of the domain. a) Trajectories are overlaid on Fig. 1-8.a, fractures are colored by the permeability, to show how particles

are drawn to larger fractures, which have higher permeabilities and offer less resistance than smaller fractures. Although particles are inserted uniformly along fractures in the inlet plane, they cluster on larger fractures as they exit the domain. This clustering suggests that transport only occurs within a small portion of the fracture network far away from the inlet plane. b) Trajectories with four example control planes, shown in grey. To quantify the visually observed clustering, particle attributes are recorded at uniformly spaced control planes throughout the domain..... 1-23

Figure 1-10. Heat map of mass distribution plotted as a function of fracture apertures (abscissa) and vertical distance traveled (ordinate) where colors indicate percent of particles for one realization. The primary direction of flow is from bottom, vertical distance equal to 0, to the top, vertical distance equal to 1000. (a) Resident injection: The initial distribution of mass is relatively uniform across all apertures, with slightly more weight at lower values due to larger numbers of small fractures in the network. As the particles move further through the domain, the bulk of the mass is drawn into fractures with larger apertures indicated by the trend of warmer colors up and right with increasing vertical distance traveled. (b) Flux-weighted injection: The initial distribution of mass is non-uniform across all apertures, with more mass being observed in fractures with larger apertures, compared to the resident injection. After traveling through a burn-in region, the distributions of mass for resident and flux-weighted injection resemble one another. .... 1-26

Figure 1-11. Heat map of mass distribution plotted as a function of fracture apertures (abscissa) and vertical distance traveled (ordinate) where colors indicate percent of particles for all realizations. The primary direction of flow is from bottom, vertical distance equal to 0, to top. (a) Resident injection: The initial distribution of mass favors small apertures due to their prevalence in the networks. As the particles move further through the domain, the bulk of the mass is drawn into fractures with larger apertures indicated by the observed trend up and right with increasing vertical distance traveled. (b) Flux-weighted injection: Compared to (a), more mass is initially placed into larger fractures due to the reduced resistance to flow, and higher flux, offered therein. As is the case in the resident injection, as the particle cloud moves through the domain, the majority of the mass migrates into the largest fractures in the networks. This clustering indicates large, fracture-to-fracture, flow channeling..... 1-26

Figure 1-12. (a) Mean particle tortuosity plotted as a function of control plane distance. Averages are computed using all particles in each DFN at each of the lower cutoffs for the generation of the DFN. Solid lines indicate particles inserted under resident injection conditions and dashed lines indicate flux-weighted values. Color indicates lower cutoff,  $r_0 = 15$ ; blue,  $r_0 = 20$ ; red,  $r_0 = 25$ ; green. The computed mean tortuosities using resident injection are consistently higher than those observed using flux-weighted injection. As the particle clouds move through the domain the difference between the two injection schemes decreases. (b) Box-dimension of particle cloud plotted as a function of control plane distance. Color indicates lower cutoff,  $r_0 = 15$ ; blue,  $r_0 = 20$ ; red,  $r_0 = 25$ ; green. Semi-transparent lines are individual realizations and thick line indicate average values. The network of fractures has a box-dimension of one at each of the control planes. The box-dimension of the particle clouds start at one because they are uniformly distributed along fractures on the inlet plane. At they move through the domain, the box-dimension decreases with distance and stabilizes to a mean value near 0.80, which indicates in-fracture clustering..... 1-28

- Figure 1-13. Cumulative distribution functions  $(t, z)$  of passage times. Line color indicate lower cutoffs,  $r_0 = 15$ ; blue,  $r_0 = 20$ ; red, and  $r_0 = 25$ ; green. Line style indicates CP,  $z = 100$ ; solid line,  $z = 750$ ; dashed line. Individual realizations are semi-transparent, and solid lines are average values. (a)  $(t, z)$  generated using resident based inject scheme. (b)  $(t, z)$  generated using flux-weighted injection scheme. The plotted values of  $(t, z)$ , are more homogeneous than  $(t, z)$  due to the majority of the mass transporting through larger fractures. .... 1-31
- Figure 1-14. Complement of the cumulative distribution function,  $1 - F(t, z)$ , of passage times. Line color indicate lower cutoffs,  $r_0 = 15$ ; blue,  $r_0 = 20$ ; red, and  $r_0 = 25$ ; green. Line style indicates CP,  $z = 100$ ; solid line,  $z = 750$ ; dashed line. Individual realizations are semi-transparent, and solid lines are average values. (a)  $1 - F_R(t, z)$  generated using resident based inject scheme. Universal power-law scaling is not observed. (b)  $1 - F_W(t, z)$  generated using flux-weighted injection scheme. It is possible that the tails demonstrate power-law scaling. The dotted black line is a power law with exponent two. The best fit for a power law in the tail of  $1 - F_W(t, 750)$  is a value of  $\approx 2.01$ . .... 1-31
- Figure 1-15. Mean travel time plotted as a function of longitudinal distance. Color indicates lower cutoff,  $r_0 = 15$ ; blue,  $r_0 = 20$ ; red,  $r_0 = 25$ ; green. Semi-transparent lines are individual realizations and thick lines are average values. (a) Resident injection mean travel times from inlet initially scale nonlinearly. After an initial distance, the mean travel time does scale linearly with distance. (b) Flux-weighted injection mean travel times scale linearly at all distances from the inlet. (c) Beyond a 250 meter burn-in region, mean travel times of particles inserted using resident injection scale linearly with distance. .... 1-32
- Figure 1-16.  $F_R(t, z^2, 250)$  and  $1 - F_R(t, z^2, 250)$  for particle travel time inserted using resident injection to account for a 250 meter burn-in region. Here, blue lines correspond to  $(t, 350, 250)$  and the red lines correspond  $(t, 1000, 250)$ . Line color indicate lower cutoffs,  $r_0 = 15$ ; blue,  $r_0 = 20$ ; red, and  $r_0 = 25$ ; green. Line style indicates CP,  $z = 100$ ; solid line,  $z = 750$ ; dashed line. Individual realizations are semi-transparent, and thick lines are ensemble values. These distances are selected so that the distance traveled from the burn-in plane is the same as those shown in Fig. 1-13.a. After accounting for the burn-in region, the general behavior of the curves is more similar to those observed for the flux-weighted injection displayed in Fig. 1-13.b, although some differences are still present. After applying this burn-in region, it is possible that these tails exhibit power law scaling, which is clearly impossible in Fig. 1-14.a. Averaging over all realizations, the best fit for a power-law tail of  $1 - F_R(t, 1000, 250)$  is  $\approx 1.94$ , which is remarkably close to the exponent observed under flux-weighted conditions. .... 1-33
- Figure 1-17. An example of one circular fracture with in-fracture variability. There are different spatial correlation lengths are applied: a)  $\lambda=0.1R$ , b)  $\lambda=0.3R$ , c)  $\lambda=0.5R$ , d)  $\lambda=0.7R$ . As correlation length increases, the zones of high and low aperture are observed clearer. .... 1-38
- Figure 1-18. Single fracture configuration with three cases of particle trajectories are shown for different applied variances of transmissivity (from left to right):  $\text{Var}_1(\sigma)$ ,  $\text{Var}_2(\sigma)$ , and  $\text{Var}_4(\sigma)$ , which correspond to 1, 2, and 4 orders of magnitude difference. Transmissivity distribution is shown by color patterns. Solid lines represent particles trajectories that are moving from bottom to top boundaries of the fracture. As variance in transmissivity increases the flow channeling is observed clearer, and the tortuosity of particles trajectories increases. .... 1-39

Figure 1-19. Example of steady state pressure solution in one of DFN realizations. The pressure boundary conditions are applied to top and bottom side of the domain, assuming fluid flow in vertical direction, from bottom to top. High pressure is shown by warm colors. ....	1-39
Figure 1-20. An example of DFN configuration with 4 cases of transmissivity distribution: a) transmissivity is constant along each fracture, but varies from fracture to fracture according to fracture size; b), c), d) show transmissivity distribution with $\text{Var}_2(\sigma)$ , $\text{Var}_4(\sigma)$ , and $\text{Var}_6(\sigma)$ , respectively.....	1-40
Figure 1-21. The cumulative and complementary cumulative distributions of calculated $\tau$ (top panel) and $\beta$ (bottom panel) are calculated for transport in reference case. ....	1-42
Figure 1-22. Cumulative and complementary cumulative distributions of $\tau$ for different variations of DFN transmissivity. Different correlation lengths, $\lambda$ , compared to the reference case, when no in-fracture variability is implied. ....	1-44
Figure 1-23. Cumulative and complementary cumulative distributions of $\beta$ for different variations of DFN transmissivity. Different correlation lengths, $\lambda$ , compared to the reference case, when no in-fracture variability is implied. ....	1-45
Figure 1-24. Cumulative and complementary cumulative distributions of $\tau$ for each considered correlation lengths, $\lambda$ . Different variations of DFN transmissivity are compared to the reference case, when no in-fracture variability is implied. ....	1-46
Figure 1-25. Cumulative and complementary cumulative distributions of $\beta$ for each considered correlation lengths, $\lambda$ . Different variations of DFN transmissivity are compared to the reference case, when no in-fracture variability is implied. ....	1-47
Figure 2-1. Batch adsorption $K_d$ values for $^{137}\text{Cs}$ on same bentonite colloids as used in this study in GTS groundwater as a function of Cs concentration (reproduced from Missana et al., 2004). ....	2-2
Figure 2-2. Microphotographs of crushed and sieved Grimsel granodiorite (left) and fracture fill material (right) in the 150-355 $\mu\text{m}$ size fraction (from Dittrich and Reimus, 2015 and Dittrich et al., 2015a). ....	2-5
Figure 2-3. Various steps in preparation of colloid suspension from FEBEX bentonite brick. ....	2-8
Figure 2-4. Particle size distribution of FEBEX bentonite colloid suspension as measured by a single particle counter. Note that the concentration scale on the y-axis does not account for sample dilution in the final suspension used in the experiments. ....	2-8
Figure 2-5. Photos of column experiment setup with three 1.5-cm-long columns running in parallel with syringe pumps, tubing, and fraction collector. ....	2-10
Figure 2-6. Results of batch adsorption experiment of $^{137}\text{Cs}$ onto FFM in SGW. 800 CPM/ml (starting concentration) corresponds to about $3\text{e-}11\text{ M }^{137}\text{Cs}$ and about $9\text{e-}7\text{ M}$ total Cs. The one-site and two-site model curves were generated using the best-fitting parameters for the column experiments and do not represent fits to the batch data. ....	2-15
Figure 2-7. Results of batch experiment of first desorption step of $^{137}\text{Cs}$ from FFM in SGW. The one-site and two-site model curves were generated using the best-fitting parameters for the column experiments and do not represent fits to the batch data. ....	2-15
Figure 2-8. Results of batch experiment of second desorption step of $^{137}\text{Cs}$ from FFM in SGW (starting with FFM remaining after first desorption step shown in Figure 2-7). Note that the Cs-1 experiment involved desorption in colloid-free SZW, while Cs-2 involved	

desorption in SZW containing 100 mg/L of bentonite colloids. Model curves are not shown because there was no column experiment that corresponded to a second desorption step. The y-axis scale is the same as in Figure 2-7 to allow comparison of the amounts of $^{137}\text{Cs}$ desorbed. ....	2-16
Figure 2-9. Normalized breakthrough curves of $^{137}\text{Cs}$ in column experiments with and without colloids in the injection pulse (top – linear concentration scale; bottom - log concentration scale). Lines are model matches to the data assuming only a single type of sorption site on both the colloids and the FFM. Note that the injection pulses ended when the model curves show sudden drops in concentration. $^3\text{HHO}$ and colloid breakthrough curves are not shown, but the colloids essentially mirrored the $^3\text{HHO}$ curves and showed no evidence of any filtration. Model parameters are listed in Tables 2-5 and 2-6. ....	2-17
Figure 2-10. Normalized breakthrough curves of Figure 2-9 showing model matches to the data assuming two types of sorption sites on both the colloids and the FFM. Model parameters are listed in Tables 2-5 and 2-6. ....	2-19
Figure 2-11. Cs $K_d$ values on colloids as a function of Cs concentration using the sorption parameters of Table 2-6. ....	2-21
Figure 2-12. Normalized breakthrough curves of $^{137}\text{Cs}$ in column experiment in which a portion of the effluent from the experiment with colloids shown in Figures 2-9 and 2-10 was passed through another column. Colloids continued to be injected through the column even after the Cs pulse had ended. Lines are model matches to the data assuming two types of sorption sites on both the colloids and the FFM. Note that the Cs injection pulse ended when the two model curves show sudden drops in concentration. $^3\text{HHO}$ and colloid breakthrough curves are not shown, but the colloids essentially mirrored the $^3\text{HHO}$ curves and showed no evidence of any filtration. Model parameters are listed in Tables 2-5 and 2-6. ....	2-22
Figure 2-13. Fraction of Cs sorbed to colloids a function volume eluted in the experiments of Figure 2-12. ....	2-23
Figure 2-14. Fraction of Cs sorbed to colloids a function of Cs concentration in the experiments of Figure 2-12. Note that 50 CPM/ml is equivalent to about $5\text{e-}8$ M total Cs concentration. ....	2-23
Figure 2-15. Fraction of Cs recovered in each of the column experiments. ....	2-23
Figure 2-16. Predictions of the rising portion of the Cs breakthrough curves of Figures 2-9 and 2-10 using eq. (2-15) as a retardation factor for colloid-facilitated transport in an analytical solution of 1-D advection-dispersion equation. The $K_d$ and $K_c$ values from the batch experiments were used in eq. (2-15). ....	2-25

## TABLES

Table 1-1. DFN parameters used in simulations of the Forsmark repository site, Sweden. ....	1-22
Table 1-2. Values of vertical distance traveled such that linear scaling of the first moment of travel time is observed [All values are in meters]. In the case of resident injection conditions, the mean, standard deviations, and maximum values depend on the lower bound of the power-law, decreasing with increasing lower cutoff. In the case of flux-weighted injection, no statistically significant relationship between these values and the lower cutoff is observed. At all lower cutoff values, the mean values are near zero, indicating the first moment of travel time scales linearly when particles are inserted using flux-weighting .....	1-30
Table 2-1. Synthetic shear zone water constituents. ....	2-4
Table 2-2. Quantitative X-ray diffraction interpretation (wt%) of Grimsel granodiorite, shear zone surface, and bulk FFM materials.....	2-5
Table 2-3. Bulk chemical analysis of granodiorite and FFM materials by X-ray fluorescence analysis (wt%). ....	2-6
Table 2-4. Quantitative X-ray diffraction interpretation (wt%) of FEBEX bentonite. ....	2-7
Table 2-5. FFM sorption parameters yielding the model curves shown in Figures 2-9, 2-10, and 2-12.....	2-20
Table 2-6. Colloid sorption parameters used in all model simulations .....	2-20





# CRYSTALLINE AND CRYSTALLINE INTERNATIONAL ACTIVITIES

## EXECUTIVE SUMMARY

This report presents the results of work conducted between September 2014 and July 2015 at Los Alamos National Laboratory in the crystalline disposal and crystalline international disposal work packages of the Used Fuel Disposition Campaign (UFDC) for DOE-NE's Fuel Cycle Research and Development program. Los Alamos focused on two main activities during this period: Discrete fracture network (DFN) modeling to describe flow and radionuclide transport in complex fracture networks that are typical of crystalline rock environments, and a laboratory investigation of the colloid-facilitated transport of Cs in a saturated crystalline rock environment. Chapter 1 presents the results of the DFN work and is divided into three main sections: (1) A description of the DFNWORKS high-performance computational suite, highlighting and providing examples of efficient computational mesh generation (DFNGEN), flow solving in fracture networks (DFNFLOW), and solving for transport by particle tracking (DFNTRANS), (2) an evaluation of differences in solute transport behavior in large-scale fracture networks depending on whether the source injection is *flux-weighted* or *resident-based*, and (3) an evaluation of the effects of internal fracture aperture variability on solute transport through fracture networks. Chapter 2 presents the results and interpretation of a set of colloid-facilitated  $^{137}\text{Cs}$  transport laboratory experiments using groundwater, colloids and geologic material that are representative of the Grimsel Test Site (Switzerland), an underground research laboratory in a crystalline granodiorite where several colloid-facilitated transport radionuclide transport experiments have been conducted.

In the evaluation of the influence of the mode of source injection on transport through discrete fracture networks, it was observed that the mean value of travel time computed using particles inserted with flux-weighting scaled linearly with distance traveled, and the tails of their cumulative distributions of travel time exhibited power-law scaling. In contrast, the mean travel time of particles inserted using resident injection initially scaled non-linearly with distance, and power-law scaling of the tail of the empirical cumulative distribution of travel times was not observed. However, after accounting for a pre-asymptotic region, the mean travel time of particles inserted using resident injection conditions also scaled linearly, and the tails of their breakthrough curves exhibited power-law scaling with nearly the same exponent as that observed for particles inserted using flux-weighting. The physical mechanism behind this evolution appears to be the draw of mass into larger fractures, and both network scale channeling and in-fracture channeling are observed.

In the evaluation of the effects of internal fracture aperture variability on transport through fracture networks, it was observed that early breakthrough times and retention curves are influenced by in-fracture aperture variability, but the tails of the breakthrough curves are insensitive to these variations. There was no significant effect of aperture spatial correlation length observed. The comparison was done using a flux-weighted source injection, but previous work suggests that similar results would be obtained for a resident-based injection.

In the laboratory investigation of colloid-facilitated  $^{137}\text{Cs}$  transport, it was shown that Cs does not appear likely to transport over long time and distance scales in a crystalline repository environment similar to that at the Grimsel Test Site unless there are very high colloid concentrations. While the partitioning of Cs onto the bentonite colloids used in the experiments was strong, the results suggested that this partitioning was reversible, and the desorption kinetics were fast enough that any colloid-associated Cs would be expected to desorb over time and distance scales relevant to repository performance assessments. It was also shown that the association of Cs with bentonite colloids is expected to be

stronger at lower Cs concentrations, and a relatively simple model to account for this was developed and parameterized using the laboratory data and information from the literature. This model should be capable of explaining observations of much stronger apparent association of Cs with colloids in field experiments at the Grimsel Test Site where much lower Cs concentrations were injected.

Future work will include continued development of the DFNWORKS computational suite, including application of the suite to model/interpret data sets from the BRIE international collaboration being coordinated by the Swedish repository program. This collaboration will provide an excellent opportunity to build and test additional capabilities in DFNWORKS and also to further examine upscaling behavior in discrete fracture networks that could have a significant impact on repository performance assessments. Also, evaluations of the circumstances under which it may be appropriate to use a more computationally-efficient heterogeneous porous medium representation of discrete fracture networks (started in FY 2015) will continue with UFDC colleagues. The colloid-facilitated Cs transport work will be incorporated into a comprehensive evaluation of colloid-facilitated radionuclide transport for repository performance assessments that is planned for the UFDC in FY 2016. This work will also be used to help explain significant differences between observed laboratory- and field-scale (i.e., Grimsel Test Site) colloid-facilitated Cs transport.

# 1. DEVELOPMENT AND DEMONSTRATION OF DISCRETE FRACTURE NETWORK MODEL

## 1.1 Introduction

In this document we report recent technical and scientific developments of the Los Alamos National Laboratory computational suite, dfnWorks, for simulating flow and transport in fractured rocks such as the Crystalline rocks that are the focus of this work package. dfnWorks can be used to stochastically generate three-dimensional discrete fracture networks where fracture geometry is retained and flow and transport are simulated therein without using one-dimensional pipe network approximations. In the first section of this report, we outline the dfnWorks suite, to highlight the novel and important aspects of the suite. The most significant technical advances over the past year have been i) the full-integration with the massively parallel flow solver, PFLOTRAN (Lichtner et al 2015) and ii) the completion of a Lagrangian transport simulator to determine pathlines through the resulting steady state flow field (Makedonska et al. 2015). We also describe the generation and meshing strategy that made these technical advances feasible.

In the subsequent sections, we describe two unique studies that these technical achievements made possible. In the first study a DFN model loosely based on the Forsmark site characterization provided by (SKB, 2011) is adopted to generate an ensemble of DFN in cubic kilometer domains. Then we compared the influence of different initial boundary conditions on the asymptotic behavior of passive transport, Section 1.3. We determined that after a pre-equilibrium region solutes injected under resident conditions evolve and behave similarly to that injected under flux-weighted conditions. The principal results required unique aspects of the dfnWorks suite, namely i) the parallel solver PFLOTRAN allowed for simulating flow through large networks, approximately five thousand fractures with roughly nine millions computational cells, in an efficient manner, ii) the retention of explicit fracture geometry allowed us to link flow and transport behavior to fracture statistics and iii) the particle tracking routine made it easy to account for various boundary conditions. In the second study, we study the influence of in-fracture aperture variability on breakthrough times and retention. dfnWorks retains the explicit fracture geometry, rather than using a one-dimensional pipe-network approximation, and each cell in the computational mesh can be assigned a unique fracture aperture/transmissivity determined using a correlated random field. We compare transport through DFN realizations with a) random aperture variation and b) various correlation lengths in the random aperture field. We find that early breakthrough times and retention curves are influenced by in-fracture aperture variability but the tails of the breakthrough curves are insensitive to these variations.

The studies presented in this report set the stage for two topics that we plan to study extensively going forward. First, we plan to work with the performance assessment team on the Used Fuel Disposition Campaign to determine when the DFN formulation is appropriate for their performance assessment studies. Second, with DOE now a member of the Swedish Task Force we are planning to use DFN tools to contribute to Task 9A, “Force on Modeling of Groundwater Flow and Transport of Solutes”.

## 1.2 DFNWORKS

### 1.2.1 Introduction

Discrete fracture network (DFN) modeling is a promising alternative to continuum approaches for simulating flow and transport through sparsely fractured rocks in the subsurface. In contrast to continuum methodologies, e.g., stochastic continuum (Neuman 2005) and dual/multiple continuum (Lichtner et al. 2015), where effective parameters are used to include the influence of the fractures on the flow, in the DFN approach, geologic field investigations are used to create a network of fractures where the geometry

and properties of individual fractures are explicitly represented as lines in two dimensions or planar polygons in three dimensions. These generated networks are meshed for computation and the governing equations are numerically integrated to simulate flow. Examples of the various DFN methodologies and their applications are found in (Cacas et al. 1990, Berrone et al. 2013, Dreuzy et al, 2004, Dreuzy et al. 2012, Dershowitz, 2014, Erhel et al. 2009, Mustapha et al. 2007, Pichot et al. 2010, 2012, Xu et al. 2006).

The primary challenge in using the DFN methodology is creating an efficient and scalable workflow. The choice to include the detailed geometry of the fractures and the connectivity of the fracture network allows for a more accurate representations of physical phenomenon and robust predictive simulation of flow and transport through fractured rocks compared to continuum approaches. However, these advantages come at an enormous computational cost, especially when attempting to simulate transport through large networks of fractures. This challenge can be broken down into three main obstacles: i) generation of a high quality computational mesh representation of three-dimensional fracture network, ii) solving the governing equations on that mesh in a computationally efficient manner, and iii) simulating transport through the resulting flow field.

In this paper, we describe the DFNWORKS high-performance computational suite that overcomes each of these obstacles in a unique fashion. Developed at Los Alamos National Laboratory over the past five years, DFNWORKS provides a novel workflow to model flow and transport in three-dimensional fractured media at scales ranging from millimeters to kilometers. One DFNWORKS simulation is shown in Fig. 1-1. The fracture network contains approximately nine hundred fractures sampled from three fracture families, with different mean radii, mean orientation, and distribution of fracture lengths. The network is created and meshed using DFNGEN, which combines the feature rejection algorithm for meshing (Hyman et al. 2014) methodology to stochastically generate three-dimensional DFNs on the basis of site specific data with the LAGRIT (LaGriT, 2013) meshing toolbox to create a high resolution computational mesh representation of the DFN. Constant pressure boundary conditions are applied to the left and right faces of the network to drive flow through the network, and steady-state conditions are determined by numerically integrating the governing flow equations using DFNFLOW, which utilizes the massively parallel subsurface flow and reactive transport code PFLOTTRAN (Lichtner et al. 2015). Transport through the DFN is simulated by adopting a Lagrangian approach within DFNTRANS, which is an extension of the of the WALKABOUT particle tracking method (Painter et al. 2012) to determine pathlines through the DFN (Makedonska et al. 2015). Particle trajectories, shown in orange and red, start from a short line source on a single fracture on the inlet plane and disperse from one another as they pass through the network, and exit the domain on numerous fractures. Importantly, all but the network generation can be carried out in parallel, which allows DFNWORKS to be applied to extremely large networks.

In Sec. 1.2.2 we describe each of these pillars of DFNWORKS (DFNGEN, DFNFLOW, DFNTRANS) which make simulations similar to Fig. 1-1 feasible. We conclude with some remarks about the suite and discuss some extensions of the method in Sec. 1.2.3.

## 1.2.2 DFNWORKS Description

An overview of the entire DFNWORKS workflow is illustrated in Figure 1-2. The workflow has three principal pieces (DFNGEN, DFNFLOW, DFNTRANS) which can be broken down into six primary aspects. The input for DFNWORKS is a fractured site characterization that provides distributions of fracture orientations, radius, and spatial locations. DFNGEN: 1) FRAM - Create DFN: Using the fractured site characterization networks are constructed using the feature rejection algorithm for meshing. 2) LAGRIT - Mesh DFN: The LAGRIT meshing tool box is used to create a conforming Delaunay triangulation of the network. DFN-FLOW: 3) Convert Mesh to PFLOTTRAN input: Control volume information is formatted for PFLOTTRAN. 4) Compute Pressure Solution: The steady-state pressure solution in the DFN is obtained using PFLOTTRAN. DFNTRANS: 5) Reconstruct Local Velocity Field: Darcy fluxes obtained using DFNFLOW are used to reconstruct the local velocity field, which is used for particle tracking on the DFN.

6) Lagrangian Transport Simulation: An extension of the WALKABOUT method is used to determine pathlines through the network and simulate transport.

Figure 1-3 illustrates the utility of the DFNWORKS workflow with a simple two fracture network, a rectangular fracture is intersected by an elliptical fracture. Figure 1-3.a overlays the mesh on the two fracture system and the fractures are colored by the distance of the computational cell from the line of intersection. Near the intersection, the mesh is refined to accurately resolve the gradients in the pressure and velocity field, which are much higher near fracture intersections than far away. Away from the intersection the mesh is coarsened to decrease computational requirements. Figure 1-3.b shows the steady-state pressure solution, the gradient is aligned with the x-axis, and yellow lines are pressure contours. The pressure contours on the elliptical fracture show there is a pressure gradient and therefore flow is occurring on this dead-end fracture, it is not connect to the domain boundary or another fracture other than principal fracture. A pipe-network representations that preserves the topology of the DFN while disregarding the detailed geometry of the fractures, a common practice in many DFN simulations, (e.g., Joyce et al. 2014), would eliminate this dead-end fracture from the network, thereby disregarding the influence of flow in the elliptical fracture on transport. Figure 1-3.c shows that the influence of flow in this fracture on transport is non- negligible and how the simplifying assumption missing important transport properties. Here, fractures are colored by x coordinate of gradient of the pressure field, which is the fluid velocity in the x direction, and black lines are particle trajectories passing through the DFN. The non-uniformity of the trajectories results in a distribution of particle travel times that exhibits longitudinal dispersion. Using the simplifying pipe- network approximations, the breakthrough curve would be a step function with no dispersion or tail, which will lead to incorrect upscaled models for transport. Although this is a sample two fracture example, it serves to demonstrate the importance of both the geometry and topology of these networks. The workflow outlined in Fig. 1-2 allows DFNWORKS to retain the explicit geometry and topology so upscaled flow and transport properties do not suffer from these elimination artifacts, and does so in a parallel manner.

In the rest of this section, we describe the different pieces of the DFNWORKS framework in the order that they are implemented during the workflow. We start with the generation method DFNGEN, move on to the flow solver DFNFLOW, and close this section by describing the particle tracking algorithm DFNTRANS which was explained in details in UFD report, FCRD-UFD-2014-000059, of 2014, “Modeling Fluid Flow in Natural Systems: Model Validation and Demonstration”.

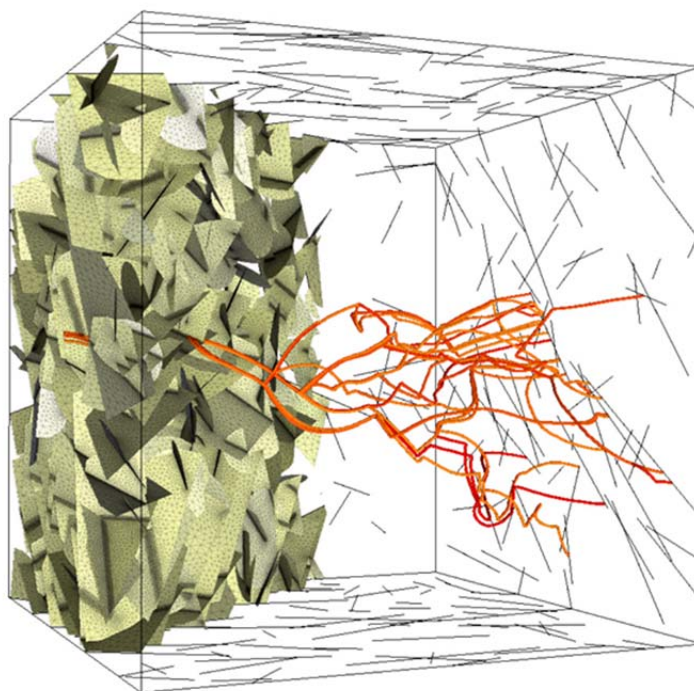


Figure 1-1. Sample fracture network and particle trajectories in a DFNWORKS simulation. The network is created and meshed using DFNGEN, which combines the feature rejection algorithm for meshing (Hyman et al. 2014) to stochastically generate three-dimensional DFNs on the basis of site specific data with the LAGRIT meshing toolbox to create a high resolution computational mesh representation of the DFN that conforms to the lines of intersections between fractures in an intrinsically parallel fashion. Constant pressure boundary conditions are applied to the left and right faces of the network to drive flow through the network, and steady-state conditions are determined by numerically integrating the governing flow equations using DFNFLOW, which utilizes the massively parallel subsurface flow and reactive transport code PFLOTRAN. Transport through the DFN is simulated by adopting a Lagrangian approach within DFNTRANS, which is an extension of the of the WALKABOUT particle tracking method (Painter et al. 2012) to determine pathlines through the DFN. Particle trajectories, shown in orange and red, start from a short line source on a single fracture on the inlet plane and disperse from one another as they pass through the network, and exit the domain on numerous fractures.

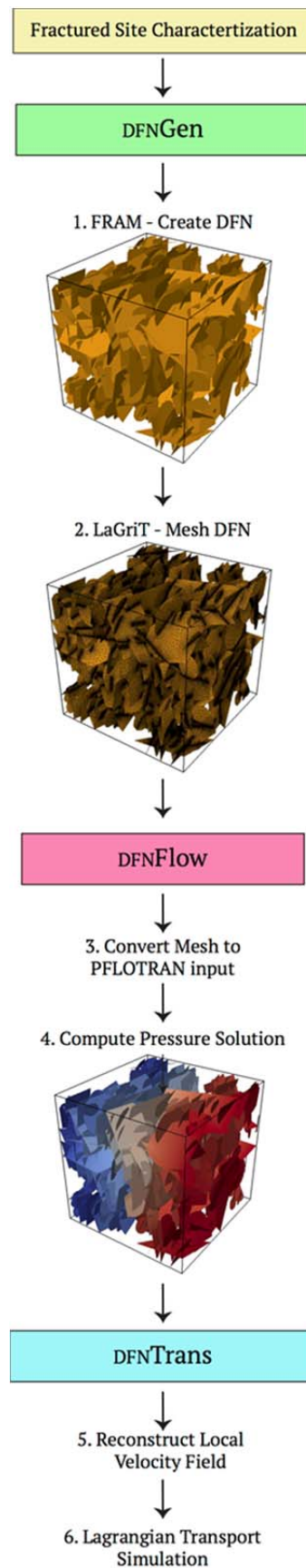


Figure 1-2. DFNWORKS Workflow. From top: The input for DFNWORKS is a fractured site characterization that provides distributions of fracture orientations, radius, and spatial locations. DFNGEN: 1) FRAM - Create DFN: Using the fractured site characterization that networks are constructed using the feature rejection algorithm for meshing. 2) LAGRIT - Mesh DFN: The LAGRIT meshing tool box is used to create a conforming Delaunay triangulation of the network. DFNFLOW: 3) Convert Mesh to PFLOTTRAN input: Control volume information is formatted for pflotran. 4) Compute Pressure Solution: The steady-state pressure solution in the DFN is obtained using pflotran. dfnTrans: 5) Reconstruct Local Velocity Field: Darcy fluxes obtained using dfnFlow are used to reconstruct the local velocity field, which is used for particle tracking on the DFN. 6) Lagrangian Transport Simulation: An extension of the walkabout method is used to determine pathlines through the network and simulate transport.

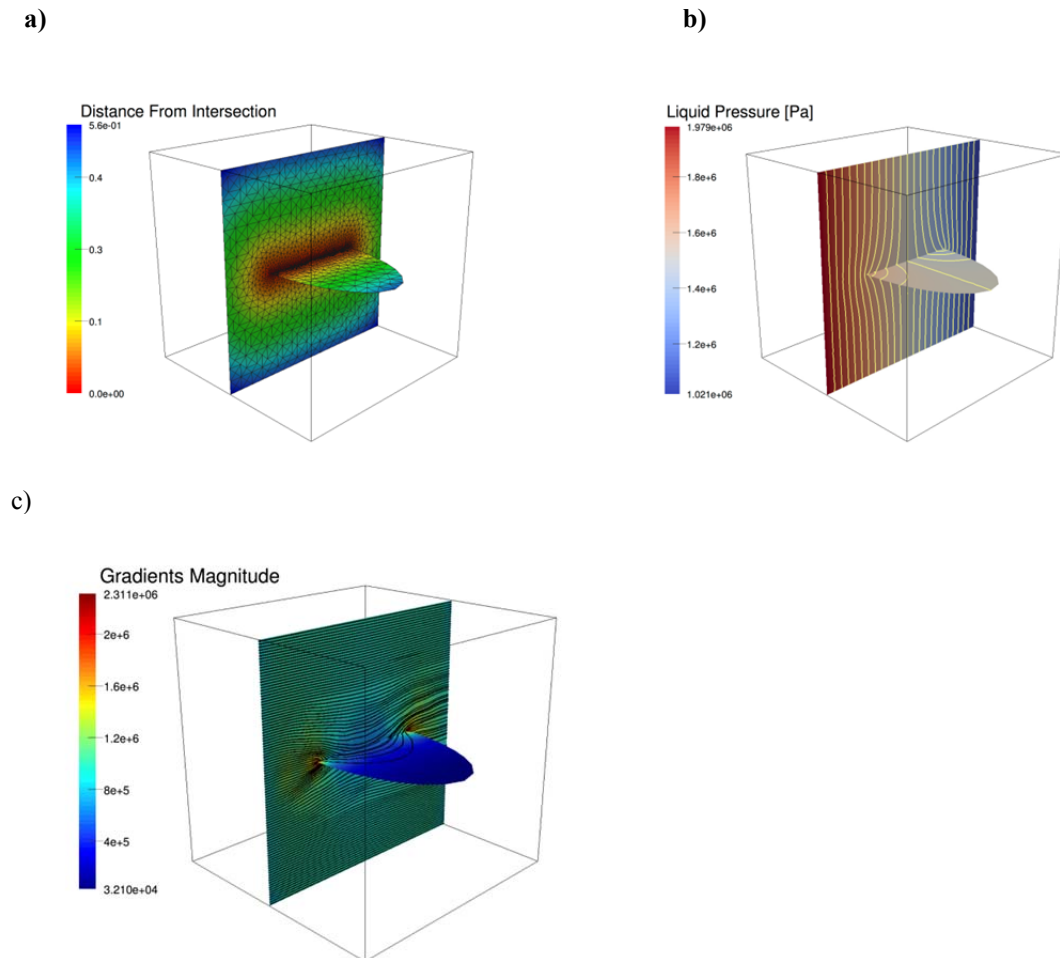


Figure 1-3. Two fracture DFN demonstrating the utility of the DFNWORKS suite. (a) Conforming Delaunay mesh on the two fracture system. The fractures are colored by the distance of the computational cell from the line of intersection. Away from the intersection the mesh is coarsened to preserve computational resources. (b) Steady- state pressure solution, the gradient is aligned with the x-axis, and yellow lines are pressure contours. The pressure contours on the elliptical fracture show there is a pressure gradient and therefore flow is occurring on this dead-end fracture, it is not connect to the domain boundary (or another fracture other than principal fracture. (c) Fractures are colored by x coordinate of



gradient of the pressure field, which is the fluid velocity in the x direction, and black lines are particle trajectories passing through the DFN. The non-uniformity of the trajectories results in a distribution of particle travel times that exhibits longitudinal dispersion. Using the simplifying pipe-network approximations, the breakthrough curve would be a step function with no dispersion or tail, which will lead to incorrect upscaled models for transport.

### 1.2.2.1 DFNGEN: The Feature Rejection Algorithm for Meshing

Each three-dimensional DFN is generated and meshed using the feature rejection algorithm for meshing (FRAM) methodology of Hyman et al., (Hyman et al. 2014). Each DFN is constructed so that all features in the network, e.g., length of intersections between fractures; distance between lines of intersection of a fracture, are larger than a user-defined minimum length scale. This restriction provides a firm lower bound on the required mesh resolution, and special care is taken so that prescribed geological statistics are not affected by this restriction. Once the DFN is generated, the LAGRIT (LaGriT, 2013) meshing toolbox is used to create a high resolution computational mesh representation of the DFN in parallel. An algorithm for conforming Delaunay triangulation is implemented so that meshes along intersections coincide and Voronoi control volumes suitable for finite volume solvers such as FEHM (Zyvoloski, 2007), TOUGH2 (Pruess, 1999), and the fully parallelized PFLOTRAN (Lichtner et al. 2015) are produced. Because the mesh conforms to fracture intersections, the method does not require solving additional systems of linear equations, which is needed if a non-conforming mesh is used (Berrone et al. 2013, Pichot et al. 2010, 2012). Key features of FRAM are that it is fully automated, meaning that throughout the procedure no adjustments of the mesh are performed to improve the mesh quality, and it's flexible, any statistical survey of a fracture site may be used in the generation of fractures, thereby allowing it to generate realistic DFNs that mimic natural fracture sites. In this section, we provide a brief description of FRAM and refer the interested reader to Hyman et al., (Hyman et al. 2014) for a complete description of the method.

#### *Network Generation and Meshing*

The principal issue in meshing a DFN is that to resolve a tiny feature in the network, the edges of the mesh surrounding the feature must be the size of the feature or smaller, if the physics are to be properly resolved. Various methods have been proposed to address this issue, and others, associated with meshing a DFN. In one methodology, pathological cases that degrade mesh quality, e.g., an arbitrarily short line of intersection between two fractures, are systematically removed after an unconstrained fracture network is generated and meshed (Mustapha and Mustapha 2007, Mustapha and Dimitrakopoulos 2011, 2011, Maryska et al. 2005, Erhel et al. 2009). However, such adjustments can deform the network, resulting in fractures that may no longer be planar. Another methodology does not require the mesh to coincide at the line of intersection, and the difficulty is pushed forward by the inclusion of additional linear systems that must be solved to impose continuity of pressure and flux along fracture intersections (Benedetto et al. 2014, Berrone et al. 2013, Pichot et al. 2010, 2012). These additional linear systems make this methodology computationally more expensive when solving for flow than when the meshes are forced to align. In addition, a non-aligned grid at fracture intersections may complicate solute transport calculations.

In contrast to these methods, DFNGEN uses FRAM to constrain the generation of the network so that it only contains features greater than or equal to a user-prescribed minimum length scale  $h$ . Each fracture in our DFN is a planar straight-line graph (PSLG) made up of the set of line segments that represent the boundary of the fracture and the line segments that represent where other fractures intersect it. Given a set of PSLGs  $\mathcal{X}$  with arbitrary orientation in  $\mathbb{R}^3$ , one can define a *local feature size at a point  $p$*  as the radius of the smallest sphere centered at  $p$  that intersects two non-incident vertices of segments of  $\mathcal{X}$  (Ruppert 1995). In a three-dimensional DFN, examples of a measurable feature include: the length of the line of

intersection between two fractures, the distance from the end of a fracture intersection that is interior to the polygon boundary to the polygon boundary, and the distance between two fracture intersection line segments. During the generation process, we require that the DFN never generate a fracture with a feature of size less than  $h$ , which provides a firm lower bound on the required resolution of the mesh. When the resulting network is meshed, all features can be resolved by generating triangular cell edges with a minimum length slightly less than  $h$ .

By constraining the network so that all features in the network are greater than  $h$ , FRAM ensures that pathological cases which degrade mesh quality are not present in the network. Under these conditions, a conforming Delaunay triangulation algorithm (Mount and Gable, 2001) can be used to ensure that the line of intersection between any two fractures is preserved in the mesh so long as the lines of intersection are discretized in steps less than  $h$ . The conforming Delaunay triangulation algorithm procedure results in meshes that are coincident along the common line of intersection between fractures. Because computational control volumes (Voronoi polygons) are based on vertices and the triangular meshes are coincident along intersections, the Voronoi cells also conform at the fracture boundaries. This results in Voronoi control volumes that span both of the intersecting fractures. However, the neighbors of these Voronoi cells are still two-dimensional. The need to check for a feature size less than  $h$  means that the fracture generation process is computationally more demanding than methods that do not impose the minimum feature size constraint. The tradeoff is a streamlined/parallelized process of mesh generation, numerical integration of the pressure solution, and simplifying particle tracking through the resulting flow field.

### *Mesh Examples*

In figure 1-4 three intersecting fractures show the intersecting conforming Delaunay triangulations. Two of the fractures are colored by distance from lines of intersections (traces) with each other and other fractures that intersect these fractures, and the other is semi-transparent for clarity. The mesh is optionally coarsened away from intersections with pressure gradients will be lower. The inclusion of the semi-transparent fracture illustrates how FRAM creates a mesh that adheres to multiple intersections on the surface of a single fracture. Two additional fractures intersect the elliptical fracture, and intersect one another on the surface of that fracture, as shown by the intersecting white colored regions. The inset shows that the Delaunay mesh conforms all of these lines of intersection.

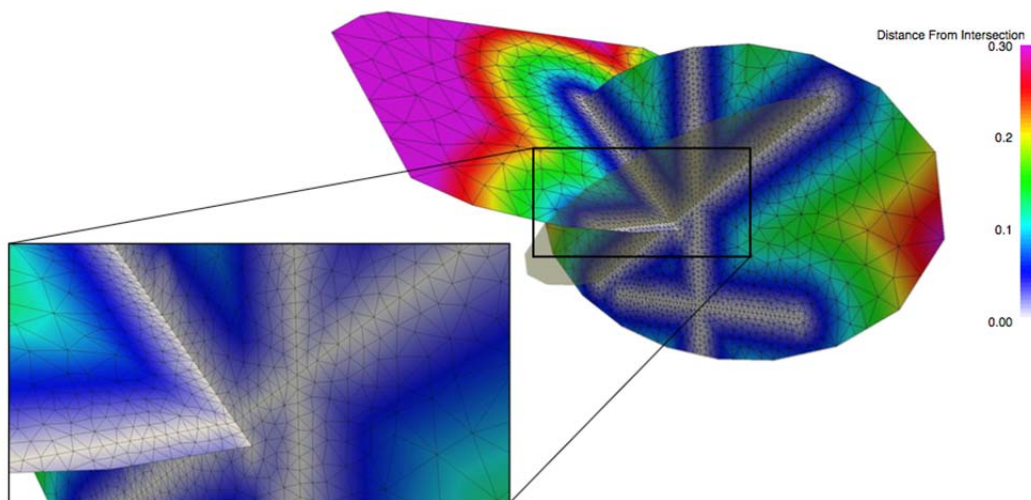


Figure 1-4. Three intersecting fractures show the intersecting conforming Delaunay triangulations. Two of the fractures are colored by distance from lines of intersections (traces) between fractures, and the

other is semi-transparent. The mesh is optionally coarsened away from intersections with pressure gradients will be lower. The inclusion of the semi-transparent fracture illustrates how FRAM creates a mesh that adheres to multiple intersections on the surface of a single fracture. Two additional fractures intersect the elliptical fracture, and intersect one another on the surface of that fracture, as shown by the intersecting white colored regions. The inset shows that the Delaunay mesh conforms all of these lines of intersection.

```

CELLS      N
  id1 x1 y1 z1 volume1
  id2 x2 y2 z2 volume2
  ...
  ...
  idN xN yN zN volumeN

CONNECTIONS  M
  idup,1 iddn,1 x1 y1 z1 area1
  idup,2 iddn,2 x2 y2 z2 area2
  ...
  ...
  idup,M iddn,M xM yM zM areaM

```

Figure 1-5. Explicit grid format in PFLOTTRAN that is used to read the DFN mesh.  $N$  is the number grid cells and  $M$  is the total number of internal connections between grid cells. In the first block under CELLS,  $id_i$ ,  $x_i$ ,  $y_i$ ,  $z_i$  are the cell id,  $x$ -coordinate,  $y$ -coordinate and  $z$ -coordinate of the  $i$ -th grid cell, respectively. In the second block under CONNECTIONS,  $id_{up,j}$ ,  $id_{dn,j}$ ,  $x_j$ ,  $y_j$ ,  $z_j$ ,  $area_j$  are the upwind grid cell id of the  $j$ -th connection, downwind grid cell id of the  $j$ -th connection, Coordinates of the face between the  $j$ -th connection and the area of the face between the  $j$ -th connection, respectively.

#### *Remarks about FRAM*

Decisions about the minimum length scale  $h$  that will be represented in a DFN are made a priori; which is typically the case in scientific computing and not unique to FRAM. When adopting the FRAM methodology the choice of the  $h$  will be reflected in the generated network. If  $h$  is chosen to large with respect to fracture and domain size, then it will be difficult to generate a DFN that meets the density requirements. If  $h$  is chosen too small, then computational cost associated with meshing and solving the governing equations will increase. The choice of  $h$  should be made so that all physical phenomena of interest are greater than  $h$ , so they can be well resolved by the computational mesh, while limiting computational expenses. The tradeoff between spatial resolution and computational expediency inherent in the choice of  $h$  in FRAM is the familiar tradeoff in most branches of scientific computing.

Due to the rejection nature of FRAM some of the desired distributions in the network, e.g. fracture length, will not be properly represented due to over rejection unless certain criteria are met. For example, larger fractures generate more measurable features in the network than smaller ones and can be rejected a disproportionate amount. However, modifying the procedure by which fracture lengths are sampled can alleviate the issue of bias in the represented fracture length distribution. This is only necessary when sampling from a distribution with a broad range of lengths, such as a truncated power law distribution. An alternative solution is decreasing  $h$  to loosen the acceptance criteria. In the limit of  $h \rightarrow 0$ , all prescribed distributions will be recovered exactly because no fractures are rejected. Details about these procedures are in (Hyman et al. 2014).

### 1.2.2.2 DFNFLOW: Flow Solver

Once the DFN is generated and meshed using DFNGEN, Voronoi control volumes, the dual mesh of the Delaunay triangulation, are computed. Then a Python script processes the LAGRIT output into an unstructured grid format compatible with the massively parallel subsurface flow code PFLOTRAN. Modifications were made to PFLOTRAN to read the unstructured Voronoi mesh and to perform calculations on the Voronoi mesh. The format to read Voronoi meshes involves locations of the Voronoi cell-centers, the connectivity of the cell-centers and the cell areas, and is referred to as explicit unstructured grid format (see Fig. 1-5). This explicit unstructured grid format can be used to read any generalized  $n$ -faced polygonal meshes. The permeability in each Voronoi cell is based on the local aperture of the fracture. These values are computed using a Python script and read into PFLOTRAN. Using this information, PFLOTRAN determines the steady-state pressure field within the DFN using a two-point flux based finite volume scheme. By using a control volume based discretization for flow, local mass balance is ensured, and by using a Voronoi mesh, the accuracy of the flux evaluation is maintained (Zyvoloski and Vesselinov, 2006). PFLOTRAN returns the groundwater fluxes (Darcy velocities) at the edges of the Voronoi control volumes. These fluxes are then used in DFNTRANS for velocity reconstruction and particle tracking. In the next part of this section, a brief description of PFLOTRAN is presented. The reader is referred to (Mills et al. 2007, Hammond et al. 2012, 2014) for details of PFLOTRAN implementation and its parallel performance.

PFLOTRAN (Lichtner et al. 20150) is an open-source, massively parallel, multiscale and multiphysics code for subsurface and surface processes. The code is the result of a multiple DOE national laboratory effort with core developers from LANL, SNL, LBNL and ORNL, with users and contributors from universities and other research facilities all over the world. PFLOTRAN is built on top of PETSc (Portable, Extensible Toolkit for Scientific Computation) (Balay et al. 2014) framework and incorporates PETSc's parallel data structures, linear and non-linear solvers, and relies on domain decomposition for parallelism, and was originally developed as part of the Department of Energy SciDAC-2 groundwater program. This foundation has allowed PFLOTRAN to run simulations with billions of degrees of freedom on over 100,000 processor cores. The code solves a system of nonlinear partial differential equations that model non-isothermal multiphase flow, reactive transport and geomechanics in porous media. Equations describing multiple continua (for matrix-fracture interactions) and non-isothermal surface flow are also solved. The code is written in object-oriented Fortran 2003 (base and derived classes) which gives the flexibility to: a) add new process models and couple with existing process models, and b) couple with other external codes that use PETSc and drive the coupling with PFLOTRAN as the master. To reduce I/O bottlenecks, PFLOTRAN also has parallel I/O modules built and outputs data in Tecplot ASCII as well as the binary HDF5 formats. The HDF5 output can be visualized using the HPC toolkits such as VisIt and Paraview. PFLOTRAN can run on a wide range of architectures ranging from multi-core laptops and clusters to petascale leadership-class supercomputers. PFLOTRAN applications are related to areas in energy, climate and nuclear including nuclear waste disposal (Makedonska et al. 2015), CO<sub>2</sub> sequestration (Lichtner and Karra, 2014, Lu and Lichtner, 2007), enhanced geothermal systems (Lichtner and Karra, 2014), groundwater contamination (Hammond and Lichtner, 2010), hydraulic fracturing (Karra et al. 2015, Middleton et al.2015), induced seismicity (Karra et al. 2013) and Arctic hydrology and

climate (Karra et al. 2014, Mills et al. 2012). PFLOTTRAN can be downloaded from <http://bitbucket.org/pfлотran>.

The subsurface flow processes currently available in PFLOTTRAN include single-phase variably-saturated flow (Richards equation), non-isothermal two-phase water-supercritical CO<sub>2</sub>, general mode that allows modeling multiphase flow of any two component systems, thermal-hydrologic coupled heat and mass conservation and three-phase ice-liquid-vapor (water) flow for Arctic applications. Any of these flow modes can be coupled to multicomponent reactive transport equations using either a global implicit algorithm or operator splitting. The multicomponent reactive transport processes include aqueous complexation, sorption, mineral precipitation/dissolution, and microbially-mediated biodegradation. Because these flow processes are already available in PFLOTTRAN, they can all be used DFN simulations with little extended effort on behalf of the user. Additionally, PFLOTTRAN can be controlled from Python using the PyFLOTTRAN (karra and Kitay, 2015) interface that provides Python classes and methods for easy modification of PFLOTTRAN input file. This allows for a streamlined workflow from pre-processing to post-processing in Python, and usage of Python scripting tools and packages for directory hierarchy, multiple processing and error checking.

### 1.2.2.3 DNFTRANS: Particle Tracking

Particle tracking method is a method for resolving solute transport using control volume flow solutions obtained from flow solver (dfnFlow) on the unstructured mesh generated using dfnGen. We adopt a Lagrangian approach and represent a non-reactive conservative solute as a collection of indivisible passive tracer particles. Particle tracking methods: a) provide a wealth of information about the local flow field, b) do not suffer from numerical dispersion, which is inherent in the discretization of advection-dispersion equations, and c) allow for the computation of each particle trajectory to be performed in an intrinsically parallel fashion if particles are not allowed to interact with one another or the fracture network. However, particle tracking on a DFN poses unique challenges that arise from both the quality of the flow solution, the unstructured mesh representation of the DFN, and the physical phenomena of interest. The flow solutions obtained from dfnFlow are locally mass conserving, so the particle tracking method does not suffer from the problems inherent in using Galerkin finite element codes, (e.g., Dershowitz, 2014, Mustapha et al. 2011, Elsworth 1986, Geier 2011, Hartley et al. 2004, Outters and Shuttle, 2000), where experience has shown that particles can become stuck in cells that exhibit unphysical stagnant regions because the flow solution does not conserve mass locally. Because the primary interest of particle tracking is simulation of mass transport, these stuck particles, representing a loss of mass in the system due to numerical artifacts, limit the usefulness of flow field provided by finite element methods (Geier 2011). The coupling of dfnTrans with finite volume codes ensures that all particles released into these DFN will eventually exit the system, and do so without incorporating additional pipe-network simplifications (Cacas et al. 1990, Dershowitz and Fidelibus, 1999).

In this section, we highlight the most important details of the method, namely: (i) the reconstruction of velocities on each vertex of the computational mesh and (ii) the unique approach taken to address mass transport through fractures intersections. A comprehensive explanation of dfnTrans and details concerning its implementation can be found in Makedonska et al., (Makedonska et al. 2015).

#### 1.2.2.3.1 Reconstruction of Velocity Field

The pathline followed by a particle is obtained by numerically integrating the trajectory equation,  $\mathbf{x} = \mathbf{v}(\mathbf{x}(t))$ , with initial position  $\mathbf{x}(0) = \mathbf{x}$ . Here,  $\mathbf{v}$  is the Eulerian velocity vector that must be defined at every point in the fracture network. However, the control volume flow solution provides a set of scalar quantities that are approximations to the normal component of Darcy flux integrated over each edge of each control volume cell, rather than the required continuous velocity field.

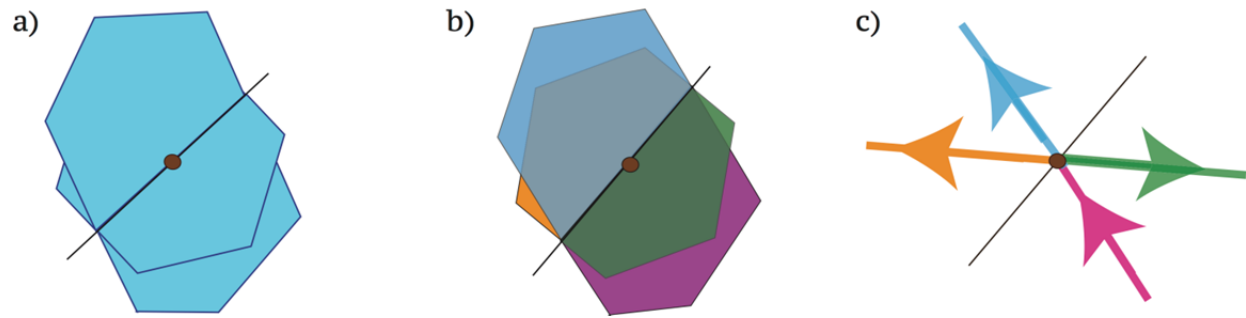


Figure 1-6. Illustration of the technique used to reconstruct flow velocities along the line of intersection between two fractures. a) A control volume along a line of intersection between two fractures. Fluxes are defined on faces of the control volume cells. b) The control volume is split into four sub-polygons using the line of intersection. The green and orange sub-polygons are on one fracture and the blue and purple are on another. c) The flow velocities are reconstructed on each of the split polygons, here arrows indicate inflow/outflow. In this example, the flux into the control volume occurs through the purple sub-volume and outflow occurs through the remaining sub-polygons.

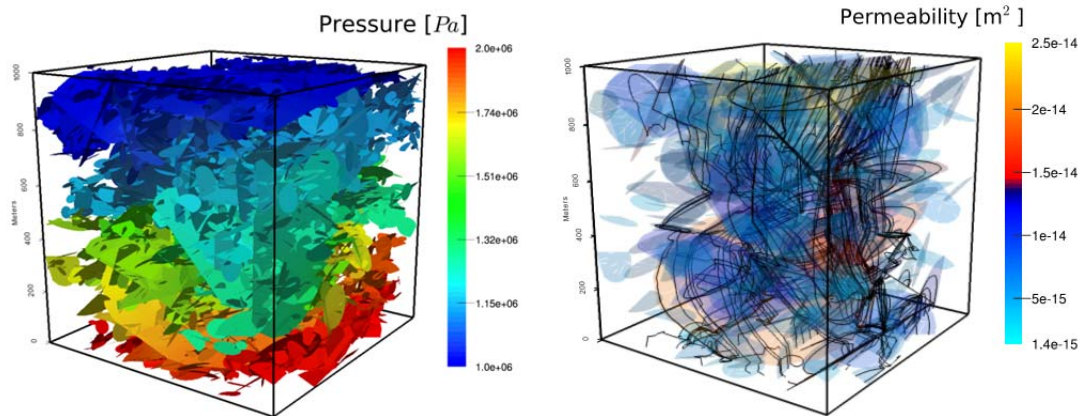
To address this issue Painter et al. (Painter et al. 2012) developed an approach to reconstruct velocity fields from flow solutions obtained on unstructured control volume mesh. Using the flow solution provided by dfnFlow, cell-centered velocities are estimated by solving a overdetermined linear system for the Darcy velocity. The system is overdetermined because each control volume has more sides than the dimension of the problem, e.g., in two dimensions each control volume has a minimum of three sides. On cells in the interior of the domain an unconstrained least squares method is used, and a constrained least squares method used to reconstruct velocities on boundary cells to enforce Neumann boundary conditions along fracture walls.

This procedure creates piecewise constant flow velocity vectors at every vertex in the DFN mesh. Then barycentric interpolation (Coxeter, 1969) is used to determined a particle's velocity at any location within a cell at any point in the DFN. Using these velocities, an adaptive time stepping first-order predictor-corrector method is used to numerically integrate the trajectory equation. The semi-implicit nature of the predictor-corrector method prevents particles from reaching the edge of a fracture with no-flow boundary conditions.

### 1.2.2.3.2 Fracture Intersections

Simulating transport through fracture intersections is a principal challenge for modeling transport through a three-dimensional DFN. The control volume cells along fracture intersections are three-dimensional objects formed from the union of two polygons in different planes; control volume cells away from intersections are two-dimensional planar polygons. This peculiar shape at intersections results in more complicated flow behavior than elsewhere in the network. Flow can go through the intersection and continue onto the same fracture without changing direction, or it change direction and exit onto the intersecting fracture or, as is usually the case, the flow can split by some percentage between the fractures. The technique schematically presented in Fig. 1-6 was developed to provide the necessary information so that the number of particles dispersed at fractures intersections is representative of the percentage of flux outgoing onto each fracture at intersections. Figure 1-6.a shows a control volume along a line of intersection between two fractures. The control volume is a three-dimensional objects formed from the union of two polygons in different planes where the Darcy flux is defined along the boundaries of the control volumes. The first step is dividing the control volume into four sub-polygons using the line of intersection, this partition is shown in Fig. 1-6.b. Here, the green and orange sub-polygons are on one

fracture and the blue and purple are on another. Then the flow velocities are reconstructed on each of the split polygons, where arrows indicate inflow/outflow. In the example shown in Fig. 1-6.c, the flux into the control volume occurs through the purple sub-volume and outflow occurs through the remaining sub-polygons; any combination of inflow/outflow can be accommodated. To determine how particles pass through intersections, probabilities proportional to the outgoing flux are assigned to each cell that borders the intersection. Then, the downstream cell is chosen randomly based on these probabilities. This method ensures that the percentage of particles exiting onto each cell is proportional to the flux exiting onto those cells.



a) Pressure Solution

b) Particles Trajectories

Figure 1-7. a) A DFN realization based upon the fractured granite at the Forsmark, Sweden site in a  $1 \text{ km}^3$  domain. The model consists of multiple sets of circular fractures whose orientations follow a Fisher distribution. The fracture diameters in each fracture set follow a truncated power-law distribution with lower cutoff at 15 meters. Fractures are colored by pressure. Dirichlet boundary conditions are imposed on the top (1 MPa) and bottom (2 MPa) of the domain to create a pressure gradient in the z direction, and no-flow boundary conditions are imposed along lateral boundaries. b) Two hundred particle trajectories within the DFN shown in Fig. 1-7. Particles are inserted uniformly along fractures on the bottom of the domain. Trajectories are overlaid on the networks shown in Fig. 1-7(a), but here fractures are colored by the permeability, to show how particles are drawn to larger fractures, which have higher permeabilities and offer less resistance than smaller fractures. Although particles are inserted uniformly along fractures in the inlet plane, they cluster on larger fractures as they exit the domain. This clustering suggests that transport only occurs within a small portion of the fracture network far away from the inlet plane.

### 1.2.2.3.3 Analysis of Trajectories

The information obtained using these particles is processed in a number of ways to characterize transport through these networks. Foremost, distributions of travel time and pathline length are constructed and their moments computed. In addition to these more common measurements, information about the location and velocity of the particles can be recorded throughout their journeys. This information can be sampled using two different methods, at a set of given times or at a set of given locations. The sampling at prescribed time increments can be used to determine key statistical features of the plume such as mean displacement and dispersion. Complementary sampling information at a set of given location, e.g., at uniformly spaced control planes, creates a pseudo-time evolution of the plume with distance traveled. Regardless of which sampling method is used, information such as current fracture aperture, box-dimension of the plume, and number of fractures a particle has touched can be recorded and analyzed.

Flow topology maps where the particle trajectories are used to determine what percentage of the network contributes to transport can be also obtained using these particle trajectories.

The Swedish Nuclear Fuel and Waste Management Company (SKB) has undertaken a detailed investigation of the fractured granite at the Forsmark, Sweden site as a potential host formation for a subsurface repository for spent nuclear fuel (Hartley and Joyce, 2013, SKB, 2011). The Forsmark area is about 120 km north of Stockholm in northern Uppland, and the repository is proposed to be constructed in crystalline bedrock at a depth of approximately 500 m. Based on the SKB site investigation, a statistical fracture model with multiple fracture sets was developed; detailed parameters of the Forsmark site model are in (Hartley and Joyce, 2013). We adopt a subset of the model that consist of three sets of background (non-deterministic) circular fractures whose orientations follow a Fisher distribution, fracture radii are sampled from a truncated power-law distribution, the transmissivity of the fractures is estimated using a power-law model based on the fracture radius, and the fracture aperture is related to the fracture size using the cubic law (Adler et al. 2012). Under such a formulation, the fracture apertures are uniform on each fracture, but vary among fractures. The network is generated in a cubic domain with sides of length one-kilometer. Dirichlet boundary conditions are imposed on the top (1 MPa) and bottom (2 MPa) of the domain to create a pressure gradient aligned with the vertical axis, and no-flow boundary conditions are enforced along lateral boundaries.

A sample realization of the Forsmark DFN is shown in Fig. 1-7. The realization contains 4,934 fractures and the computational mesh consists of 7,731,299 cells. There are significantly more small, low permeability, fractures than larger fractures due to the power law distribution used to generate the network. The larger fractures act as conduits for flow, connecting numerous small fractures together in the network. Figure 1-7.a shows the steady state pressure solution. Fractures are colored by pressure, with warmer colors indicating higher values. A selection of two hundred particle trajectories passing through this network are shown in Fig. 1-7.b. The particles are inserted uniformly along fractures in the inlet plane (bottom), and the movement of the particles is determined by the local velocity. The permeability of the fractures is shown along with the trajectories to highlight that particles are attracted toward larger fractures. Because the fracture permeability is based upon the fracture radius, the largest fractures have the highest permeabilities. Although the particles are inserted uniformly, their trajectories cluster together onto larger fractures. This clustering suggests that transport only occurs within a small portion of the fracture network far away from the inlet plane.

#### **1.2.2.3.4 Solute Transport with Sorption and Matrix Interactions**

The particle trajectories generated by dfnWorks represent those of hypothetical groundwater tracers moving through complex DFNs. Although not strictly part of dfnWorks, the dfnWorks-generated trajectories may be used as transport pathway input to contaminant transport algorithms that use particle tracking in the time domain (Painter et al. 2008) to simulate transport of trace contaminants such as radionuclides. For example, groundwater tracer trajectories generated by dfnWorks may be used as input to the MARFA computer code (Painter and Mancillas, 2013) to simulate the migration of trace contaminants in DFNs taking into account diffusion into a matrix of limited or unlimited extent, sorption onto immobile minerals, longitudinal dispersion, and first-order transformations (decay and in-growth).

### **1.2.3 Remarks**

DFNWORKS is a parallalized computational suite for simulating single/multiphase flow and transport in stochastically generated three-dimensional discrete fracture networks. We have described the pillars of DFNWORKS (DFNGEN, DFNFLOW, DFNTRANS) and provided several applications of the work flow to demonstrate its utility. The three applications we presented highlight various aspects of DFNWORKS including its ability to generate networks in accordance with geological data, match transport properties to data, and simulate multiphase flow.



We focused on the basic elements of the computational suite to provide a foundational understanding of the workflow. However, there are several extensions of the method that, while not being central to the workflow, increase its utility. These include: (i) in-fracture aperture/transmissivity variability; (ii) networks composed of multiple regions with variable fracture densities; (iii) mapping a DFN into a continuum for the inclusion of fracture-matrix interaction; (iv) multicomponent reactive transport; (v) integration uncertainty quantification and sensitive analysis suites such as MADS (Model Analysis and Decision Support) (Vesselinov and Harp, 2012); (vi) inclusion of large deterministic fractures for site specific studies.

## 1.3 Influence of Injection Mode

### 1.3.1 Introduction

In low permeability fractured rocks, networks of fractures are typically the principal pathways for fluid flow and transport of dissolved contaminants. However, fractured rocks are difficult to characterize because their structural attributes, e.g., fracture orientations and apertures, exhibit anisotropy and heterogeneity on length scales that span several orders of magnitude (Neuman, 2005). The energy and engineering applications impacted by this uncertainty include hydrocarbon extraction, aquifer storage and management, geothermal energy extraction, environmental restoration of contaminated fractured rock, and the disposal of used nuclear fuel (Adler et al. 2012, Berkowitz, 2002, Faybishenko, 2005, Karra et al. 2015). In particular, the long term storage of used nuclear fuel in subsurface repositories requires a comprehensive understanding of the mechanisms governing transport in fractured media.

There exists a variety of models, both computational and theoretical, for the phenomena associated with transport in heterogeneous and fractured media (Berkowitz and Scher, 1997, Berkowitz, 2002, Cacas et al. 1990, Cvetkovic, 2011, Endo et al. 1984, Frampton and Cvetkovic, 2007, 2011, Long and Remer, 1982, Neuman and Tartakovsky, 2009, O'Malley and Vesselinov, 2014, Painter and Cvetkovic, 2005, Painter et al. 2002, Smith and Schwartz, 1984, Schwartz and Smith, 1988, Tsang et al. 1988). However, a major obstacle in the successful application of these models in fractured media is the lack of field scale information that can be used to verify and validate them. This information gap is the result of physical limitations associated with *in situ* tracer experiments (Andersson et al. 2007). Computational simulations, such as those performed here, serve as a virtual laboratory to provide data which can be used to calibrate and validate analytical models, while also providing insights into transport through fractured media. The most common computational approaches to simulate flow and transport in fractured media are the stochastic continuum, dual/multiple continuum, and discrete fracture network (DFN) methodologies, each of which has its advantages and disadvantages (Neuman 2005, Lichtner and Karra 2014, Painter et al. 2002).

In general, the initial distribution of mass transport in fractured rock can be modeled using one of two injection methods. The first method, *flux-weighted injection*, mimics a solute that is released in proportion to the flux at the location of insertion, e.g., miscible gas released into a packed off borehole connected to hydraulically active fractures (Jankovic and Fiori, 2010). The second method, *resident based injection*, is designed to mimic a source that introduces a solute uniformly throughout the input zone, e.g., multiple leaking canisters within a buffer zone (Frampton and Cvetkovic, 2009). Studies concerning the influence of injection mode on solute transport date back to at least (Kreft and Zuber, 1978). They derived solutions to the advection-dispersion equation for various initial and boundary conditions in semi-infinite and infinite domains. Computational studies of transport through strongly heterogeneous and fractured media, e.g., two and three-dimensional porous media (Demmy et al. 1999, Gotovac et al. 2009, 2010, Jankovic and Fiori, 2010, Vanderborcht 1998) and in two-dimensional DFN simulations (Frampton and Cvetkovic, 2009), report that the choice of injection scheme influences key physical observables, namely the scaling of the moments of transport travel time with distance traveled.

Many theoretical models of transport require these moments to scale linearly with distance; most notably Fickian dispersion (Frampton and Cvetkovic, 2011). These previous studies found that solutes inserted under flux-weighted conditions scales linearly with distance, while those obtained using resident injections display nonlinear behavior. In a computational study of transport through strongly heterogeneous two-dimensional porous media, (Gotovac et al. 2010) found that all moments of travel time eventually scale linearly with distance, even those observed using resident based injection that initially displayed nonlinear behavior. In the context of DFN, (Frampton and Cvetkovic, 2009) observed non-linear scaling of travel time modes under resident conditions using in two-dimensional DFNs, and (Frampton and Cvetkovic, 2011) observed linear scaling of the first two moments of travel time obtained using flux-weighted injection in three-dimensional DFN, but they did not consider resident injection.

The contribution of this paper is testing the hypothesis that solute plumes injected under resident conditions evolve to behave similarly to solutes injected under flux-weighted conditions in terms of transport time, pathline tortuosity, and flow channeling. We test this hypothesis in large (km) three-dimensional DFN. Computational limitations have prohibited simulations sufficiently large enough to investigate this hypothesis previously. A new DFN methodology allows us to couple the DFN methodology with a Lagrangian approach to model transport through fractured media at the kilometer-scale and characterize the influence of injection mode, asymptotic behavior of the plumes, and the physical mechanisms at play. Statistically independent DFN realizations are generated in kilometer cubes based on site characterization data obtained from the Forsmark site in Sweden (SKB, 2011), a potential host repository for spent nuclear fuel. We selected this particular location due to the wealth of information available about the site that resulted from the Swedish Nuclear Fuel and Waste Management Company's (SKB) detailed investigation of the area. Even though the DFN are based on site-specific data, the presented results are general, not than site-specific. We use generic boundary conditions, do not include *site-specific features*, e.g., fracture zones, rock domains, topography, regional flow, and only use a subset of the site investigation data related to fracture statistics from the cited report. Although these large scale simulations are feasible using modern DFN capabilities, specifically the computational suite DFNWORKS that we utilize, they are still computationally demanding. Therefore, we limit the number of DFN samples to sixty. However, the domains sizes considered appear to be sufficiently large to provide informative statistics about the ensemble.

Each of the DFNs contains approximately five thousand fractures. A pressure gradient is imposed across the domain, the governing equations for flow are numerically integrated until steady state conditions are reached, and advective non-reactive particles are injected into the resulting flow field to simulate solute transport through the networks. Approximately one hundred thousand advective particles are inserted into each DFN. In sum, over 5.5 million particle trajectories are considered. Our focus is on advection-dominated flows where the effects of matrix diffusion are small. We impose no-flow boundary conditions along fracture walls so that particles do not interact with the fracture walls or the surrounding, and do not consider processes such as absorption or precipitation. Spatial and temporal particle attributes are recorded at uniformly spaced control planes throughout the domain to observe the evolution of transport properties as functions of distance traveled. Both flux-weighted and resident injection methods are considered.

We observe that the mean value of travel time computed using advective particles inserted using flux-weighting scale linearly with distance traveled, and the tails of their cumulative distributions of travel time exhibit power-law scaling. In contrast, the mean travel time of particles inserted using resident injection initially scales non-linearly with distance and power-law scaling of the tail of the empirical cumulative distribution of travel times is not observed. However, after accounting for a pre-asymptotic region, the mean travel time of particles inserted using resident injection conditions also scales linearly, and the tails of their breakthrough curves exhibit power-law scaling with nearly the same exponent as that observed for particles inserted using flux-weighting. The physical mechanism behind this evolution

appears to be the draw of mass into larger fractures, both network scale channeling and in-fracture channeling are observed.

We present a formal mathematical description of the problem in Sec. 1.3.2. Next, our adopted methodology for generating DFNs and therein simulating flow and transport is outlined in Sec. 1.3.3. We use the computational suite DFNWORKS, which combines the feature rejection algorithm for meshing (FRAM) (Hyman et al. 2014), the LaGriT meshing toolbox (LaGriT, 2014) the massively parallel flow and transport solver PFLOTTRAN (Lichtner et al. 2015), and an extension of the WALKABOUT particle tracking method (Painter et al. 2012) to determine pathlines through the DFN and simulate conservative solute transport (Makedonska et al. 2015). In Sec. 1.3.4, we present and discuss the spatial and temporal Lagrangian observations. Final remarks are provided thereafter in Sec. 1.3.5.

### 1.3.2 Theory

The focus of this work is on the spreading of a nonreactive conservative solute in a three-dimensional discrete fracture network (DFN) represented by a cloud of passive tracer particles, i.e., using a Lagrangian approach. The imposed pressure gradient is aligned with the vertical axis,  $z$ , and thus the primary direction of flow is also in the vertical direction. Particles are released at an inlet plane of the domain,  $z = 0$ , at time  $t = 0$ .

#### 1.3.2.1 Problem Statement

Let  $\mathcal{X}$  denote a set of  $N$  particles with unique initial positions,  $x_i = (x_i, y_i, 0)$  for  $i = 1, \dots$ , on the fractures which intersect the inlet plane. The trajectory of the  $i$ th particle starting at  $x_i$  is defined by the pathline,  $p_i$ , which is the solution to initial value problem

$$\frac{dx}{dt} = v(x(t)), \quad x(0) = x_i \quad (1-1)$$

Here,  $v$  is the Eulerian velocity vector with components,  $v = [u, v, w]$  defined at every point in the fracture network. The length of the pathline,  $\ell$ , is used to parameterize the spatial and temporal coordinates of the particle. Explicitly,  $p(\ell) = [x(\ell), y(\ell), z(\ell), t(\ell)]$  for  $\ell > 0$  and  $p_i(0) = [x_i, y_i, 0, 0]$ . Under the assumptions of steady state flow and in the absence of local dispersion, particles move along their respective pathlines and arrive at a control plane,  $CP(z)$ , at the point  $p_i(\ell') = [x(\ell'), y(\ell'), z, t(\ell')]$ , at a time  $t(\ell') = \tau_i(z)$ , the breakthrough time of particle  $i$  at  $CP(z)$ . The Lagrangian integral along each trajectory can be used to compute  $\tau_i(z)$  for each particle,

$$\tau_i(z) = \int_0^{\ell'(z)} \frac{d\xi}{w[x(\xi), y(\xi), z(\xi)]} \quad (1-2)$$

to reach  $CP(z)$ . In Eq. 1-2,  $w$  is the vertical Eulerian velocity along  $p_i$ . Our focus is on first passage time of pathlines through each CP, which we define as the travel time required for a particle to reach a CP for the first time. It is possible that multiple crossings at a CP occur due to local flow opposite the primary direction of flow, but these crossings are not considered in our analysis.

The two injection modes are distinguished from one another by the initial mass distribution along the inlet plane. Given a fixed total mass represented by the particles,  $M$ , the mass associated with each particle,  $m_i$ , is determined using the total area of the fractures, length times aperture, along the inlet plane,  $A$ , and, in the case of flux-weighted injection, the local flux associated with the particle's initial position,  $Q_i$  and the total flux,  $Q$ , across the inlet plane. Specifically,

$$m_i = M/A \quad \text{resident injection,} \quad (1-3a)$$

$$m_i = (M/A)(Q_i/Q) \quad \text{flux-weighted injection.} \quad (1-3b)$$

The mass represented by each particle and the breakthrough time at each control plane can be combined to compute the total solute mass flux  $F(t, z)$  that has crossed CP(z) at a time  $t$ ,

$$F(t, z) = \frac{1}{M} \int m_i H[t - \tau_i(z)] d\mathcal{X} \quad (1-4)$$

Here,  $H(t)$  is the Heavyside function where  $H(t) = 1$  for  $t > 0$ , and  $H(t) = 0$  otherwise, and integration is carried out using Lebesgue measure. Equation (1-4) is the integral form of the familiar cumulative distribution function (CDF) of solute passing through a control plane. We also consider the expression  $1 - H(t, z)$ , the complementary cumulative distribution function (CCDF), which when plotted on a log-log scale can be used to determine power law scaling of the tail of the  $H(t, z)$  (Painter et al. 2002). The relevant solute flux through CP(z) is

$$F(t, z) = \frac{dF}{dt} = \frac{1}{M} \int m_i \delta[t - \tau_i(z)] d\mathcal{X} \quad (1-5)$$

which is an integral form of the breakthrough curve. Placing (1-3) into (1-5) one obtains the distributions of travel time for both initial conditions:

$$f_R(t, z) = 1/A \int \delta [t - \tau_i(z)] d\mathcal{X} \quad (1-6)$$

$$f_W(t, z) = 1/(AQ) \int Q_i \delta [t - \tau_i(z)] d\mathcal{X} \quad (1-7)$$

For clarity, the quantities  $f_R(t, z)$  and  $f_W(t, z)$  denote the distributions of travel time  $\tau$  at a control plane a distance of  $z$  away from the inlet plane for resident and flux-weighted injection schemes. We use the notation  $F_R(t, z)$  and  $F_W(t, z)$  for the cumulative distributions based on resident and flux-weighted injection that result from placing (1-3) into (1-4).

One of our major foci is how  $H(t, z)$  evolves with vertical distance traveled. This evolution is typically studied as the cloud evolves from the inlet plane. However, one may also study how the plume evolves between control planes. To do so, we introduce the following notation to aid in the isolation of the evolution of the particle cloud between control planes, not only from the inlet plane. Consider particle travel times at CP( $z^1$ ),  $\tau_i(z^1)$ , and at another control plane CP( $z^2$ ),  $\tau_i(z^2)$ , where  $z^1 < z^2$ . Then the CDF of the cloud between these two planes is given by

$$F(t, z^2, z^1) = \frac{1}{M} \int m_i H[t - \Delta\tau_i(z^{2,1})] d\mathcal{X} \quad (1-8)$$

where  $\Delta\tau_i(z^{2,1}) = \tau_i(z^2) - \tau_i(z^1)$ . This expression  $H(t, z^2, z^1)$  eliminates the history of the particle travel times prior to arriving at CP( $z^1$ ), and allows for the isolation of the cloud evolution moving to CP( $z^2$ ). Placing (1-3) into (1-8) provides an expression for the difference CDF of both resident,  $H(t, z^2, z^1)$ , and flux-weighted injection schemes,  $H(t, z^2, z^1)$ .

### 1.3.3 Methods

In this section, we describe the methods used to generate and mesh three-dimensional discrete fracture networks (DFN), numerically integrate the governing equations for fully saturated flow, and track particles through the network. The DFNs in this study are based on the fractured granite at the Forsmark, Sweden site (a potential host formation for a subsurface repository for spent nuclear fuel (SKB, 2011, Cvetkovic 2013)) and we provide details of the site in Sec. 1.3.3.1.

In the DFN approach, geologic field investigations are used to create a network of fractures where the geometry and properties of individual features (usually fractures) are represented explicitly, as lines in two dimensions or planar polygons in three dimensions. Fractures in the network are assigned a shape, location, aperture, and orientation based on distributions determined by the geological survey. To account

for the uncertainty associated with these distributions, multiple independent DFN realizations are generated stochastically by sampling these distributions. Once a network is constructed, the individual fractures are meshed for computation and the flow equations are numerically integrated on the resulting computational mesh. Examples of the various DFN methodologies and their applications are found in (Cacas et al. 1990, Dreuzy et al. 2004, 2012, Dershowitz 2014, Erhel et al. 2009, Mustapha et al. 2007, Pichot et al. 2010, 2012, Xu et al. 2006). One advantage of DFN models over stochastic continuum models is that they can represent a wider range of transport phenomena (Painter and Cvetkovic, 2005, Painter et al. 2002), which makes them a preferred choice when investigating the influence of injection mode on transport. Additionally, DFN simulations are generally favorable when investigating sparsely fractured rock because heterogeneity and topology can be explicitly represented.

### 1.3.3.1 DFN Model: Forsmark, Sweden

The Swedish Nuclear Fuel and Waste Management Company (SKB) has undertaken a detailed investigation of the fractured granite at the Forsmark, Sweden site as a potential host formation for a subsurface repository for spent nuclear fuel (SKB, 2011, Hartley and Joyce, 2013). The Forsmark area is about 120 km north of Stockholm in northern Uppland. The repository is proposed to be constructed in crystalline bedrock at a depth of approximately 500 m. Based on the SKB site investigation, a statistical fracture model with multiple fracture sets was developed and the detailed parameters of the Forsmark site model are provided in (SKB, 2011). We adopt a subset of the site investigation using three stochastic/statistical descriptions of background fractures. Our model consist of three sets of circular fractures whose orientations follow a Fisher distribution,

$$f(\mathbf{x}; \boldsymbol{\mu}, \kappa) = \frac{\kappa \exp(\kappa \boldsymbol{\mu}^T \mathbf{x})}{4\pi \sinh(\kappa)} \quad (1-9)$$

Here,  $\boldsymbol{\mu}$  is the mean direction vector, which can be expressed in terms of spherical coordinates,  $\theta'$  and  $\varphi'$ , and  $\kappa \geq 0$  is the concentration parameter that determines the degree of clustering around the mean direction. Values of  $\kappa$  approaching zero represent a uniform distribution on the sphere while larger values generate small average deviations from the mean direction.

Fracture radii  $r$  are sampled from a truncated power-law distribution with exponent  $\alpha$  and upper and lower cutoffs ( $r_u$ ;  $r_0$ ),

$$r = r_0 \left[ 1 - u + u \left( \frac{r_u}{r_0} \right)^\alpha \right]^{-1/\alpha} \quad (1-10)$$

where  $\mu$  is a random number sampled from the continuous uniform distribution on the open interval (0,1). We assume that the transmissivity of the fractures,  $\sigma$ , is estimated using a deterministic power-law model based on the fracture radius,

$$\log(\sigma) = \log(\gamma r^\beta) \quad (1-11)$$

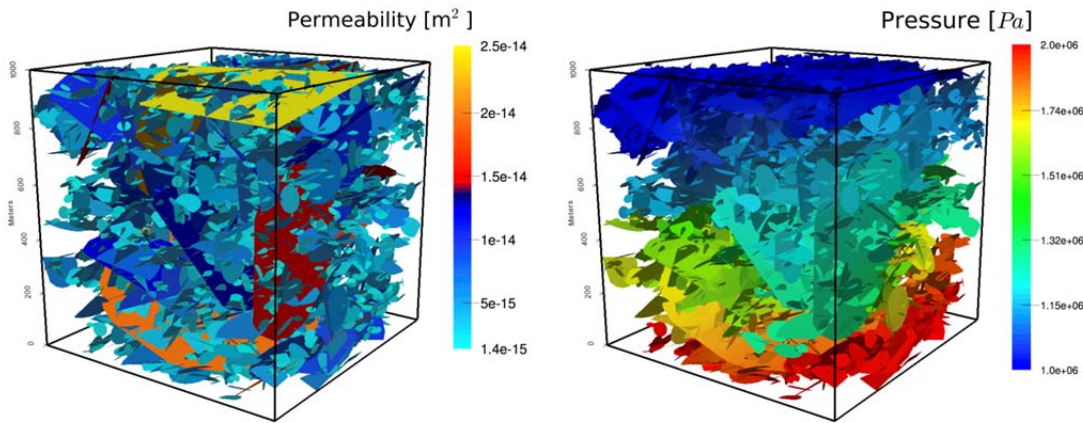
with parameters,  $\gamma = 1.6 \times 10^{-9}$ , and  $\beta = 0.8$ . Other relationships between the fracture radius and transmissivity have also been proposed. For example, there can be no correlation between the two, they can be perfectly correlated, or they can be semi-correlated. We adopted the second of these assumptions because (a) we believe that the assumption that larger fractures have high transmissivities is generally valid and are not concerned with site specific sensitivities, but (b) a systematic study concerning how variations in the semi-correlation between radius and transmissivity influence flow properties would be better performed using a simple DFN setting so the particular influences of the semi-correlation (and its strength) can be properly characterized. The fracture aperture,  $b$ , is related to the fracture transmissivity using the cubic law,  $\sigma = b^3/12$  (Adler et al. 2012). Under such a formulation, the fracture apertures are uniform on each fracture, but vary between fractures. Values of the parameters used to generate the sample DFNs for all three fracture sets are provided in Table 1-1. The average surface area of fractures

per unit volume of rock, denoted as  $P_{32}$  ( $m^2/m^3$ ), computed using the entire DFN for the three different cutoffs are  $r_0 = 15 \text{ m} : 0.048 \text{ m}^{-1}$ ,  $r_0 = 20 \text{ m} : 0.056 \text{ m}^{-1}$ ,  $r_0 = 25 \text{ m} : 0.057 \text{ m}^{-1}$ .

Using this statistical model, sixty DFNs with three lower cutoffs in the truncated power-law distributions (15m, 20m, and 25m) and upper limit 560m are generated (twenty realizations are generated at each other lower cutoff values) in cubic domains with sides of length one kilometer. The upper limit of fracture size reflects a technical distinction between background and deterministic fractures in the SKB report. We note that these simulations are not meant to be site-specific and therefore inclusion of deterministic features (fractures larger than 560m) is not necessary. The DFN sets represent rock mass between larger deterministic fracture zones and should be thought of as a representation of a background/stochastic fractures. In a site-specific study, background fractures are typically incorporated stochastically, whereas features larger than this approximate threshold are included with assigned properties as fracture zones and do not vary between realizations. All other generation parameters, with the exception of the number of fractures, are fixed. For equivalency, the number of fractures in each realization is selected so that the fracture density is relatively constant between realizations. Dirichlet boundary conditions are imposed on the top (1 MPa) and bottom (2 MPa) of the domain to create a pressure gradient aligned with the vertical axis, and no-flow boundary conditions are enforced along lateral boundaries. Approximately one hundred thousand particles are inserted into each network, using uniform spacing across all fractures at the bottom of the domain.

Table 1-1. DFN parameters used in simulations of the Forsmark repository site, Sweden.

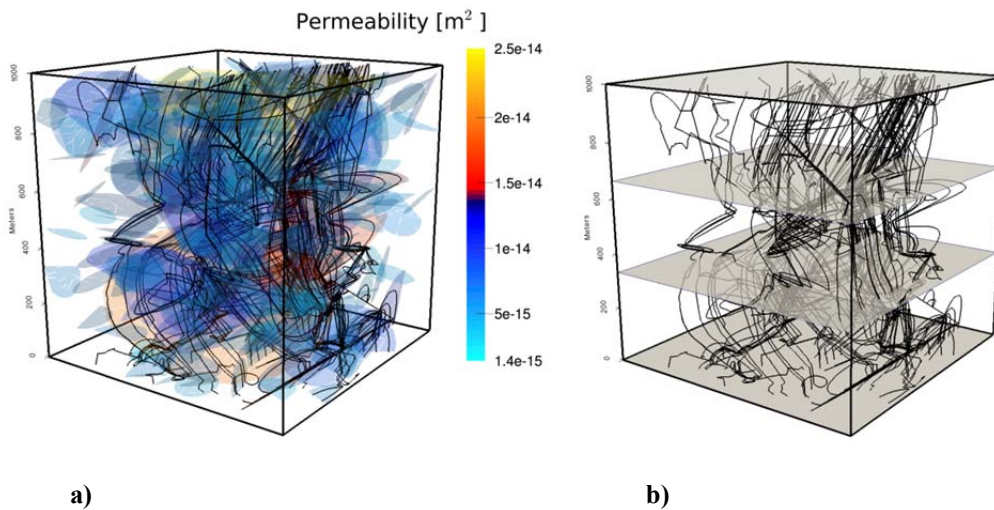
Set	Orientation		Distribution:		Size Distribution:			Fracture Density
	Fisher				Power Law			
	Mean Trend	Mean Plunge	Conc. $\kappa$	$\alpha$	$r_u$ , m	$r_0$ , m	Number of fractures in $1 \text{ km}^3$	
1. (NS)	90.0°	0.0°	21.7	2.5	560	15	2093	
						20	1019	
						25	583	
2. (NE)	135.0°	0.0°	21.5	2.7	560	15	2000	
						20	919	
						25	503	
3. (HZ)	360.0°	90.0°	8.2	2.38	560	15	7711	
						20	3887	
						25	2285	



a) Permeability

b) Pressure Solution

Figure 1-8. a) A DFN realization based upon the fractured granite at the Forsmark, Sweden site in a 1 km<sup>3</sup> domain. The model consists of three sets of circular fractures whose orientations follow a Fisher distribution. The fracture diameters in each fracture set follow a truncated power-law distribution with lower cutoff at 15 m. Fractures are colored by permeability, which is based upon fracture radius. b) steady state pressure solution within the network shown in (a). Dirichlet boundary conditions are imposed on the top (1 MPa) and bottom (2 MPa) of the domain to create a pressure gradient in the z direction, and no-flow boundary conditions are imposed along lateral boundaries.



a)

b)

Figure 1-9. Two hundred particle trajectories within the DFN shown in Fig. 1-8. Particles are inserted uniformly along fractures on the bottom of the domain. a) Trajectories are overlaid on Fig. 1-8.a, fractures are colored by the permeability, to show how particles are drawn to larger fractures, which have higher permeabilities and offer less resistance than smaller fractures. Although particles are inserted uniformly along fractures in the inlet plane, they cluster on larger fractures as they exit the domain. This clustering

suggests that transport only occurs within a small portion of the fracture network far away from the inlet plane. b) Trajectories with four example control planes, shown in grey. To quantify the visually observed clustering, particle attributes are recorded at uniformly spaced control planes throughout the domain.

A sample realization of the Forsmark DFN is shown in Fig. 1-8.a. The realization contains 4,934 fractures and the computational mesh consists of 7,731,299 cells. Fractures are colored by permeability, with warmer colors indicating higher values. Because the fracture permeability is based upon the fracture radius, the largest fractures have the highest permeabilities. There are significantly more small, low permeability, fractures than larger fractures due to Eq. 3.10. Dirichlet pressure boundary conditions are applied to the  $z$ -faces of the  $1 \text{ km} \times 1 \text{ km} \times 1 \text{ km}$  domain of the network shown in Fig. 1-8.a, and Fig. 1-8.b shows the steady state pressure solution. The larger fractures act as conduits for flow, connecting numerous small fractures together in the network.

A selection of two hundred particle trajectories passing through this network are shown in Fig. 1-9. The particles are inserted uniformly along fractures in the inlet plane (bottom), and the movement of the particles is determined by the local velocity. In Fig. 1-9.a, the permeability of the fractures is shown along with the trajectories to highlight that particles are attracted toward larger fractures. In Fig. 1-9.b, four of the previously mentioned control planes are shown along with the trajectories. At each of these control planes, spatial and temporal attributes of the particles are recorded to provide a pseudo-temporal evolution of the solute plume. Although the particles are inserted uniformly, their trajectories cluster together onto larger fractures. This clustering suggests that transport only occurs within a small portion of the fracture network far away from the inlet plane. This observed clustering is investigated quantitatively in the next section where we report spatial and temporal particle attributes recorded at uniformly spaced control planes.

### 1.3.4 Lagrangian Based Observations

Spatial and temporal particle attributes are recorded at uniformly spaced control planes, CP, throughout the domain to observe the evolution of transport properties. The CP are perpendicular to the imposed pressure gradient in the  $z$  direction, the primary direction of flow, and spaced twenty five meters apart.

Three spatial traits are considered, each of which highlight different aspects of the solute plume. The first attribute is the aperture of the fractures on which a particle resides as it passes through a CP. At one control plane, the combination of these values shows the distribution of mass in the network. Placing these distributions into a sequence according to the vertical distance traveled shows how mass disperses or clusters as it moves through the network. The second trait we consider is the tortuosity of a trajectory. Tortuosity is the ratio of the length of a trajectory  $\ell$  over the vertical distance traveled to reach the control plane  $z$ ,  $\mathcal{T} = \ell/z$ , and measures the deviation of a trajectory from a straight-line path (Bear, 1988). Once pathlines are computed, determining tortuosity is a straightforward procedure. The tortuosity of the plume of particles can be related to the coefficient of hydrodynamic dispersion (Bear, 1988), and is an indicator of dispersion in high Pe'let number flows. The third trait we consider is the box-counting dimension of the cloud based on their  $x - y$  spatial locations at each control plane computed according the techniques outlined in (Falconer, 2013). The box-counting dimension, box-dimension for short, is a computationally tractable upper bound on the Hausdorff dimension, which is a generalization of the notion of dimension in a real vector space, that we use to estimate the fractal dimension of the particle cloud at CPs. The fracture network has a Hausdorff dimension of one at CPs. Initially, the particles are uniformly spaced on these fractures and the plume also has a Hausdorff dimension of one. As the set of particles moves through the network it may evolve to have a fractal dimension that is less than one due to mechanical dispersion induced by the network; local in-fracture dispersion is not included in these simulations. A fractal dimension less than one indicates that the plume has clustered on individual fractures.



Particle travel time is computed according to Eq. (1-2) and is recorded at every control plane. The cumulative distribution function of travel time ( $t, z$ ) Eq. (1-4), and the complement of the cumulative distribution function,  $1 - (t, z)$ , provide information regarding the distribution of trajectory times at a control plane. In sequence, they show how the plume evolves as the cloud moves through the domain. We also consider the travel times between CPs computed according to Eq. (1-8), as well as the mean of the plume at each of the CPs.

Comparisons of the influence of injection mode are performed for fracture aperture, tortuosity, and travel time by assigning the mass associated with each particle using Eq. (1-3). However, the adopted computation of the box-dimension only depends on the spatial distribution of particle trajectories, not upon the distribution of mass associated with each particle. Nonetheless, the box-dimension complements the other traits by measuring clustering of the plume.

#### 1.3.4.1 Spatial Attributes

We begin by presenting the measurements of the spatially based attributes: fracture aperture, tortuosity, and box-dimension.

##### *Fracture Aperture*

Figure 1-10 shows heat maps of the mass distribution plotted as a function of fracture apertures (abscissa) and vertical distance traveled (ordinate) where colors indicate percent of mass. The plots are provided for one realization, with a lower cutoff of fifteen meters. Across each vertical level in the domain, horizontal level in the graph, the sum of all the mass equals one. Figure 1-10.a shows the mass distribution for resident injection and Figure 1-10.b provides the same information for the flux-weighted injection. In the case of resident injection, the initial distribution of mass is relatively uniform across all apertures. As the particles move through the domain, the mass consolidates into fractures with larger apertures, indicated by the trend of increasingly warmer colors to the right with increasing distance traveled. In the case of flux-weighted injection, the initial distribution of mass is non-uniform; more mass is in fractures with larger apertures due to the reduced resistance to flow offered by the higher permeabilities. Recall that the aperture of the fracture depends on the radius of the fractures, larger fractures have larger radii. Similarly to the resident injection, the bulk of the mass is drawn into fractures with larger apertures as the particles move through the domain. After traveling approximately two hundred meters vertically, the distributions of mass for resident and flux-weighted injection resemble one another closely.

Figure 1-11 shows the same information as Fig. 1-10, but the values computed using all particles in all thirty realizations. Mass is more widely distributed under resident injection conditions than flux-weighted because of the abundance of small fractures in the networks. In particular, the initial distribution of mass favors small apertures due to their prevalence in the networks. The observed trend of warmer colors up and right indicates that after an initial region, which depends upon the injection mode and the particular realization, the majority of mass is transported through larger fractures. Under flux-weighted conditions, more mass is initially placed into larger fractures due to the reduced resistance to flow, and higher flux, offered therein. As is the case in the resident injection, as the particle cloud moves through the domain, the majority of the mass migrates into the largest fractures in the networks. After this initial region, the distributions of mass for resident and flux-weighted injection resemble one another, with the majority of the mass in large fractures.

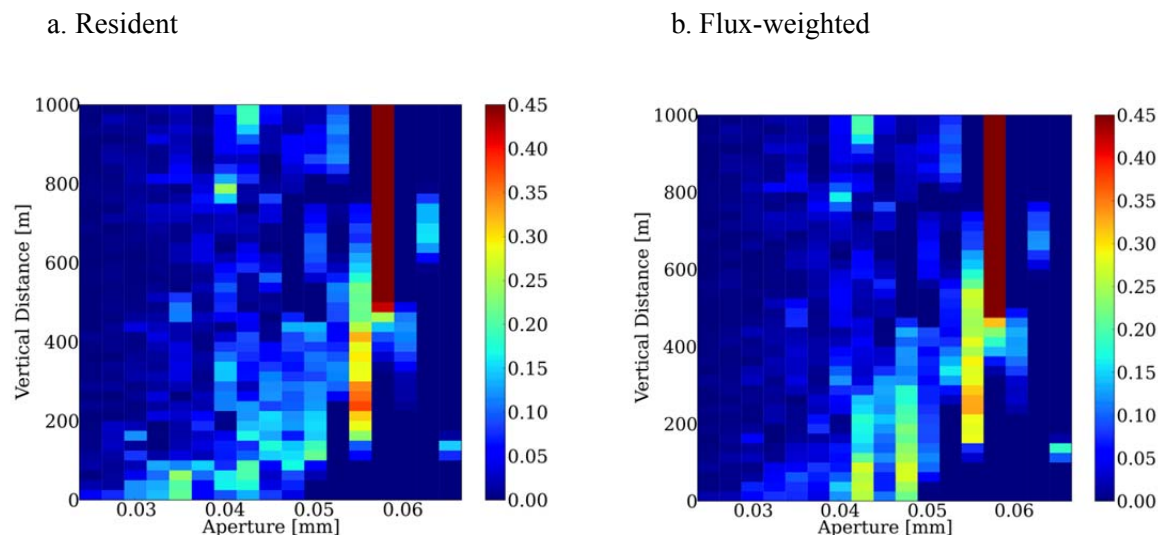


Figure 1-10. Heat map of mass distribution plotted as a function of fracture apertures (abscissa) and vertical distance traveled (ordinate) where colors indicate percent of particles for one realization. The primary direction of flow is from bottom, vertical distance equal to 0, to the top, vertical distance equal to 1000. (a) Resident injection: The initial distribution of mass is relatively uniform across all apertures, with slightly more weight at lower values due to larger numbers of small fractures in the network. As the particles move further through the domain, the bulk of the mass is drawn into fractures with larger apertures indicated by the trend of warmer colors up and right with increasing vertical distance traveled. (b) Flux-weighted injection: The initial distribution of mass is non-uniform across all apertures, with more mass being observed in fractures with larger apertures, compared to the resident injection. After traveling through a burn-in region, the distributions of mass for resident and flux-weighted injection resemble one another.

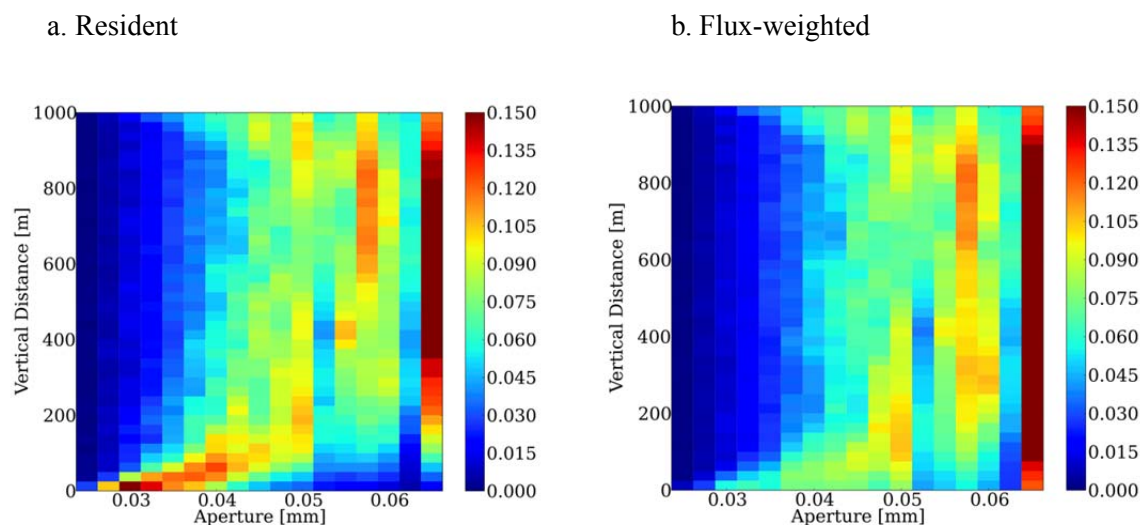


Figure 1-11. Heat map of mass distribution plotted as a function of fracture apertures (abscissa) and vertical distance traveled (ordinate) where colors indicate percent of particles for all realizations. The primary direction of flow is from bottom, vertical distance equal to 0, to top. (a) Resident injection: The initial distribution of mass favors small apertures due to their prevalence in the networks. As the particles move further through the domain, the bulk of the mass is drawn into fractures with larger apertures

indicated by the observed trend up and right with increasing vertical distance traveled. (b) Flux-weighted injection: Compared to (a), more mass is initially placed into larger fractures due to the reduced resistance to flow, and higher flux, offered therein. As is the case in the resident injection, as the particle cloud moves through the domain, the majority of the mass migrates into the largest fractures in the networks. This clustering indicates large, fracture-to-fracture, flow channeling.

### *Tortuosity*

The computed values of mean tortuosity are plotted as a function of travel distance in Fig. 1-12.a. Color indicates lower cutoff in the truncated power-law distribution of fracture size:  $r_0 = 15$ ; blue,  $r_0 = 20$ ; red,  $r_0 = 25$ ; green. Dashed lines denote flux-weighted injection, and solid lines indicate resident based injection. The values of mean tortuosities computed for particles inserted under resident injection are consistently higher than those observed using flux-weighted injection. As the particles move through the domain, the difference between the two injection schemes decreases. This convergence appears more rapid for the two higher lower cutoffs, the red and green lines.

The difference between the mass inserted into small fractures and large fractures under resident and flux-weighted conditions is likely responsible for the observed differences in tortuosity. Under resident injection conditions mass is uniformly distributed regardless of the size of the fracture, cf. Fig. 1-10.a. While under flux-weighting conditions, mass is disproportionately distributed into larger fractures whose wider apertures provide a decreased resistance to flow that results in higher flux, cf. Fig. 1-10.b. Movement between small fractures at various orientations will result in longer trajectories when compared to the movement within larger fractures where the particle remains on a single plane when the same total vertical distance is covered. This additional fracture switching is likely the cause of the higher observed values for tortuosity in the resident injection mode. As particles move through the domain they are drawn towards larger fractures that offer reduced resistance to flow, as discussed in Sec. 1.3.4.1. Transport through these larger fractures results in straighter trajectories, because the particles do not have to switch fractures to enter the primary flow channels. These straighter trajectories are reflected in the lower values of tortuosity that are observed. Because tortuosity can be related to the coefficient of dispersion (Bear, 1988), these results indicate that the difference of dispersion under the two different injection conditions also diminishes with time.

A trajectory's length, and therefore its tortuosity, depends on the entire history of a particle's journey, as opposed to the aperture of the fracture on which a particle resides which is a local, in time, attribute. This hysteresis of tortuosity could be the reason that the initial difference between the flux-weighted and resident particles' tortuosities persist as the plume moves through the domain, even though the distribution of mass appear similar.

### *Box-Dimension*

The box-counting dimension of the particle plumes at every control plane is reported in Fig. 1-12.b. Individual realizations are shown as semi-translucent lines, and thick lines indicate average values by lower cutoff. Color indicates lower cutoff,  $r_0 = 15$ ; blue,  $r_0 = 20$ ; red,  $r_0 = 25$ ; green. Initially, all particles are evenly spaced on fractures and have a box-dimension of one, and the box-dimension of the DFN at CPs is constant with a value of one (details not shown). However, as the cloud moves through the domain, the mean box-dimension decreases and stabilizes at a values of  $\approx 0.80$ . This value indicates that the particles are clustering within fractures; if the particles remained uniformly spaced on fractures they would retain a box-counting dimension of one. This in-fracture clustering can be observed using scatter plots of the particle locations overlaying the network at CPs. All thirty DFN realizations exhibit this behavior suggesting that the in-fracture channeling occurs regardless of realization.

In conjunction with the plots presented and discussed in Sec. 1.3.4.1, these results indicate that particle clustering occurs on two scales in these networks. There is a larger scale of mass moving into larger

fractures indicated by the observed trend of mass into fractures with larger apertures, Fig. 1-11, and a smaller scale in-fracture channeling, particle trajectories clustering on a single fracture plane, which is indicated by the stabilization of the box-dimension to a value less than one. Both of these types of channeling are observed in Fig. 1-9. Variations between fracture apertures induce the network scale channeling, while the network topology induces the smaller scale of in-fracture channeling. Recall that fracture aperture varies from fracture to fracture, but not within a fracture in these simulations; in-fracture aperture variability has been shown to induce in-fracture channeling (Tsang and Neretnieks, 1988, Tsang and Tsang, 1989, Berkowitz, 2002, Berkowitz and Braester, 1991). This channeling influences mass transport times which can be linked to injection mode, as we discuss in the following section.

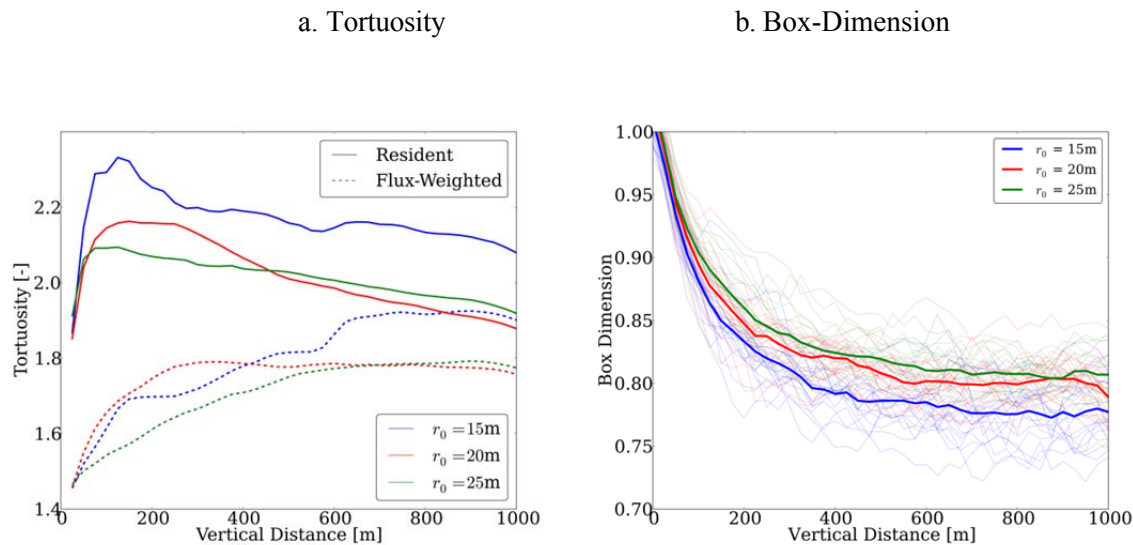


Figure 1-12. (a) Mean particle tortuosity plotted as a function of control plane distance. Averages are computed using all particles in each DFN at each of the lower cutoffs for the generation of the DFN. Solid lines indicate particles inserted under resident injection conditions and dashed lines indicate flux-weighted values. Color indicates lower cutoff,  $r_0 = 15$ ; blue,  $r_0 = 20$ ; red,  $r_0 = 25$ ; green. The computed mean tortuosities using resident injection are consistently higher than those observed using flux-weighted injection. As the particle clouds move through the domain the difference between the two injection schemes decreases. (b) Box-dimension of particle cloud plotted as a function of control plane distance. Color indicates lower cutoff,  $r_0 = 15$ ; blue,  $r_0 = 20$ ; red,  $r_0 = 25$ ; green. Semi-transparent lines are individual realizations and thick line indicate average values. The network of fractures has a box-dimension of one at each of the control planes. The box-dimension of the particle clouds start at one because they are uniformly distributed along fractures on the inlet plane. As they move through the domain, the box-dimension decreases with distance and stabilizes to a mean value near 0.80, which indicates in-fracture clustering.

#### 1.3.4.2 Temporal Attributes

Particle travel times are recorded at every control plane, and their distributions are discussed in this section. We focus on the empirical cumulative distribution, the complement of the empirical cumulative distribution, and the mean travel time. Particles are inserted at the bottom of the domain,  $z = 0$ . Empirical cumulative distributions of travel time, breakthrough curves, at CP(100) and CP(750) are shown in Fig. 1-13 for resident,  $(t, z)$ ; Fig. 1-13.a, and flux-weighted,  $(t, z)$ ; Fig. 1-13.b, injection modes. Line color indicate lower cutoffs,  $r_0 = 15$ ; blue,  $r_0 = 20$ ; red, and  $r_0 = 25$ ; green. Line style indicates CP,  $z = 100$ ; solid line,  $z = 750$ ; dashed line. Individual realizations are semi-transparent, and thick lines are ensemble

values. In the case of  $(t, z)$ , variation in travel time within and between realizations is apparent. These variations are most prevalent for  $r_0 = 15$  m. The initial portion of  $(t, z)$ , values less than 0.6, are fairly uniform, but thereafter several of the realizations exhibit behavior that does not follow the general trend.

The plotted values of  $(t, z)$ , are more homogeneous than  $(t, z)$ , but differences between realizations are still present. Steep segments of the curves are observed in  $(t, 100)$ , where a large portion of the mass passes through CP(100) in a relatively short time period. Flux-weighting injection places more mass into larger fractures due to their higher transmissivities and that mass is transported at a uniform velocity with little mechanical dispersion for short distances; these sharp fronts are not observed in  $(t, 100)$ . (Frampton and Cvetkovic, 2011) observed similar behavior in smaller, (100m), three-dimensional DFNs and reached a similar conclusion regarding the physical mechanisms that created this feature. As the plume moves further through the domain, mechanical dispersion induced by the network breaks this plume apart and particles travel at various speeds, and these sharp interfaces are not observed in  $(t, 750)$ .

Additional differences between travel times associated with resident and flux-weighted injection modes are observed by looking at the complement of the cumulative distributions,  $1 - (t, z)$ ; shown in Fig. 1-14, colloquially referred to as the survivor function. The survivor function can be used to determine power-law scaling in the tails of these distributions, if it exists. Fig. 1-14.a shows the survivor function obtained using resident injection conditions, and no universal power-law scaling is observed. In the case of flux-weighted injection from the inlet, Fig. 1-14.b, it is possible that the tails demonstrate power-law scaling. However, this behavior breaks down at longer time scales, possibly an artifact of the number of particles used in the simulations. This is expected in empirical distributions where the structure in tails suffer from small densities.

A black dotted line for a power-law with exponent of two is included in the plot for reference. Averaging over all realizations, the best fit for a power-law scaling is computed at every control plane and when plotted as a function of vertical distance from the inlet plane they display exponential convergence to an asymptotic value slightly greater than two,  $\approx 2.07$ , (images not provided). The best fit for a power law in the tail of  $1 - (t, 750)$  is a value of  $\approx 2.01$ .

Mean particle travel time for each plume is plotted as a function of vertical distance traveled in Figure 1-15; resident injection in Fig. 1-15.a and flux-weighted in Figure 1-15.b. Line color indicate lower cutoffs,  $r_0 = 15$ ; blue,  $r_0 = 20$ ; red, and  $r_0 = 25$ ; green. Individual realizations are semi-transparent, and thick lines are average values. Values based on resident injection initially scale nonlinearly, and after some vertical distance, which depends on the particular realization, the values scale linearly. In contrast, the mean value of travel time for particles inserted under flux-weighting conditions scales linearly with vertical distance traveled, although there is one outlier from the typical behavior. There are differences between realizations, but they are minor when compared to those observed in Fig. 1-15.a.

By computing the second derivative of these curves as a function of vertical distance traveled, we determine a value of  $z$  such that thereafter the second derivative is within a user prescribed tolerance of zero, indicating linearity. The average mean values, standard deviations, minimum value, and maximum value for this value of  $z$  are reported in Table 1-2 for each of the three lower cutoffs in the generation of the DFN. Two hundred and fifty meters appears to be a sufficient distance for the first moment of travel time for clouds inserted using resident injection to scale linearly for most realizations. Below this value there is substantial variation, and above it the majority of the realizations exhibit mean values of travel time that scale linearly. In the case of resident injection conditions, the mean, standard deviations, and maximum values depend on the lower bound of the power-law. In the case of flux-weighted injection, no relationship between these values and the lower cutoff is observed. At all lower cutoff values, the mean values are near zero, indicating the first moment of travel time scales linearly when particles are inserted using flux-weighting.

Table 1-2. Values of vertical distance traveled such that linear scaling of the first moment of travel time is observed [All values are in meters]. In the case of resident injection conditions, the mean, standard deviations, and maximum values depend on the lower bound of the power-law, decreasing with increasing lower cutoff. In the case of flux-weighted injection, no statistically significant relationship between these values and the lower cutoff is observed. At all lower cutoff values, the mean values are near zero, indicating the first moment of travel time scales linearly when particles are inserted using flux-weighting.

$r_0$	Resident				Flux			
	Mean	Std. Dev.	Min	Max	Mean	Std. Dev.	Min	Max
15	180.0	67.36	100	325.0	21.25	55.49	0.0	250.0
20	130.0	66.59	50.0	300	6.25	15.56	0.0	50.5
25	143.75	43.92	75.0	225.0	2.50	7.5	0.0	25.0

To confirm this behavior we plot the mean travel time generated of  $(t, z, 250)$ , as defined in Eq. (1-8). This removes the particles history prior to reaching CP(250) to isolate how they advance beyond that control plane. These moments are shown in Figure 3.8.c, and they all scale linearly with distance as is the case for the flux-weighted particles.

Figure 1-16.a shows  $(t, 350, 250)$  and  $(t, 1000, 250)$  after applying this 250 meter burn-in region. Here, blue lines correspond to  $(t, 350, 250)$  and the red lines correspond  $(t, 1000, 250)$ . These CPs are selected so that the distance traveled from the burn-in plane is the same as those shown in Fig. 1-13.a. After accounting for the burn-in region, the general behavior of the curves is more similar to those observed for the flux-weighted injection displayed in Fig. 1-13.b than with Fig. 1-13.a. Figure 1-16.b shows  $1 - (t, 350, 250)$  and  $1 - F_r(t, 1000, 250)$  for additional comparison. All realizations exhibit similar behaviors, and power-law scaling of the tails can be observed. A black dashed line for a power-law with exponent of two is included in the plot for reference. Averaging over all realizations, the best fit for a power-law scaling are computed at every control plane and when plotted as a function of vertical distance from the inlet plane they display stabilization to a value slightly greater than two,  $\approx 1.94$ , which is remarkably close to the exponent observed under flux-weighted conditions.

These similarities suggest that after a burn-in region mass inserted under resident conditions evolves into a cloud that behaves in a manner similar to a cloud inserted under flux-weighted conditions. This trend was also observed when considering spatial attributes of the particles plumes. For example, the Kolmogorov-Smirnov test does not reject the null hypothesis that these empirical distributions are from the same underlying distribution after 250 meters, indicating the degree of similarity between the samples.

In the following and final section we provide remarks regarding this behavior, hypothesize about the physical mechanisms which induce it, and discuss its implications and applications.

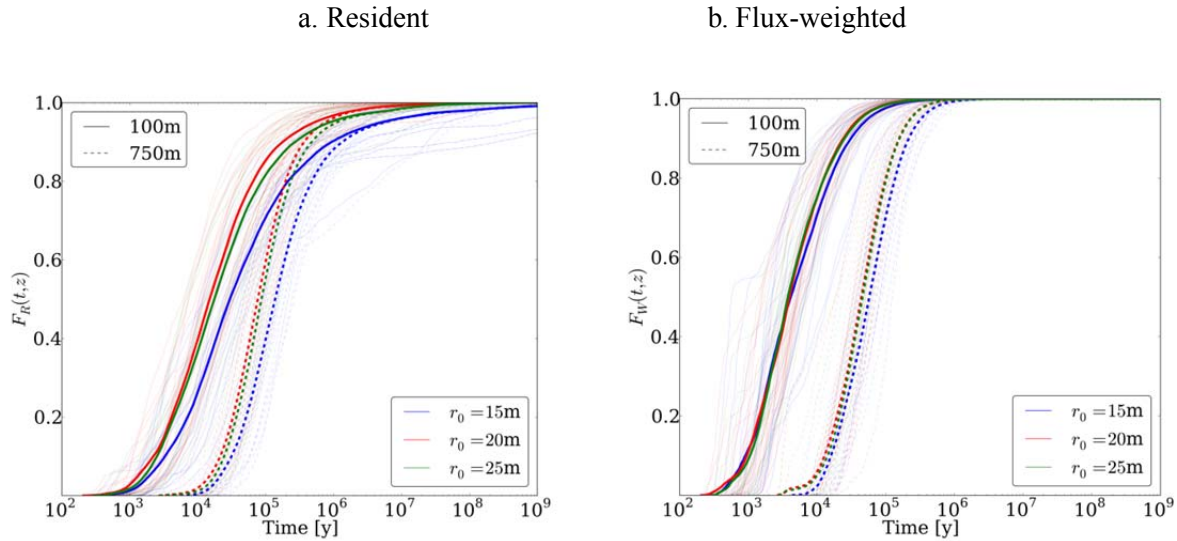


Figure 1-13. Cumulative distribution functions ( $t, z$ ) of passage times. Line color indicate lower cutoffs,  $r_0 = 15$ ; blue,  $r_0 = 20$ ; red, and  $r_0 = 25$ ; green. Line style indicates CP,  $z = 100$ ; solid line,  $z = 750$ ; dashed line. Individual realizations are semi-transparent, and solid lines are average values. (a) ( $t, z$ ) generated using resident based inject scheme. (b) ( $t, z$ ) generated using flux-weighted injection scheme. The plotted values of ( $t, z$ ), are more homogeneous than ( $t, z$ ) due to the majority of the mass transporting through larger fractures.

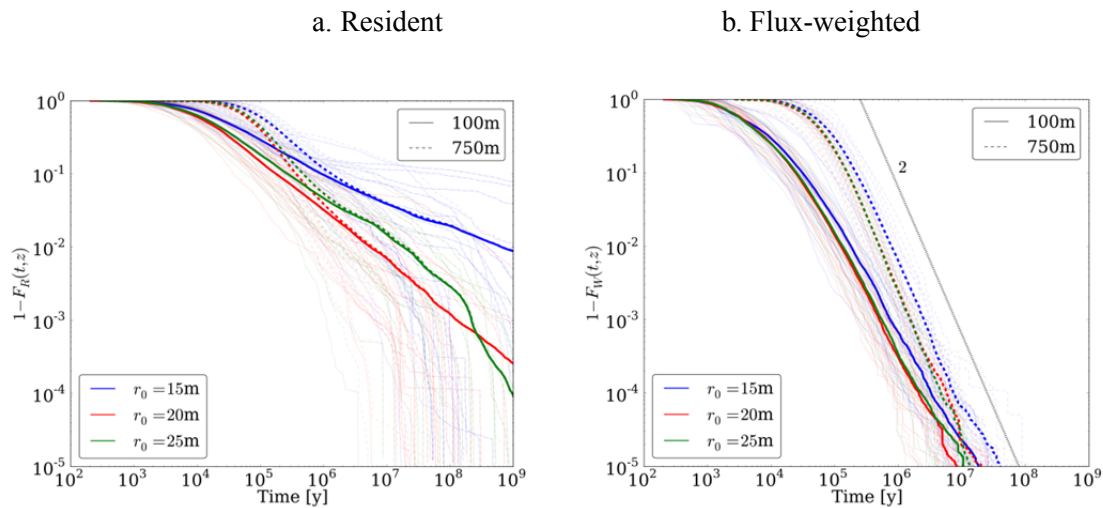


Figure 1-14. Complement of the cumulative distribution function,  $1 - F(t, z)$ , of passage times. Line color indicate lower cutoffs,  $r_0 = 15$ ; blue,  $r_0 = 20$ ; red, and  $r_0 = 25$ ; green. Line style indicates CP,  $z = 100$ ; solid line,  $z = 750$ ; dashed line. Individual realizations are semi-transparent, and solid lines are average values. (a)  $1 - F_R(t, z)$  generated using resident based inject scheme. Universal power-law scaling is not observed. (b)  $1 - F_W(t, z)$  generated using flux-weighted injection scheme. It is possible that the tails demonstrate power-law scaling. The dotted black line is a power law with exponent two. The best fit for a power law in the tail of  $1 - F_W(t, 750)$  is a value of  $\approx 2.01$ .

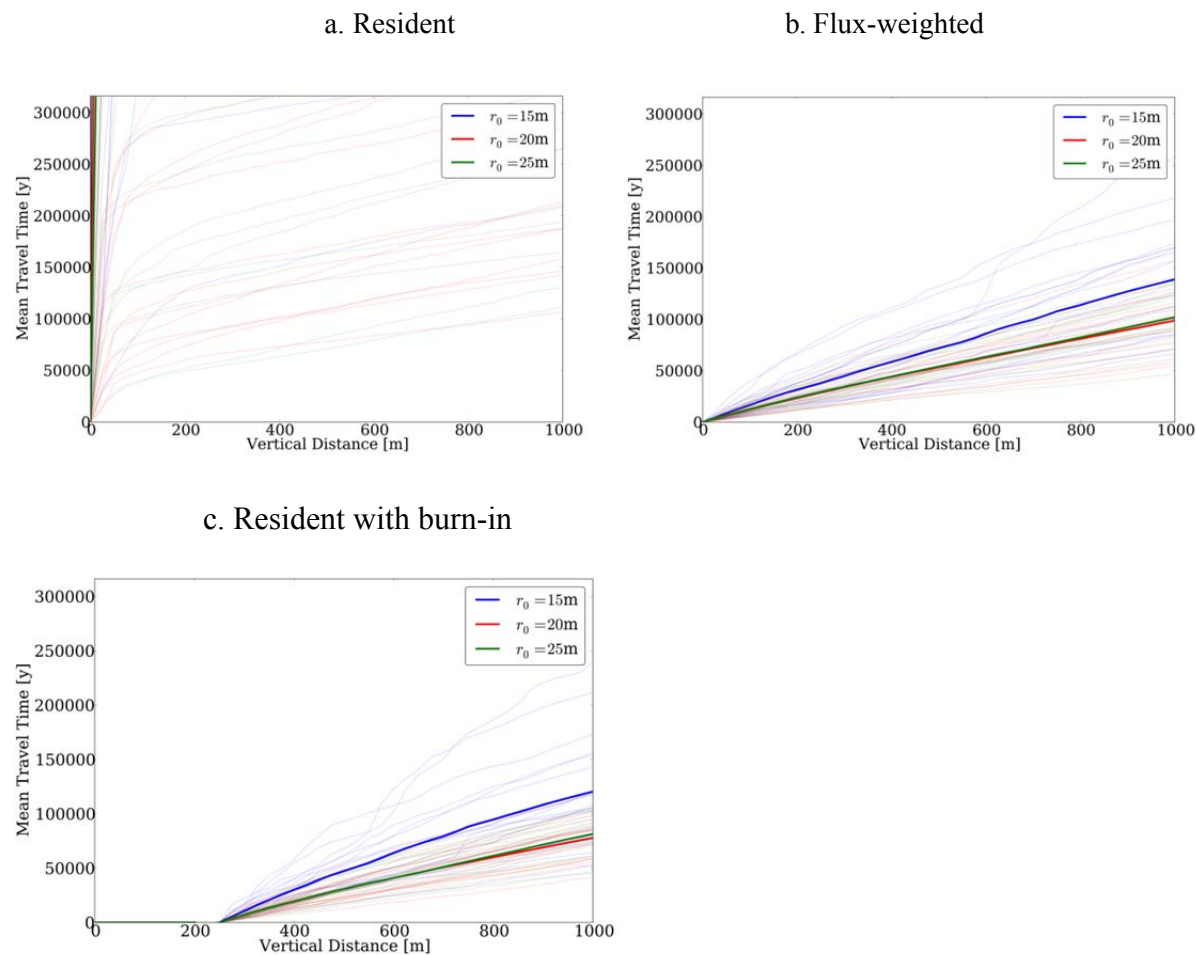


Figure 1-15. Mean travel time plotted as a function of longitudinal distance. Color indicates lower cutoff,  $r_0 = 15$ ; blue,  $r_0 = 20$ ; red,  $r_0 = 25$ ; green. Semi-transparent lines are individual realizations and thick lines are average values. (a) Resident injection mean travel times from inlet initially scale nonlinearly. After an initial distance, the mean travel time does scale linearly with distance. (b) Flux-weighted injection mean travel times scale linearly at all distances from the inlet. (c) Beyond a 250 meter burn-in region, mean travel times of particles inserted using resident injection scale linearly with distance.



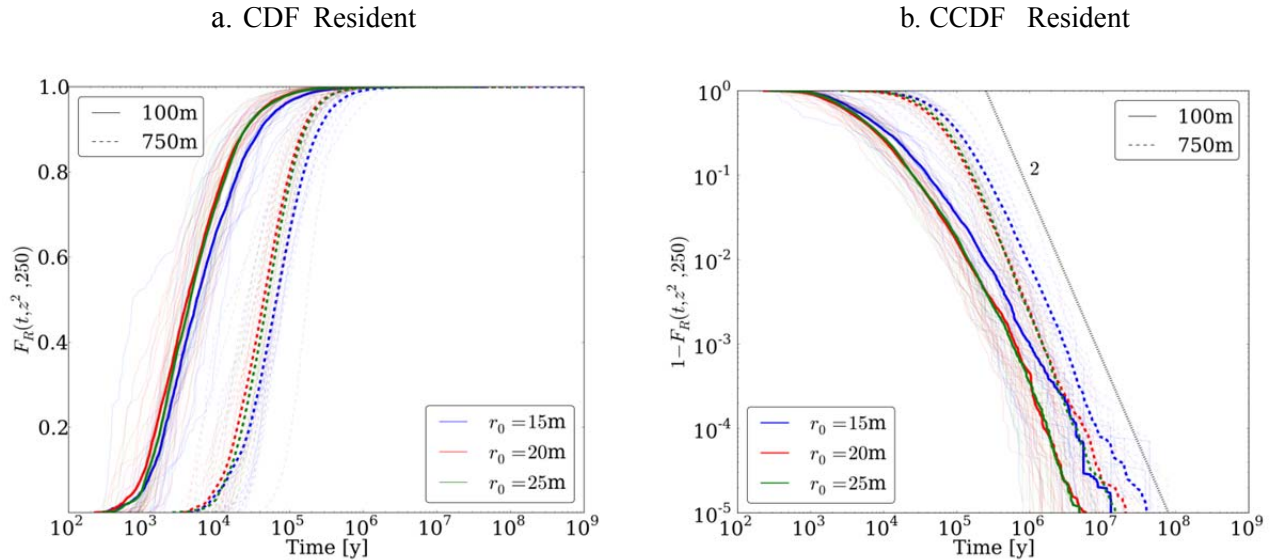


Figure 1-16.  $F_R(t, z^2, 250)$  and  $1 - F_R(t, z^2, 250)$  for particle travel time inserted using resident injection to account for a 250 meter burn-in region. Here, blue lines correspond to  $(t, 350, 250)$  and the red lines correspond  $(t, 1000, 250)$ . Line color indicate lower cutoffs,  $r_0 = 15$ ; blue,  $r_0 = 20$ ; red, and  $r_0 = 25$ ; green. Line style indicates CP,  $z = 100$ ; solid line,  $z = 750$ ; dashed line. Individual realizations are semi-transparent, and thick lines are ensemble values. These distances are selected so that the distance traveled from the burn-in plane is the same as those shown in Fig. 1-13.a. After accounting for the burn-in region, the general behavior of the curves is more similar to those observed for the flux-weighted injection displayed in Fig. 1-13.b, although some differences are still present. After applying this burn-in region, it is possible that these tails exhibit power law scaling, which is clearly impossible in Fig. 1-14.a. Averaging over all realizations, the best fit for a power-law tail of  $1 - F_R(t, 1000, 250)$  is  $\approx 1.94$ , which is remarkably close to the exponent observed under flux-weighted conditions.

### 1.3.5 Discussion

The observations of the particle trajectories and analysis of their behavior support the notion of a burn-in region in the context of fractured media, as well as providing a physical explanation for its occurrence. The existence of a burn-in region such that solutes inserted under resident conditions evolve into plumes that exhibit similar behavior to those inserted under flux-weighted conditions has been hypothesized but has never been observed before due to computational limitations. The major observations that support the existence of this burn-in region are the following:

1. Initially, the mean travel time of particle clouds inserted under resident injection conditions scale non-linearly with distance. After a burn-in region, however, they scale linearly, as does the first moment of the travel time for particle inserted under flux-weighted conditions, cf. Fig. 1-15.
2. Power-law scaling in the tail of the empirical distributions of travel time is observed for solutes inserted under flux-weighted conditions, Fig. 1-14.b, and under resident injection conditions once accounting for this burn-in region, Fig. 1-16.b. The best fit for the exponent of the power-laws for these distributions are close to one another.
3. After traveling through the burn-in region, the distributions of mass as a function of fracture aperture for resident and flux-weighted injection resemble one another closely, cf. Fig. 1-10 and Fig. 1-11. The Kolmogorov-Smirnov test does not reject the null hypothesis that these empirical

distributions are from the same underlying distribution after this burn-in region.

4. The computed mean tortuosities using resident injection are consistently higher than those observed using flux-weighted injection, yet as the cloud moves through the domain the difference between the two injection schemes decreases, cf. Fig. 1-12.a.

The physical mechanisms behind this evolution appear to be the combination of in-network channeling, mass moves into fractures with larger apertures because they offer less resistance to flow, and in-fracture channeling, particle trajectories cluster on single fracture planes, that results from the structure of the DFN. The strength of this flow channeling might be a result of the adopted correlation function between transmissivity and fracture radius. However, the assumption that larger fractures have larger transmissivities is generally valid and this flow channeling is likely to occur under other reasonable correlation assumptions between transmissivity and fracture radius. The stabilization of the distribution mass into larger fractures, Fig. 1-11, and stabilization of the box-counting dimension of the particles to a value less than one, Fig. 1-12.b, occurs at roughly the same distance from the inlet where the mean travel time of particle clouds inserted using resident injection begins to scale linearly.

Under resident injection conditions, mass is inserted uniformly along the inlet plane, and as the plume moves through the DFN it is drawn into larger fractures, Fig. 1-10.a and Fig. 1-10.a. Retention of mass in these large fractures is observed after the cloud passes through this burn-in region. Flux-weighting inserts more mass into larger fractures and the mass remains there as the cloud moves through the domain. After this initial difference, the mass inserted under both conditions is primarily found in these larger fractures that act as principal pathways for flow and transport. Plots of the mean aperture of fractures on which mass resides shows that the initial discrepancy between the resident and flux-weighted injection rapidly decreases and the two curves nearly overlay one another after approximately two hundred and fifty meters (images not shown).

In addition to the migration of mass into large fractures, mass clusters within individual fractures. This is evidenced by the stabilization of the particle cloud box-dimension to a value less than one,  $\approx 0.80$ . This value indicates that the particles occupy a subspace of the fracture network at control planes which has dimension one. This in-fracture clustering is a result of the network topology and variability between fractures; there is no in-fracture aperture variability which would enhance in-fracture clustering (Tsang and Neretnieks, 1988, Tsang and Tsang, 1989, Berkowitz, 2002, Berkowitz and Braester, 1991).

Tortuosity retains information from all previous time steps, unlike mean aperture and box-dimension. Therefore it is more challenging to clearly see the evolution of the resident injected particles to the flux-weighted curves. However, the shape of the curve reporting the mean tortuosities rather than the actual values hint towards this convergence. Moreover, these results indicate that the difference in dispersion of the particle plumes inserted using the two different injection conditions also diminishes with time because tortuosity can be related to the coefficient of dispersion. After a slightly longer burn-in region than that observed for mean aperture and box-dimension, the shape of the two curves match closely, suggesting that the particles are moving through similar regions in the network. There might be a dependence of tortuosity on fracture set orientation. However, a systematic study with a thoughtfully designed synthetic fracture set would be more appropriate to characterize this dependence rather than the adopted fracture set. Nonetheless, changes in the fracture set orientation will not change the presented results that the initial difference between the two computed values of tortuosity decreases with time because of channeling.

Significantly, the exponent in the power-law tail of mass breakthrough was found to be greater than 2 for both flux-weighted and resident injection, which suggests that with sufficiently long travel distances the central limit theorem will ensure that the travel time distribution approaches a normal distribution. In such a situation, transport may be described with conventional analytical techniques such as the advection dispersion equation, (e.g., Painter et al. 2002). This is in contrast to the results of numerical experiments on smaller two-dimensional networks, (Berkowitz and Scher, 1997, 1998) and using smaller three-

dimensional networks with more approximate numerical approaches (Painter et al. 2002), which found evidence for anomalous (non-Fickian) transport using resident injection assumptions.

With larger fully three-dimensional networks and better numerical control for the particle tracking, and after accounting for a burn-in period in the resident-injection cases, we found evidence that the advection-dispersion equation might be an appropriate theoretical model for asymptotic behavior of transport in fractured media. The key factor for the asymptotic behavior of the plumes to be Fickian is that the velocity field must be fully sampled. One of the principal observations in this paper is that flow channeling occurs in these sparsely fractured networks. As noted above, this study suggests that particles spend the majority of their travel time in large fractures, which act as conduits through the domain rather than dispersing and sampling the entire network/velocity field. However, we only considered one fracture site characterization, which although generic, is insufficient to characterize how the geometry and connectivity of a DFN influence the time/domain size required for full sampling of a velocity field in a fracture dominated system. Moreover, the Forsmark site is extremely sparsely fractured, even in the context of sparsely fractured rock, and this might influence the ability of particles to sample the entire velocity field. Therefore, a separate study with a synthetic DFN where the geometry and connectivity of the network are designed to isolate and quantify this influence would be a more appropriate framework to determine how fracture connectivity influences the particles ability to sample the entire velocity field.

The application of theoretical models to represent the transport simulations reported here will be the focus of future investigations.

With regard to the sensitivity of the measured particle attributes to different lower cutoffs in the truncated power-law distribution used to generate the DFN, the following observations can be made. In the case of flux-weighted injection, no significant dependence is observed for any of the particle based attributes on the lower bound. This is likely the result of mass being inserted and then transported through the larger fractures in the network, which are not influenced by the lower cutoff used in the generation. However, a dependence is observed in the case of resident based injection. In general, particles moving through DFNs generated with lower values of the cutoff require longer distances before their mean travel time scales linearly. This dependence is possibly the result of more small fractures with low flux receiving the same percentage of mass as larger fractures under resident injection conditions. Therefore it takes longer for all the mass inserted in these small fractures to reach the large high transmissivity fractures than in networks generated with higher cutoff values. How this cutoff influences the distance required to reach an asymptotic state when resident injection conditions are employed requires further investigation.

### 1.3.6 Conclusions

We investigated the influence of injection mode on transport properties by coupling the DFN technique with a Lagrangian approach to model transport through stochastically generated representations of kilometer-scale fractured media. To simulate transport, passive advective particles were tracked through thirty independent DFN realizations generated according to site characterization data obtained from an extensive field investigation of the Forsmark site in Sweden. Spatial and temporal particle attributes were recorded at uniformly spaced control planes throughout the domain to observe the evolution of transport properties.

We observe that the mean value of travel time computed using particles inserted using flux-weighting scale linearly with distance traveled, and the tails of their cumulative distributions of travel time exhibit power-law scaling. In contrast, the mean travel time of particles inserted using resident injection initially scales non-linearly with distance and power-law scaling of the tail of the empirical cumulative distribution of travel times is not observed. However, after accounting for a pre-asymptotic region, the mean travel time of particles inserted using resident injection conditions also scales linearly, and the tails of their breakthrough curves exhibit power-law scaling with nearly the same exponent as that observed for particles inserted using flux-weighting. The physical mechanism behind this evolution appears to be

the draw of mass into larger fractures, both network scale channeling and in-fracture channeling are observed.

## 1.4 Effect of Internal Aperture Variability on Particle Tracking in DFN

### 1.4.1 Introduction

Aperture variability within individual fractures is usually neglected in fractured media modeling. In such case, individual fractures are assumed to be homogeneous. However, in reality, individual fractures are heterogeneous and have an effect on flow and transport properties. For example, the strong influence of fracture aperture variations on dispersion of contaminants was found by Keller et al. (Keller et al. 1999). In this study strong dependent of dissolved contaminants in fractured rocks from fracture aperture variability was established using 2D continuum model. It was shown that large fracture aperture regions result in significant channeling of the fluid flow, accelerating the movement of solute in particular direction (Keller et al. 1999). Dreuzy et al addressed effect of internal heterogeneity on flow properties in fractured media modeling using discrete fracture networks. Authors have shown that the distribution of local apertures effects on global fracture transmissivity field (Dreuzy et al. 2012). However, the importance of in-fracture variability in large-scale 3D discrete fracture network modeling on flow and solute transport is still poorly studied due to high computational cost.

The relative importance of in-fracture variability on solute transport is a long-standing scientific issue. Previous studies (e.g., Cvetkovic et al. 1999) of the transport effects of flow channeling in variable-aperture fractures typically considered a single fracture isolated from the rest of the network. Although these studies yield some clear insights into the process, the unrealistic boundary conditions for flow limit the usefulness of the results for field-scale applications. Flow in an individual fracture is controlled not only by the aperture variability, but also by the boundary conditions that are determined by connections with other fractures in the network. Fluid may enter and leave a fracture only where the fracture intersects other fractures. Those connections may represent a relatively small fraction of the fracture surface. This limited connection to other fractures introduces a certain degree of flow channeling independent of that caused by aperture variability. The relative importance of the two channeling mechanisms – heterogeneity-induced or geometry-induced – cannot be investigated without considering heterogeneous fractures embedded in a three-dimensional network. Previous attempts to address that issue (Painter, 2006) were limited by lack of reliable numerical tools. The new DFN simulation capability, DFNWORKS, has been extended to incorporate both fracture-to-fracture and within-fracture variability, thus allowing the importance of single-fracture aperture variability to be reliably assessed at the field scale.

In order to investigate the importance of in-fracture variability on solute transport simulation in large-scale DFN we compute Lagrangian parameters  $\tau$  and  $\beta$ . The role of the flow-dependent Lagrangian parameters  $\tau$  and  $\beta$  in controlling transport and retention in heterogeneous fractures and fracture networks was established in previous studies (Cvetkovic and Frampton, 2012). The non-reacting travel time  $\tau$  [T] and cumulative reactivity parameter  $\beta$  [T/L] (also referred to as transport resistance and denoted F) are cumulative parameters obtained by integrating along random streamlines. Once the probability distributions for these parameters are known, probabilistic simulation of transport can be performed with relatively little effort (Painter, 2006).

Detailed analyses (Cvetkovic et al. 2004) of comprehensive discrete fracture network simulations using the FracMan platform (Outters, 2003) clearly demonstrate that the distributions of  $\tau$  and  $\beta$  are highly non-Gaussian at the scales of interest, which is inconsistent with the results of continuum models and suggests that DFN simulation is a more reliable method for assessing transport in sparsely fractured rock. DFN-based simulation must adequately represent the transport processes at small scales. When aperture

variability within individual fractures is neglected in DFN simulations, individual fractures are assumed to be homogeneous. The cumulative reactivity parameter  $\beta$  is then computed as a ratio of the “flow-wetted surface” and flow rate of an individual fracture. When individual fractures are heterogeneous, it may cause flow to be “channelized” in individual fractures. However, the importance of internal variability relative to other sources of variability in the flow system is not obvious. On the one hand, internal variability in aperture tends to be smaller than fracture-to-fracture variability, which would suggest that internal aperture variability is less important. On the other hand, flow channeling in heterogeneous fractures tends to cause flow lines to coalesce in high-velocity regions, which may introduce a systematic bias toward lower  $\beta$  and less retention (Painter, 2006).

The current study addresses the importance of internal fracture aperture variability in determining field-scale transport in large-scale discrete fracture network. Recently developed DFNWORKS software is used to generate large-scale DFN, to apply internal heterogeneity on every fracture, where each computational cell is given its own value of aperture and transmissivity, to simulate a particle tracking through DFN, and, as a result, to analyze statistics of Lagrangian parameters calculated for millions of particles.

### 1.4.2 State of the Art

The DFN modeling and transport simulation are the primary tools in the study of in-fracture variability effect. DFNWORKS software, described in Chapter “DFNWORKS”, is used to model large scale DFN with following simulation of steady state flow and particle tracking. Once the DFN is generated, the in-fracture variability is applied to every single fracture of DFN. This procedure is described in Section “Representation of internal variability in DFN”, which also includes simple example of transport simulation of one fracture problem, showing the transport “channeling” in high variances. Section “Transport Lagrangian variables:  $\beta$  and  $\tau$ ” is focused on the Lagrangian variables  $\beta$  and  $\tau$  that are used to analyze the transport results in large scale discrete fracture networks.

#### 1.4.2.1 Representation of Internal Variability in DFN

Once the DFN is generated and the computational mesh is produced, the value of aperture and transmissivity of each individual fracture can be calculated independently of each other. Fracture transmissivity is calculated as a function of fracture aperture using the cubic law (Adler et al. 2012), while aperture is semi-correlated to fracture size and estimated as  $b=F \times R^k$ , where  $R$  is a fracture radius and  $0.5 < k < 2.0$  (Adler et al. 2012). This aperture value is used in our previous studies, when aperture and transmissivity remained constant along the fracture. In the case of in-fracture variability we use this value as a mean value for Gaussian distribution, which is applied to all fracture cells. GSTAT software is used to scatter aperture values to each computational cell along every fracture (Pebesma and Wesseling, 1998; Pebesma, 2004). It was found that the aperture distribution in the open part of the fracture in natural granite is well approximated by log-normal distribution. In the current study the aperture was modeled as having a log-normal distribution. The log-normal model for aperture is widely used in studies of transport in fractured rock. If aperture and transmissivity are related through cubic law, a log-normal distribution of aperture implies a log-normal distribution of transmissivity, albeit with different distribution parameters.

Applied spatial correlation length,  $\lambda$ , is a function of fracture size:  $\lambda=c \times R$ . We consider following values of coefficient  $c$ :  $c=0.1, 0.3, 0.5$ , and  $0.7$ . Fig. 1-17 shows the example of one circular fracture with distributed aperture values according to different spatial correlation lengths.

Another parameter that is being varied is a variance. Since fracture transmissivity is calculated from aperture using cubic law, we refer to variance in transmissivity:  $\text{Var}_2(\sigma)$ ,  $\text{Var}_4(\sigma)$ , and  $\text{Var}_6(\sigma)$  correspond to 2, 4, and 6 orders of magnitude difference in DFN transmissivity, respectively.

Once aperture and transmissivity are defined for each computational cell on each fracture, the flow solution is obtained using DFNFLOW and transport is simulated using DFNTRANS.

### 1.4.2.1.1 Transport Simulation on Single Fracture Problem

Before we proceed to large scale DFN modeling we have tested our workflow on a single fracture problem. Effect of internal heterogeneity on transport on single fracture model is well studied (e.g., Moreno and Tsang, 1994). It's been shown that flow “channeling” takes place as a variance in permeability increases. Fig. 1-18 shows results of particle tracking through a single fracture. The pressure boundary conditions are applied on bottom (high pressure) and top (low pressure) boundaries of the fracture. Aperture is distributed according to spatial correlation length  $\lambda=0.1R$ , where  $R$  is an average of lengths of rectangular sides. Three cases are shown for different variance of transmissivity (from left to right):  $\text{Var}_1(\sigma)$ ,  $\text{Var}_2(\sigma)$ , and  $\text{Var}_4(\sigma)$ , which correspond to 1, 2, and 4 order of magnitude difference in transmissivity value, respectively, shown on color patterns on the figure.

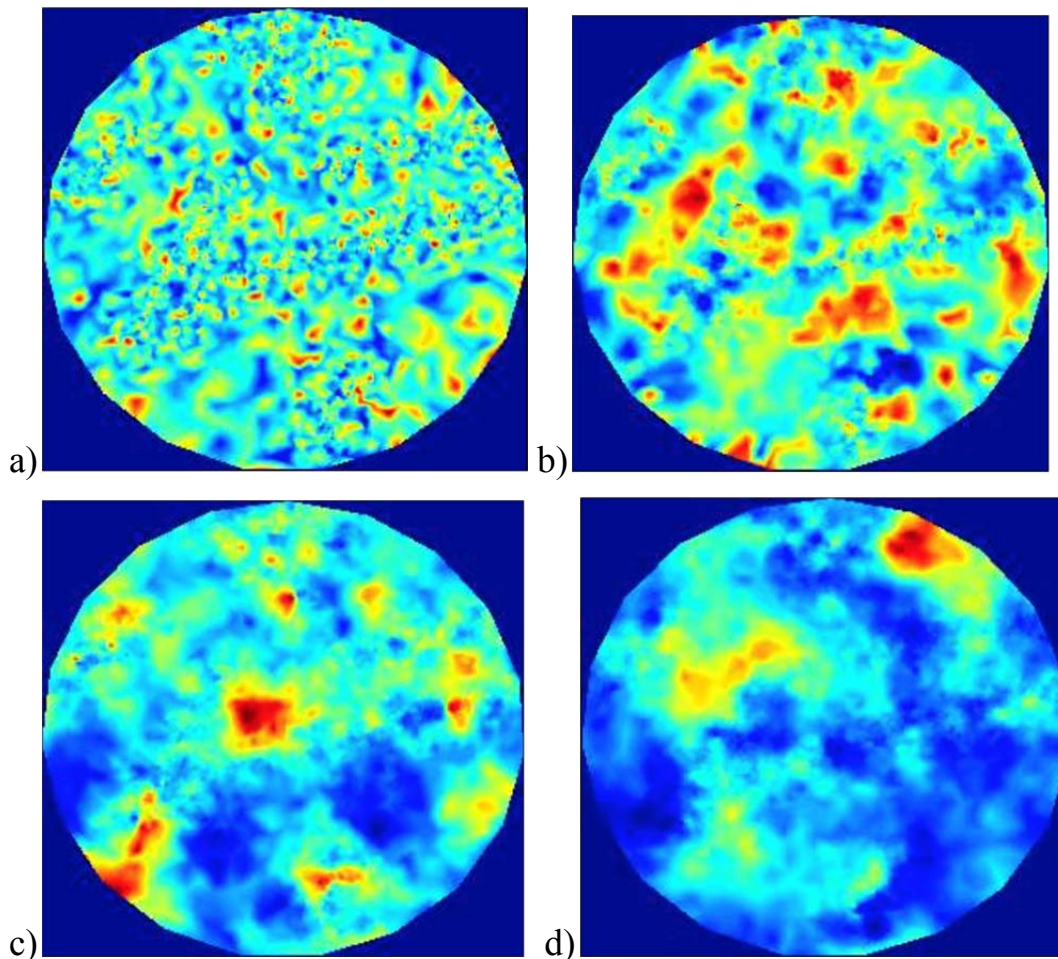


Figure 1-17. An example of one circular fracture with in-fracture variability. There are different spatial correlation lengths are applied: a)  $\lambda=0.1R$ , b)  $\lambda=0.3R$ , c)  $\lambda=0.5R$ , d)  $\lambda=0.7R$ . As correlation length increases, the zones of high and low aperture are observed clearer.

Initially particles are placed equidistant at bottom boundary of the fracture. Proceeding to the top out-flow boundary, the trajectories are pretty straight and tortuosity of paths is minimal in case of low variance. As variance of transmissivity is getting higher we can observe flow “channeling”. Particles tend to move around zones with low transmissivity and keep motion towards higher transmissivity regions.

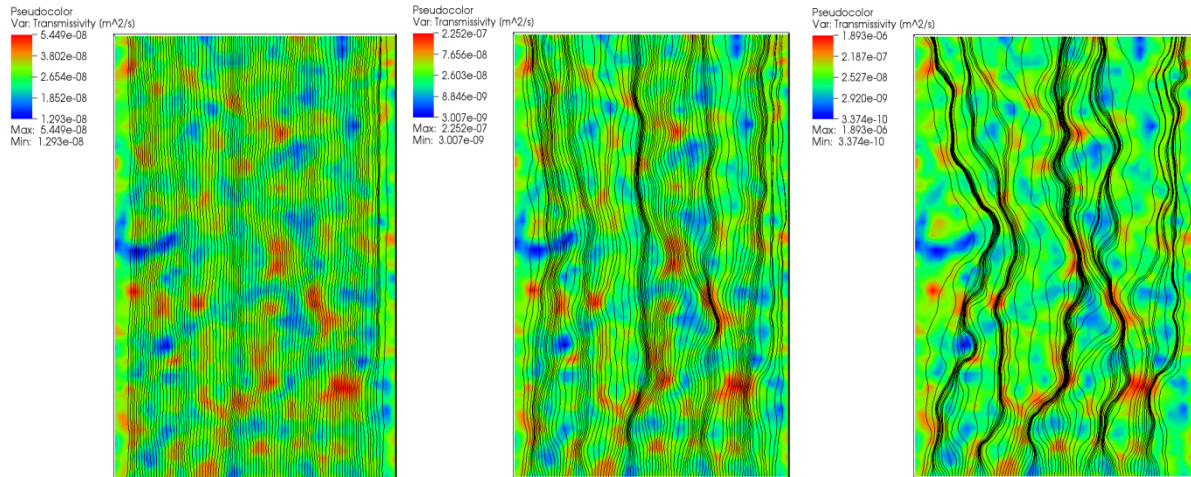


Figure 1-18. Single fracture configuration with three cases of particle trajectories are shown for different applied variances of transmissivity (from left to right):  $\text{Var}_1(\sigma)$ ,  $\text{Var}_2(\sigma)$ , and  $\text{Var}_4(\sigma)$ , which correspond to 1, 2, and 4 orders of magnitude difference. Transmissivity distribution is shown by color patterns. Solid lines represent particles trajectories that are moving from bottom to top boundaries of the fracture. As variance in transmissivity increases the flow channeling is observed clearer, and the tortuosity of particles trajectories increases.

**1.4.2.1.2 DFN with In-fracture Variability in Scale of 1 km**

The discrete fracture networks, similar to those observed in natural repository cite Forsmark, Sweden, are generated to study the effect of in-fracture variability on a transport in large scale DFN. Details and input parameters for DFN generation are provided in Section “DFN Model: Forsmark, Sweden”. In this study we use the version of DFN with highest density, where low cut-off radius of circular fractures is 15m ( $r_0=15\text{m}$  in Eq.1-10, Table 1-1). Ten independent DFN realizations were generated. The pressure boundary conditions are applied to top and bottom side of the domain, assuming fluid flow in vertical direction, from bottom to top. Example of steady state pressure solution in one of DFN realizations is shown in Fig. 1-19.

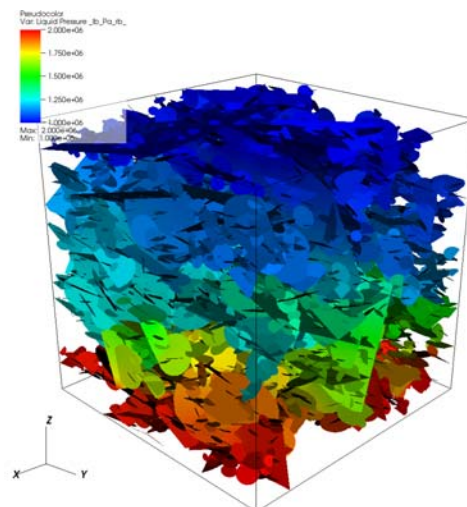


Figure 1-19. Example of steady state pressure solution in one of DFN realizations. The pressure boundary conditions are applied to top and bottom side of the domain, assuming fluid flow in vertical direction, from bottom to top. High pressure is shown by warm colors.

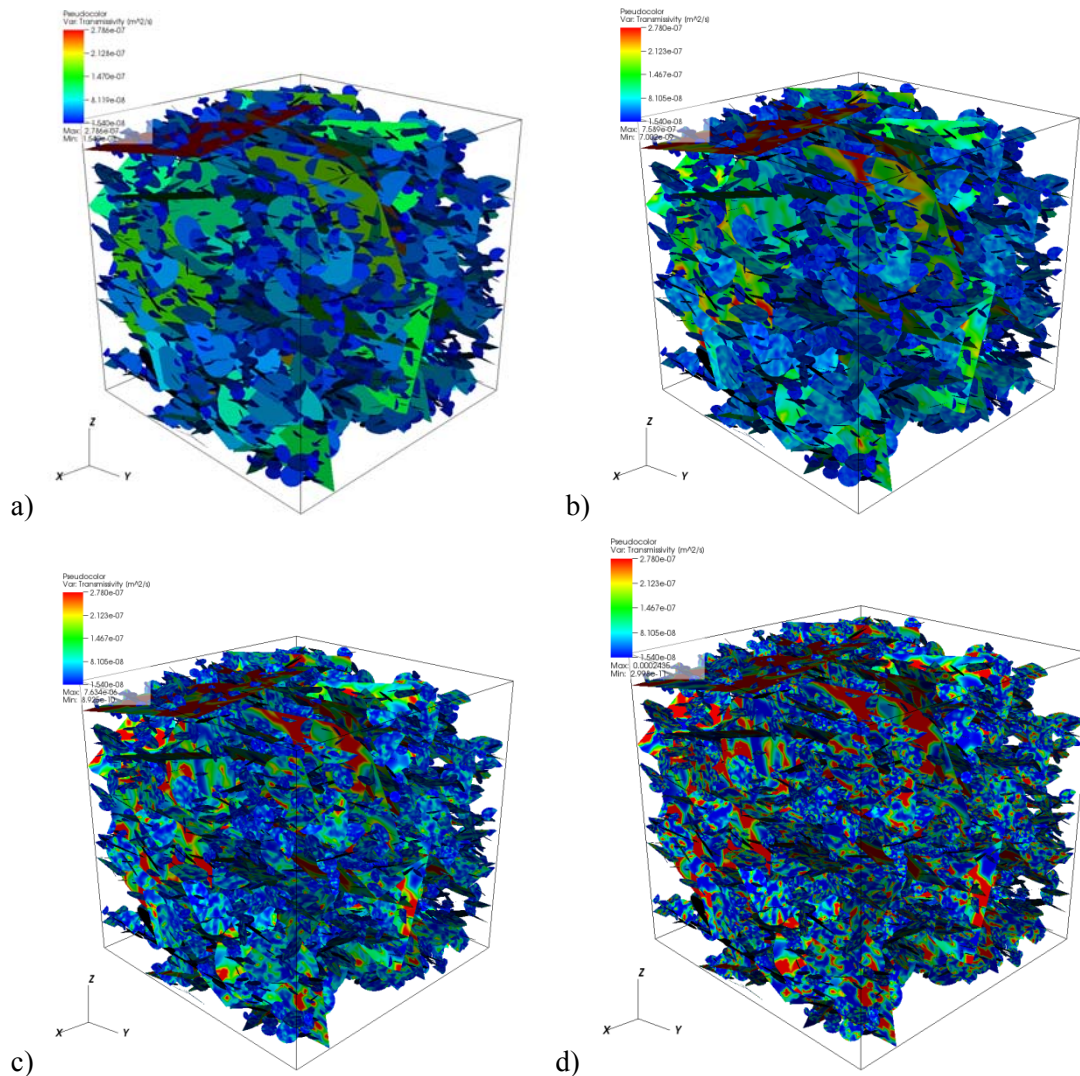


Figure 1-20. An example of DFN configuration with 4 cases of transmissivity distribution: a) transmissivity is constant along each fracture, but varies from fracture to fracture according to fracture size; b), c), d) show transmissivity distribution with  $\text{Var}_2(\sigma)$ ,  $\text{Var}_4(\sigma)$ , and  $\text{Var}_6(\sigma)$ , respectively.

Figure 1-20 shows the transmissivity distribution over entire DFN. The constant transmissivity along each fracture is shown in Fig. 1-20.a. The transport for this case is modeled for all 10 realizations and is used as a reference case. Fig. 1-20 b, c, d show transmissivity distribution with  $\text{Var}_2(\sigma)$ ,  $\text{Var}_4(\sigma)$ , and  $\text{Var}_6(\sigma)$ , respectively. The actual minimum and maximum of transmissivity values are show below the color legend, however colors are scaled according to the reference case (Fig.1-20.a). This way, the smooth transition of transmissivity from cell to cell can be observed in case of low variance (Fig. 1-20 b), and local sharp change of transmissivity is detected at high variance.

#### 1.4.2.2 Transport Lagrangian Variables: $\beta$ and $\tau$

We are interested in the time required for a particle to be transported by advection with the water flowing in open fractures. The residence time is a random variable and is controlled by two Lagrangian variables:  $\tau$ , the residence time for a particle moving with water from in-flow to out-flow boundary, and  $\beta$ , a



retention parameter related to the normalized surface area available for diffusional transfer to the rock matrix. These parameters are defined as integrals along the trajectory  $x'$

$$\tau = \int_0^x \frac{1}{v(x')} dx' \cong \sum_{i=1}^n \frac{l_i}{v_i} \quad (1-12)$$

$$\beta = \int_0^x \frac{1}{v(x')b(x')} dx' \cong \sum_{i=1}^n \frac{l_i}{b_i v_i}$$

where the particle trajectory is a path through fractures in fracture network, passing through a series of  $n$  cells with a constant velocity and aperture in each cell  $n_i$ . Here  $b_i$  is a half-aperture of the current cell,  $v_i$  is a particle velocity in the cell, and  $l_i$  is a length of the  $i$ -th cell in the pathway. The total travel distance is through fracture network from in-flow to out-flow boundary is  $x$  (Painter et al. 2002). The Lagrangian variables are defined along the trajectories of particles, therefore they have the flow dynamics built in. Given statistics of  $\tau$  and  $\beta$  and a model retention process, the distribution of residence time can be calculated.

Fig. 1-21 shows the cumulative and complementary cumulative distributions of calculated Lagrangian variables of advective transport in large scale DFN. Here  $\tau$  (top panel) and  $\beta$  (bottom panel) are calculated for reference case, when the fracture transmissivity remains constant along each fracture but varies from fracture to fracture in the network.

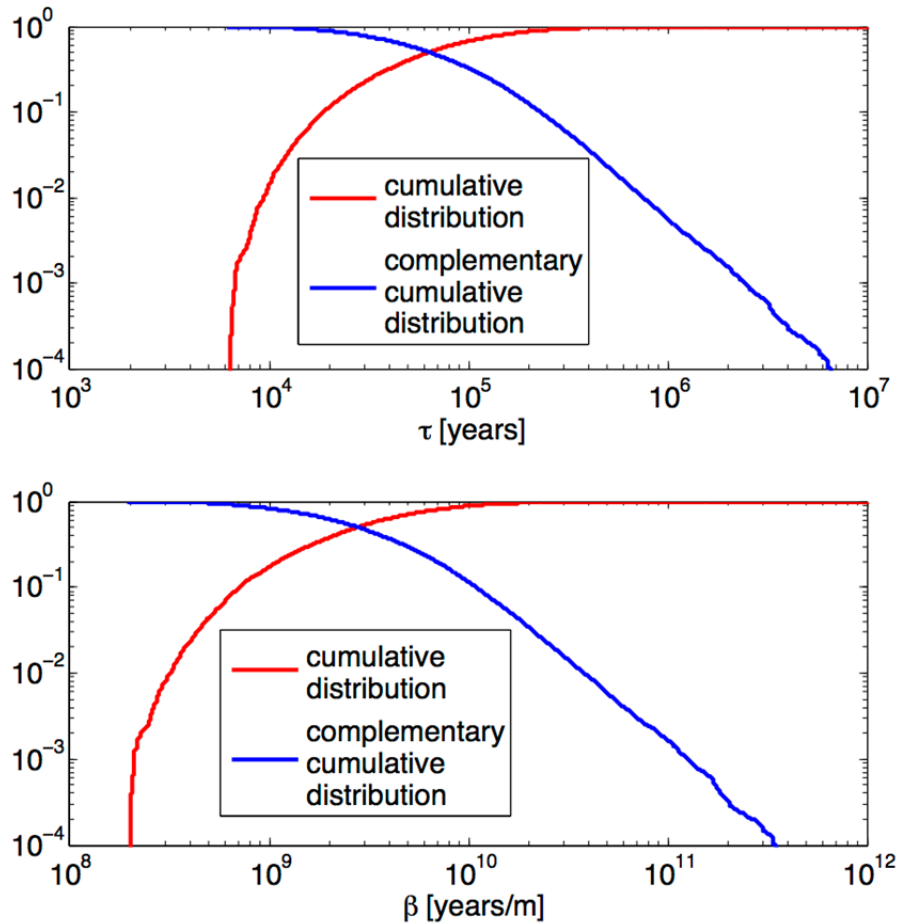


Figure 1-21. The cumulative and complementary cumulative distributions of calculated  $\tau$  (top panel) and  $\beta$  (bottom panel) are calculated for transport in reference case.

### 1.4.3 Results and Discussion

Lagrangian parameters  $\tau$  and  $\beta$  are computed during particles travel through fracture network. Initially particles are placed equidistant on in-flow boundary and followed to out-flow boundary accumulating  $\tau$  and  $\beta$  in each computational cell. Statistics of  $\tau$  and  $\beta$  are shown for  $10^6$  particles participated in 10 DFN independent realizations. The cumulative (CDF) and complementary cumulative (CCDF) distributions are plotted according to their flux weights, calculated by Eq.1-3.b, showing statistics of earlier time on cumulative distributions (fastest particles) and longest travel time on tail of complementary cumulative distributions.

Fig. 1-22 and Fig.1-23 show CDF and CCDF of  $\tau$  and  $\beta$ , respectively, comparing results of simulations with different correlation lengths,  $\lambda$  at the same transmissivity variance. The in-fracture variability has an insignificant effect on both,  $\tau$  and  $\beta$ , when the fracture transmissivity variance is little,  $\text{Var}_2(\sigma)$ . However, as variance increases, the tails of cumulative distributions of different spatial correlation lengths diverge from reference case (constant transmissivity along each fracture) of both,  $\tau$  and  $\beta$ . Thus, travel time of fastest particles is sensitive to transmissivity variation, and at longest spatial correlation length,  $\lambda=0.7R$ , the smallest travel time has been captured. Analyzing complementary cumulative distribution, no

difference between spatial correlation lengths is observed at probability higher than 0.001. There is a little diverging of distribution tails (Probability < 0.001) from the reference case, however no clear dependence on spatial correlation length is detected.

Fig. 1-24 and Fig. 1-25 show CDF and CCDF of  $\tau$  and  $\beta$ , respectively, comparing results of simulations with different variance of DFN transmissivity and plotted for the spatial same correlation length. As correlation lengths increases, the difference between reference case and largest transmissivity variance expands in cumulative distribution tails. Thus, the shortest travel time is sensitive to transmissivity variance at probability < 0.1, however there is no difference is observed at probability higher than 0.1 at any considered variance of transmissivity. The longest time measured for particles (tails of complementary cumulative distribution) shows almost no divergence with reference case.

Scott Painter looked at the sensitivity of transport on in-fracture variability in previous study (Painter, 2006) for small scale DFN, comparing  $\beta$  for two different correlation length. Analyzing CDF and CCDF for particles under residence injection, no sensitivity to in-fracture variability was noticed (Painter, 2006). In our large-scale DFN simulations with flux-weighted particles, we observe a little sensitivity on transmissivity variations at earlier travel time. Also, no significant effect of spatial correlation length,  $\lambda$ , was detected.

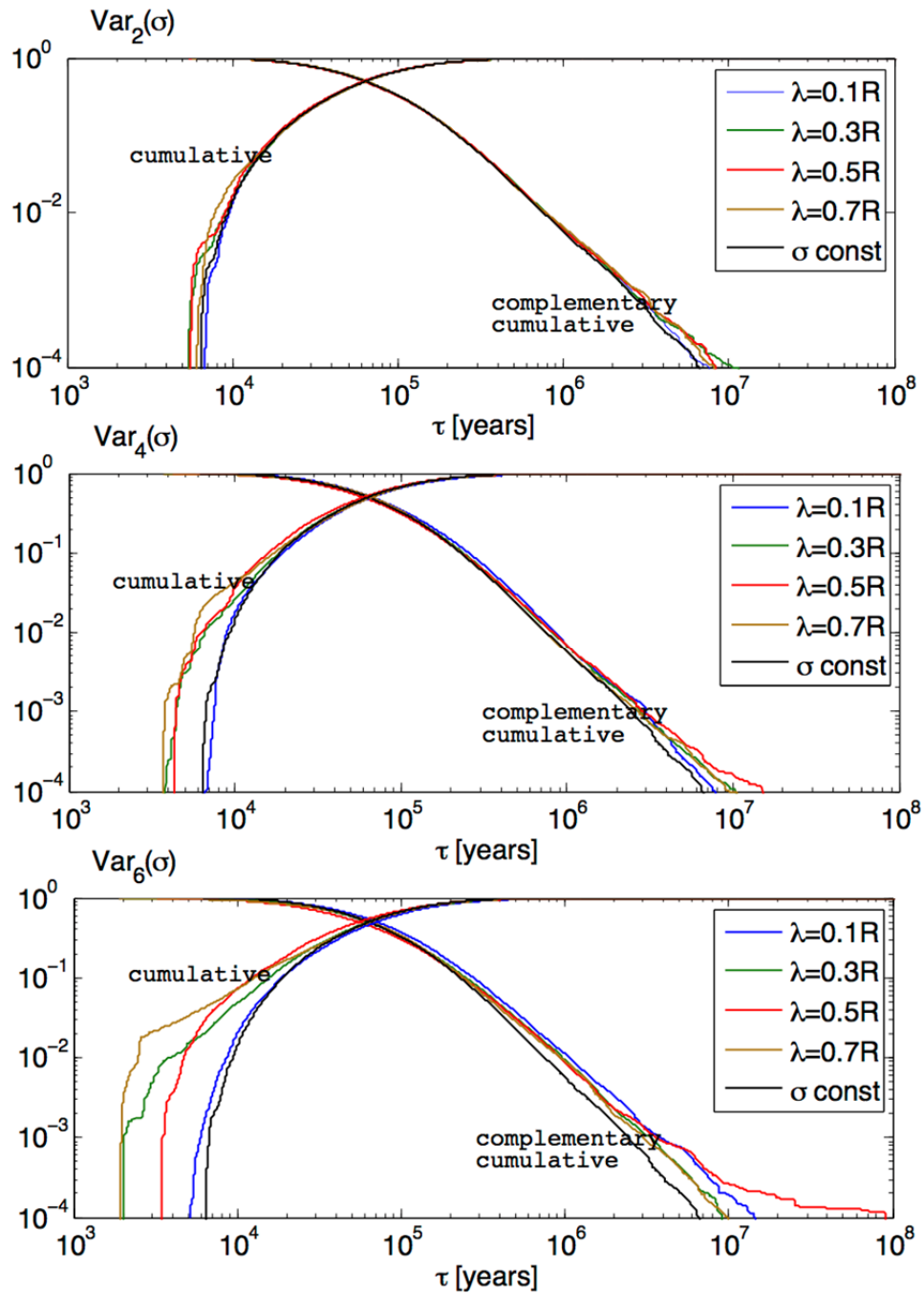


Figure 1-22. Cumulative and complementary cumulative distributions of  $\tau$  for different variations of DFN transmissivity. Different correlation lengths,  $\lambda$ , compared to the reference case, when no in-fracture variability is implied.

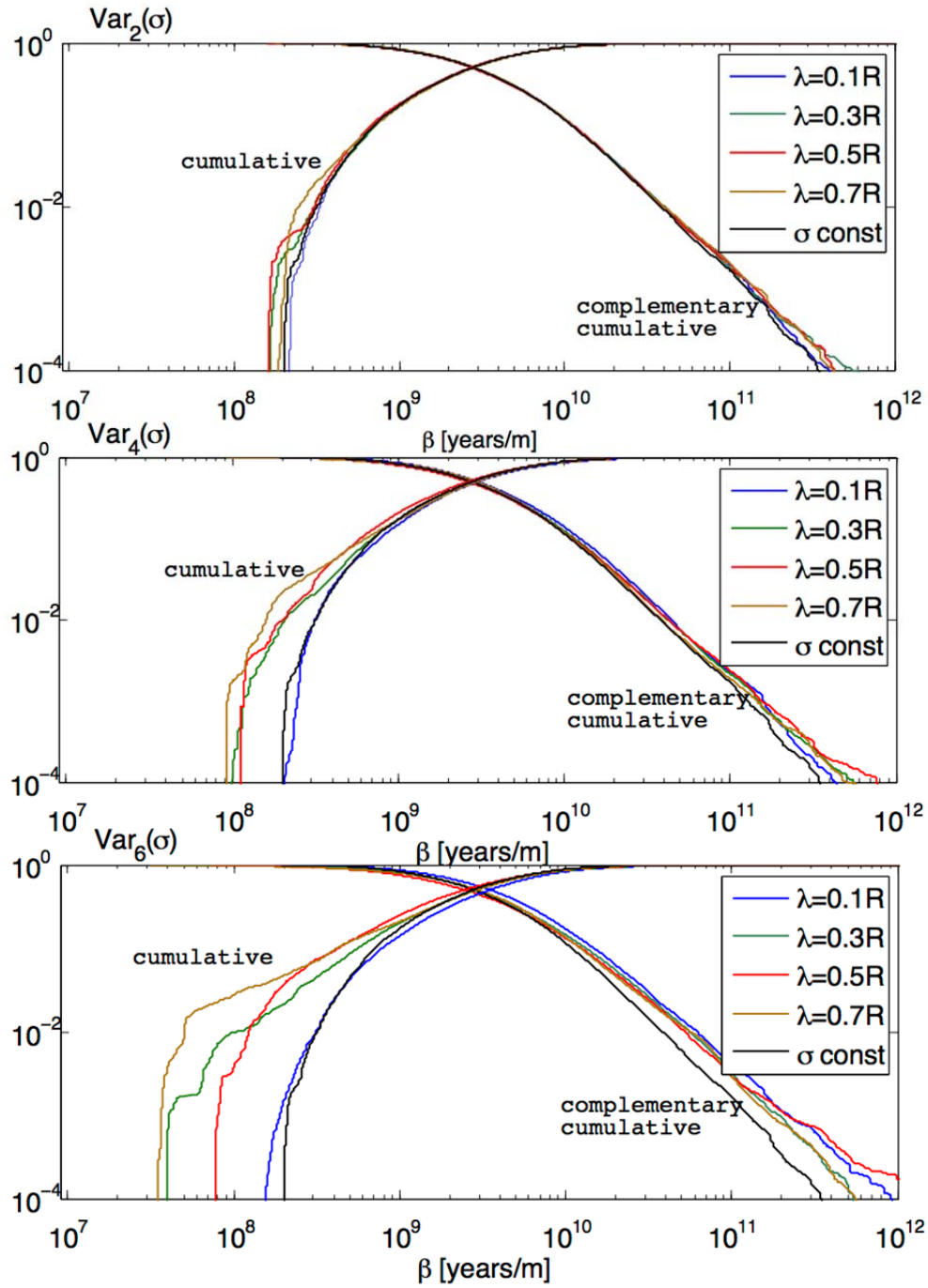


Figure 1-23. Cumulative and complementary cumulative distributions of  $\beta$  for different variations of DFN transmissivity. Different correlation lengths,  $\lambda$ , compared to the reference case, when no in-fracture variability is implied.

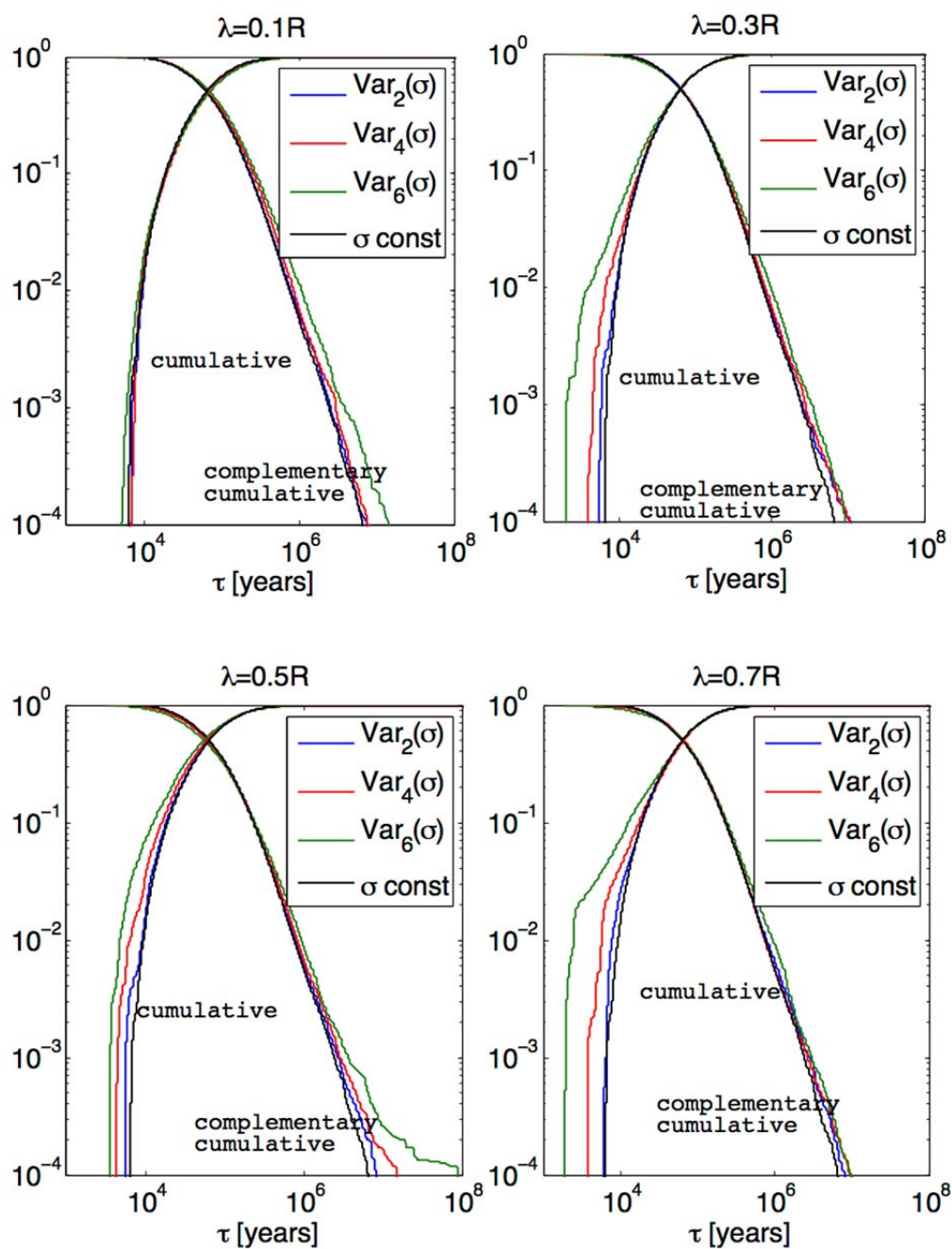


Figure 1-24. Cumulative and complementary cumulative distributions of  $\tau$  for each considered correlation lengths,  $\lambda$ . Different variations of DFN transmissivity are compared to the reference case, when no in-fracture variability is implied.

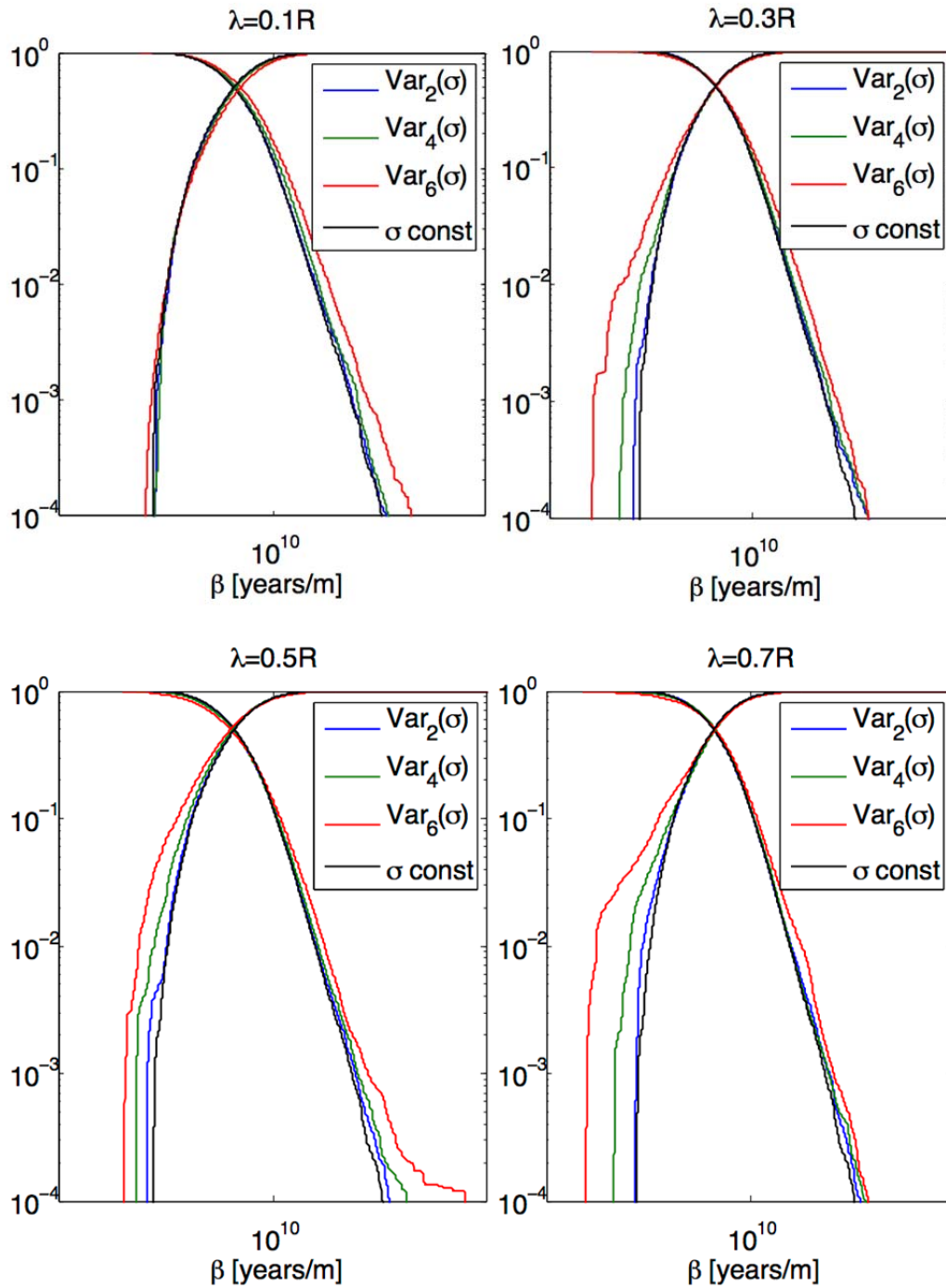


Figure 1-25. Cumulative and complementary cumulative distributions of  $\beta$  for each considered correlation lengths,  $\lambda$ . Different variations of DFN transmissivity are compared to the reference case, when no in-fracture variability is implied.

## 1.5 Concluding Remarks

We have provided a unified description of the dfnWorks suite that was developed over the past five years with significant contribution from the Used Fuel Campaign. The generation and meshing strategy are outlined, a description of the flow solver provided, and the pillars of the particle tracker presented. The ability to resolve flow and transport while retaining fracture geometry allowed for two unique studies of transport in large, kilometer-scale, DFN. The first study showed that after a pre-equilibrium region solutes injected under resident conditions evolve and behave similarly to that injected under flux-weighted conditions. The observation of this evolution was made feasible by the size of the DFN considered and characterizing the physical mechanisms that induced this phenomenon was made possible by retaining the geometry of the fractures rather than using a one-dimensional pipe-network approximation. Similarly, the second study was made possible because the fracture geometry was retained, so in-fracture variability could be incorporated. Other studies have used breakthrough times acquired from single fractures with internal aperture variability, but this study marks the first to resolve Lagrangian based transport in DFN where in-fracture variability is explicitly represented. We found that early breakthrough times and retention curves are influenced by in-fracture aperture variability but the tails of the breakthrough curves are insensitive to these variations.

Moving forward, we are utilizing the dfnWorks suite in a number of ways. First, a major question in DFN modeling is the relationship between fracture size and transmissivity. We are currently characterizing the impact of adopting different relationships between the two on transport by selecting three different models: i) deterministic correlation between fracture radius and transmissivity, ii) semi-deterministic correlation between fracture radius and transmissivity that includes a stochastic noise term, and iii) non-correlated where transmissivities are sampled from log normal distribution without regard for fracture size. This work is being done in collaboration with Andrew Frampton of the Stockholm University and Scott Painter of Oak Ridge National Laboratory. Second, we are moving beyond model development and towards model comparison in a co-operative venture with Sandia National Laboratory to compare our DFN model with their fractured continuum model (FCM). Preliminary results from a DFN/FCM comparison are presented in Sandia's Level 4 milestone. Using the same fracture site characterization, we are individually modeling transport using our unique models and comparing the results. We plan on using this collaboration to understand the transition between when continuum and DFN models are more appropriate when sites have varying degrees of fracture density. Finally, PFLOTRAN provides an efficient and scalable framework to capitalize on for upcoming performance assessment and uncertainty quantification studies that will be conducted under the Used Fuel Disposition Program. We are developing tools to run PFLOTRAN and then extract reduced order models that can be rapidly implemented in system-level and decision-making models.

In frame of SKB Task "Force on Modeling of Groundwater Flow and Transport of Solutes", Task 9A, LANL team can provide a significant contribution to a modeling of REPRO experiments WPDE-1&2 and TDE. Modeling the boreholes with diameter of 56 mm, leaving 1 mm gap between borehole walls and the filled inside dummy requires accurate computational mesh that can be produced by LaGriT (LaGriT, 2013). Modeling the water injection into the gap with a tracer pulse can be successfully driven by massively parallel flow solver, PFLOTRAN (Lichtner et al 2015), where the tracer diffusion into rock matrix can be accurately measured.

## 1.6 References

Adler P. M., Thovert J. F. and Mourzenko V. V. (2012) *Fractured porous media*. Oxford University Press.



- Andersson P., Byegård J., Billaux D., Cvetkovic V., Dershowitz W., Doe T., Hermanson J., Poteri A., Tullborg E. L., and Winberg A. (2007) *TRUE block scale continuation project. final report.*, Technical report, Swedish Nuclear Fuel and Waste Management Co., Stockholm, Sweden.
- Balay S., Abhyankar S., Adams M., Brown J., Brune P., Buschelman K., Eijkhout V., Gropp W., Kaushik D., Knepley M., et al. (2014) *PETSc users manual*, revision 3.5.
- Bear J. (1988) *Dynamics of fluids in porous media*, Dover publications.
- Benedetto M. F., Berrone S., Pieraccini S., and Scialo` S. (2014) The virtual element method for discrete fracture network simulations, *Computer Methods in Applied Mechanics and Engineering*, 280, 135–156.
- Berkowitz B. (2002) Characterizing flow and transport in fractured geological media: A review, *Adv. Water Resour.*, 25(8-12), 861–884.
- Berkowitz B. and Braester C. (1991) Solute transport in fracture channel and parallel plate models, *Geophys. Res. Lett.*, 18(2), 227–230.
- Berkowitz B. and Scher H. (1997) Anomalous transport in random fracture networks, *Phys. Rev. Lett.*, 79(20), 4038.
- Berkowitz B. and Scher H. (1998) Theory of anomalous chemical transport in random fracture networks, *Phys. Rev. E*, 57, 5858–5869.
- Berrone S., Pieraccini S., and Scialo` S. (2013) A PDE-constrained optimization formulation for discrete fracture network flows, *SIAM Journal of Scientific Computing*, 35(2), B487–B510.
- Cacas M. C., Ledoux E., De Marsily G., Tillie B., Barbreau A., Durand E., Feuga B., and Peaudecerf P. (1990) Modeling fracture flow with a stochastic discrete fracture network: Calibration and validation: 1. the flow model, *Water Resources Research*, 26(3), 479–489.
- Coxeter H. S. M. (1969) *Introduction to geometry*, Vol. 6, Wiley New York.
- Cvetkovic V. (2011) The tempered one-sided stable density: a universal model for hydrological transport? *Environ. Res. Lett.*, 6(3), 034008.
- Cvetkovic V. (2013) How accurate is predictive modeling of groundwater transport? A case study of advection, macrodispersion, and diffusive mass transfer at the Forsmark site (sweden), *Water Resour. Res.*, 49(9), 5317–5327.
- Cvetkovic V. and Frampton A. (2012) Solute transport and retention in three-dimensional fracture networks, *Water resources research*, 48(2).
- Cvetkovic V., Selroos J. O. and Cheng H. (1999) Transport of reactive tracers in rock fractures, *Journal of Fluid Mechanics*, 378, 335-356.
- Cvetkovic V., Painter S., Outters N. and Selroos J. O. (2004). Stochastic simulation of radionuclide migration in discretely fractured rock near the Äspö Hard Rock Laboratory, *Water resources research*, 40(2).
- De Dreuzy J.-R., Darcel C., Davy P., and Bour O. (2004) Influence of spatial correlation of fracture centers on the permeability of two-dimensional fracture networks following a power law length distribution, *Water Resources Research*, 40(1).
- Demmy G., Berglund S., and Graham W. (1999) Injection mode implications for solute transport in porous media: Analysis in a stochastic Lagrangian framework, *Water Resour. Res.*, 35(7), 1965–1973.

- Dershowitz W. (2014) *Interactive discrete feature data analysis, geometric modeling, and exploration simulation: User documentation*, version 7.4, FracMan, <http://fracman.golder.com/>.
- Dershowitz W. and Fidelibus C. (1999) Derivation of equivalent pipe network analogues for three-dimensional discrete fracture networks by the boundary element method, *Water Resources Research*, 35(9), 2685–2691.
- Dreuzy J.-R., Meheust Y., and Pichot v. (2012) Influence of fracture scale heterogeneity on the flow properties of three-dimensional discrete fracture networks, *Journal of Geophysical Research - Solid Earth*, 117(B11).
- Elsworth D. (1986) A hybrid boundary element-finite element analysis procedure for fluid flow simulation in fractured rock masses, *International Journal for Numerical and Analytical Methods in Geomechanics*, 10(6), 569–584.
- Endo H., Long J., Wilson C., and Witherspoon P. (1984) A model for investigating mechanical transport in fracture networks, *Water Resour. Res.*, 20(10), 1390–1400.
- Erhel J., De Dreuzy J.-R., and Poirriez B. (2009) Flow simulation in three-dimensional discrete fracture networks, *SIAM Journal of Scientific Computing*, 31(4), 2688–2705.
- Falconer K. (2013) *Fractal Geometry: Mathematical Foundations and Applications*. John Wiley & Sons, 2013.
- Faybishenko B. (2005) *Dynamics of fluids and transport in fractured rock*, Number 162, American Geophysical Union.
- Frampton A. and Cvetkovic V. (2007) Upscaling particle transport in discrete fracture networks: 1. Nonreactive tracers, *Water Resour. Res.*, 43(10).
- Frampton A. and Cvetkovic V. (2007) Upscaling particle transport in discrete fracture networks: 2. Reactive tracers, *Water Resour. Res.*, 43(10).
- Frampton A. and Cvetkovic V. (2009) Significance of injection modes and heterogeneity on spatial and temporal dispersion of advecting particles in two-dimensional discrete fracture networks, *Adv. Water Resour.*, 32(5), 649–658.
- Frampton A. and Cvetkovic V. (2011) Numerical and analytical modeling of advective travel times in realistic three-dimensional fracture networks, *Water Resour. Res.*, 47(2).
- Geier J. (2011) *Investigation of discrete-fracture network conceptual model uncertainty at Forsmark*, Tech. rep., Swedish Radiation Safety Authority, Stockholm, Sweden.
- Gotovac H., Cvetkovic V., and Andricevic R. (2009) Flow and travel time statistics in highly heterogeneous porous media, *Water Resour. Res.*, 45(7).
- Gotovac H., Cvetkovic V., and Andricevic R. (2010) Significance of higher moments for complete characterization of the travel time probability density function in heterogeneous porous media using the maximum entropy principle, *Water Resour. Res.*, 46(5).
- Hammond G. E. and Lichtner P. C. (2010) Field-scale model for the natural attenuation of uranium at the Hanford 300 area using high-performance computing, *Water Resources Research*, 46(9), 2010.
- Hammond G. E., Lichtner P. C., and Mills R. T. (2014) Evaluating the performance of parallel subsurface simulators: An illustrative example with PFLOTRAN, *Water Resources Research*, 50(1), 208–228.
- Hammond G. E., Lichtner P. C., Lu C., and Mills R. T. (2012) PFLOTRAN: reactive flow & transport code for use on laptops to leadership-class supercomputers, *Groundwater Reactive Transport Models*, pages 142–160.

- Hartley L. and Joyce S. (2013) Approaches and algorithms for groundwater flow modeling in support of site investigations and safety assessment of the Forsmark site, Sweden, *Journal of Hydrology*, 500, 200–216.
- Hartley L., Cox I., Holton D., Hunter F., Joyce S., Gylling B., Lindgren M. (2004) *Groundwater flow and radionuclide transport modelling using CONNECTFLOW in support of the SR can assessment*, Tech. Rep. SKB Rapport R-04-61, Swedish Nuclear Fuel and Waste Management Co., Stockholm, Sweden.
- Hyman J. D., Gable C. W., Painter S. L., and Makedonska N. (2014) Conforming Delaunay triangulation of stochastically generated three dimensional discrete fracture networks: A feature rejection algorithm for meshing strategy, *SIAM Journal of Scientific Computing*, 36(4), A1871–A1894.
- Jankovic' I. and Fiori A. (2010) Analysis of the impact of injection mode in transport through strongly heterogeneous aquifers, *Adv. Water Resour.*, 33(10), 1199–1205.
- Joyce S., Hartley L., Applegate D., Hoek J., and Jackson P. (2014) Multi-scale groundwater flow modeling during temperate climate conditions for the safety assessment of the proposed high-level nuclear waste repository site at forsmark, Sweden, *Hydrogeology Journal*, 22(6), 1233–1249.
- Karra S. and Kitay C. (2015) *PyFLOTTRAN documentation release 1.0.0*, Technical Report LA-UR-15-21189, Los Alamos National Laboratory.
- Karra S., Painter S. L., and Lichtner P. C. (2014) Three-phase numerical model for subsurface hydrology in permafrost-affected regions (PFLOTTRAN-ICE v1. 0), *The Cryosphere*, 8(5), 1935–1950.
- Karra S., Bisht G., Lichtner P. C., and Hammond G. E. (2013) Coupling geomechanics with flow and reactive transport in PFLOTTRAN for subsurface applications, *AGU Fall Meeting Abstracts*, 1, 1106.
- Karra S., Makedonska N., Viswanathan H., Painter S. L., and Hyman J. D. (2015) Effect of advective flow in fractures and matrix diffusion on natural gas production, *Water Resources Research*, (under review).
- Keller A. A., Roberts P. V. and Blunt M. J. (1999) Effect of fracture aperture variations on the dispersion of contaminants, *Water Resources Research*, 35(1), 55-63.
- Kreft A. and Zuber A. (1978) On the physical meaning of the dispersion equation and its solutions for different initial and boundary conditions, *Chem. Eng. Sci.*, 33(11), 1471–1480.
- LaGriT (2013) *Los Alamos Grid Toolbox, (LaGriT)*, <http://lagrit.lanl.gov>, Los Alamos National Laboratory.
- Lichtner P. C. and Karra S. (2014) Modeling multiscale-multiphase-multicomponent reactive flows in porous media: Application to co2 sequestration and enhanced geothermal energy using PFLOTTRAN. In *Al-Khoury R. and Bundschuh J. (eds.) Computational Models for CO<sub>2</sub> Geo-sequestration & Compressed Air Energy Storage* (<http://www.crcnetbase.com/doi/pdfplus/10>), pages 81–136, CRC Press.
- Lichtner P. C., Hammond G. E., Lu C., Karra S., Bisht G., Andre B., Mills R. T., and Kumar J. (2015) *PFLOTTRAN user manual: A massively parallel reactive flow and transport model for describing surface and subsurface processes*, Technical report, Los Alamos National Laboratory.
- Long J., Remer J., Wilson C., and Witherspoon P. (1982) Porous media equivalents for networks of discontinuous fractures, *Water Resour. Res.*, 18(3), 645–658.

- Lu C. and Lichtner P. C. (2007) High resolution numerical investigation on the effect of convective instability on long term CO<sub>2</sub> storage in saline aquifers, *Journal of Physics: Conference Series*, 78, 012042, IOP Publishing.
- Makedonska N., Painter S. L., Bui Q. M., Gable C. W., and Karra S. (2015) Particle tracking approach for transport in three-dimensional discrete fracture networks, *Computation Geosciences*, (under review).
- Marys'ka J., Severy'n O., and Vohral'ik M. (2005) Numerical simulation of fracture flow with a mixed-hybrid fem stochastic discrete fracture network model, *Computational Geosciences*, 8(3), 217–234.
- Middleton R. S., Carey J. W., Currier R. P., Hyman J. D., Kang Q., Karra S., Jime'nez-Mart'inez J., Porter M. L., and Viswanathan H. S. (2015) Shale gas and non- aqueous fracturing fluids: Opportunities and challenges for supercritical CO<sub>2</sub>, *Applied Energy*, 147, 500–509.
- Mills R. T., Lu C., Lichtner P. C., and Hammond G. E. (2007) Simulating subsurface flow and transport on ultrascale computers using PFLOTRAN, *Journal of Physics: Conference Series*, 78, 012051, IOP Publishing.
- Mills R. T., Bisht G., Karra S., Hoffman F. M., Hammond G. E., Kumar J., Painter S. L., Thornton P. E., and Lichtner P. C. (2012) Progress towards coupled simulation of surface/subsurface hydrologic processes and terrestrial ecosystem dynamics using the community models PFLOTRAN and CLM, In *AGU Fall Meeting Abstracts*, 1, 1426.
- Moreno L. and Tsang C. F. (1994) Flow channeling in strongly heterogeneous porous media: A numerical study, *Water Resources Research*, 30(5), 1421-1430.
- Mount D. M. and Gable C. W. (2001) A point-placement strategy for conforming Delaunay tetrahedraliza- tion, *International Journal of Computational Geometry & Applications*, 11(6), 669–682.
- Mustapha H. and Dimitrakopoulos R. (2011) Discretizing two-dimensional complex fractured fields for incompressible two-phase flow, *International Journal for Numerical Methods in Fluids*, 65(7), 764– 780.
- Mustapha H. and Mustapha K. (2007) A new approach to simulating flow in discrete fracture networks with an optimized mesh, *SIAM Journal of Scientific Computing*, 29, 1439.
- Mustapha H., Dimitrakopoulos R., Graf T., and Firoozabadi A. (2011) An efficient method for discretizing 3D fractured media for subsurface flow and transport simulations, *International Journal for Numerical Methods in Fluids*, 67(5), 651–670.
- National Research Council (1996) *Rock fractures and fluid flow: contemporary understanding and applications*, National Academy Press.
- Neuman S. P. (2005) Trends, prospects and challenges in quantifying flow and transport through fractured rocks, *Hydrogeology Journal*, 13(1), 124–147.
- Neuman S. P. and Tartakovsky D. M. (2009) Perspective on theories of non-Fickian transport in heterogeneous media, *Advances in Water Resources*, 32(5), 670–680.
- O'Malley D. and Vesselinov V. V. (2014) Analytical solutions for anomalous dispersion transport, *Adv. Water Resour.*, 68, 13–23.
- Outters N. (2003) *A generic study of discrete fracture network transport properties using FracMan/MAFIC*, Rep. R-03, 13.

- Outters N., Shuttle D. (2000) *Sensitivity analysis of a discrete fracture network model for performance assessment of aberg*, Tech. rep., Swedish Nuclear Fuel and Waste Management Co., Stockholm, Sweden.
- Painter S. (2006) *Effect of single-fracture aperture variability on field-scale transport*, Technical report, SKB.
- Painter S. and Cvetkovic V. (2005) Upscaling discrete fracture network simulations: An alternative to continuum transport models, *Water Resources Research*, 41, W02002.
- Painter S. and Mancillas J. (2013) *Marfa user's manual: migration analysis of radionuclides in the far field*, Posiva Working Report 1.
- Painter S., Cvetkovic V., and Selroos J.-O. (2002) Power-law velocity distributions in fracture networks: Numerical evidence and implications for tracer transport, *Geophysical Research Letters*, 29(14), 20-1-20-4.
- Painter S. L., Gable C. W., and Kelkar S. (2012) Pathline tracing on fully unstructured control-volume grids, *Computational Geosciences*, 16(4), 1125-1134.
- Painter S., Cvetkovic V., Mancillas J. and Pensado O. (2008) Time domain particle tracking methods for simulating transport with retention and first-order transformation, *Water Resources Research*, 44 (1).
- Pebesma E.J. (2004) Multivariable geostatistics in S: the gstat package, *Computers & Geosciences*, 30(7), 683-691
- Pebesma E.J. and Wesseling C.G. (1998) Gstat, a program for geostatistical modelling, prediction and simulation, *Computers & Geosciences*, 24(1), 17-31.
- Pichot G., Erhel J., and De Dreuzy J. R. (2010) A mixed hybrid mortar method for solving flow in discrete fracture networks, *Applicable Analysis*, 89(10), 1629-1643.
- Pichot G., Erhel J., and De Dreuzy J. R. (2012) A generalized mixed hybrid mortar method for solving flow in stochastic discrete fracture networks, *SIAM Journal of Scientific Computing*, 34(1), B86-B105.
- Pierre M. A., Jean-Francois T., and Valeri V. M. (2012) *Fractured Porous Media*, Oxford University Press.
- Pruess K., Oldenburg C. M., and Moridis G. J. (1999) *TOUGH2 user's guide version 2*.
- Ruppert J. (1995) A Delaunay refinement algorithm for quality 2-dimensional mesh generation, *Journal of Algorithms*, 18(3), 548-585.
- Schwartz F. W. and Smith L. (1988) A continuum approach for modeling mass transport in fractured media, *Water Resour. Res.*, 24(8), 1360-1372.
- SKB (2011) *Long-term safety for the final repository for spent nuclear fuel at Forsmark. main report of the SR-site project*, Technical Report SKB TR-11-01, Swedish Nuclear Fuel and Waste Management Co., Stockholm, Sweden.
- Smith L. and Schwartz F. W. (1984) An analysis of the influence of fracture geometry on mass transport in fractured media, *Water Resour. Res.*, 20(9), 1241-1252.
- Tsang C.-F. and Neretnieks I. (1998) Flow channeling in heterogeneous fractured rocks, *Reviews of Geophysics*, 36(2), 275-298.
- Tsang Y. W. and Tsang C. F. (1989) Flow channeling in a single fracture as a two-dimensional strongly heterogeneous permeable medium, *Water Resour. Res.*, 25(9), 2076-2080.

- Tsang Y., Tsang C., Neretnieks I., and Moreno L. (1988) Flow and tracer transport in fractured media: A variable aperture channel model and its properties, *Water Resour. Res.*, 24(12), 2049–2060.
- Vanderborght J., Mallants D., and Feyen J. (1998) Solute transport in a heterogeneous soil for boundary and initial conditions: Evaluation of first-order approximations, *Water Resour. Res.*, 34(12), 3255–3270.
- Vesselinov V. and Harp D. (2012) Model analysis and decision support (mads) for complex physics models, In *XIX International conference on water resources-CMWR*.
- Xu C., Dowd P. A., Mardia K. V., and Fowell R. J. (2006) A connectivity index for discrete fracture networks, *Mathematical Geology*, 38(5), 611–634.
- Zyvoloski G. A. (2007) *FEHM: A control volume finite element code for simulating subsurface multi-phase multi-fluid heat and mass transfer*, Los Alamos Unclassified Report LA-UR-07-3359.
- Zyvoloski G. A. and Vesselinov V. V. (2006) An investigation of numerical grid effects in parameter estimation, *Groundwater*, 44(6), 814–825.

## 2. LABORATORY INVESTIGATION OF COLLOID-FACILITATED TRANSPORT OF CESIUM BY BENTONITE COLLOIDS IN A CRYSTALLINE ROCK SYSTEM

### 2.1 Introduction

The most likely mechanism for strongly-adsorbing radionuclides to be transported significant distances in groundwater after being released from waste packages in a high-level nuclear waste repository is by colloid-facilitated transport. Barring a strong association with mobile colloids, strongly-adsorbing radionuclides are generally predicted to have negligible impact on dose estimates in repository risk assessments because they aren't expected to transport far enough to reach potential receptors. The objective of this study was to quantify the potential for colloid-facilitated transport of one strongly-adsorbing radionuclide, cesium (as  $^{137}\text{Cs}$ ), through a weathered fractured granodiorite system. Cs was adsorbed to bentonite clay colloids before injection through columns packed with geologic media to provide estimates of desorption rate constants (from colloids) and other parameters that are important for performance assessment calculations. While our studies focused on a specific crystalline rock system, the method(s) we developed can, in principle, be applied to any geologic setting in which colloid-facilitated transport in groundwater is a potential mechanism for radionuclide release to the accessible environment. The methods are intended to especially provide insights into upscaling of colloid-facilitated radionuclide transport predictions in time and space.

For this study, we selected a fractured/weathered granodiorite at the Grimsel Test Site (GTS) in Switzerland as a model crystalline rock repository system because the system has been thoroughly studied (e.g., Geckeis et al., 2004; Huber et al., 2011), and field experiments involving radionuclides have already been conducted at this site (Geckeis et al., 2004; Möri, 2004; Wang et al., 2013; Dittrich et al., 2014). Working on this system provides a unique opportunity to compare lab experimental results with field-scale observations.

Field experiments and observations in a shear zone at the GTS have shown that Cs transport in a fractured crystalline environment can be enhanced by the presence of bentonite colloids (Geckeis et al., 2004; Möri, 2004; Wang et al., 2013). In an experiment conducted at the GTS in 2002 as part of the a Colloid and Radionuclide Retardation (CRR) project, a significant fraction (~60%) of  $^{137}\text{Cs}$  associated with colloids transported essentially conservatively in a dipole tracer test conducted between two boreholes completed in the shear zone. The mean conservative tracer residence time in this experiment was on the order of 2 hours, with peak tracer concentrations occurring in about 70 minutes. Interestingly, a second peak of  $^{137}\text{Cs}$ , accounting for less than 10% of the injected mass, was observed at about 100 times longer than the first peak. This peak likely reflected the retardation of dissolved  $^{137}\text{Cs}$  that was not associated with the colloids (or had become dissociated from the colloids during transport through the shear zone), as the colloid concentrations had essentially declined to background long before this peak was observed (Geckeis et al., 2004; Möri, 2004). In 2012, a second colloid-facilitated transport experiment involving  $^{137}\text{Cs}$  was conducted at the GTS under the Colloids Formation and Migration (CFM) project (Wang et al., 2013). This experiment was conducted in a different dipole than the 2002 test (between a borehole and the access tunnel wall) and with a mean residence time of about 34 hours. In this experiment, the  $^{137}\text{Cs}$  recovery was only about 10% and the breakthrough curve closely matched the shape of the bentonite colloid breakthrough curve, indicating that the observed  $^{137}\text{Cs}$  was essentially all associated with the colloids. A second  $^{137}\text{Cs}$  peak was not observed in this experiment, although this may have been because the experiment was not conducted long enough to observe such a peak. A second peak would have taken about a year to arrive if the delay relative to the first peak was the same as in the 2002 experiment.

Laboratory experiments to evaluate the association of Cs with bentonite or smectite colloids have been conducted by several research groups (Murali and Mathur, 2002; Missana et al., 2004; Geckeis et al., 2004; Kurosawa et al., 2004; Iijima et al., 2010). The experiments of Missana et al. (2004), Geckeis et al.

(2004) and Iijima et al. (2010) focused on the Grimsel system, although the bentonite colloids used by Iijima et al. (2010) were derived from a different bentonite source. These experiments, and in particular the work of Missana et al. (2004), have shown that Cs sorption to GTS bentonite colloids has a nonlinear dependence on Cs concentrations and that desorption of at least a portion of the sorbed Cs is slow and potentially incomplete (partial sorption irreversibility). The dependence of Cs partition coefficients ( $K_d$  values) onto the bentonite colloids as a function of Cs concentration measured by Missana et al. (2004) is reproduced in Figure 2-1. In general, the work of the other research groups mentioned above are in reasonable agreement with Missana et al. (2004) when the Cs concentrations in the respective experiments are considered.

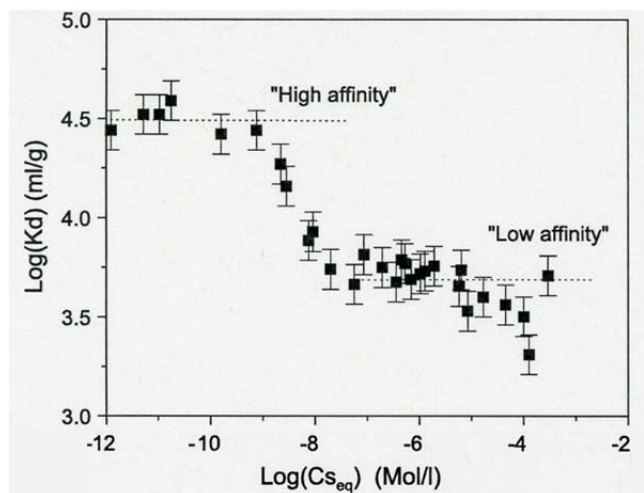


Figure 2-1. Batch adsorption  $K_d$  values for  $^{137}\text{Cs}$  on same bentonite colloids as used in this study in GTS groundwater as a function of Cs concentration (reproduced from Missana et al., 2004).

In this study, we conducted both batch and column transport experiments to refine and parameterize a colloid-facilitated transport model and to provide insight into potential colloid-facilitated transport of Cs isotopes in a crystalline rock repository. The batch experiments included both Cs adsorption and desorption experiments onto fracture fill material (FFM) obtained from the GTS shear zone. We also measured the partitioning of Cs onto colloids that were prepared from the same bentonite that was used in the GTS field experiments (also the same bentonite used by Missana et al., 2004). The starting concentration of Cs in these experiments was not varied, but rather was kept the same as the injection solutions for the column experiments so that we could compare the batch test parameters with parameters derived from the column experiments. Column experiments were conducted with (1) Cs injected without colloids, (2) Cs injected pre-sorbed onto colloids with the colloid pulse ending at the same time as the Cs pulse, and (3) Cs injected pre-sorbed onto colloids with the colloids continuously fed through the column after the Cs pulse had ended.

An update of work conducted for the Colloids Formation and Migration Project at the Grimsel Test Site is not included in this report other than to say that the majority of the work over the past 1-1/2 years has involved the emplacement and subsequent long-term monitoring of a radionuclide-doped bentonite plug into a borehole at the GTS that intersects the flowing shear zone in which previous colloid-facilitated radionuclide transport experiments were conducted. The emplacement of the doped bentonite was accomplished in May 2014, and since then monitoring has indicated that the bentonite rapidly (within about 2 weeks) swelled to fill and pressurize the emplacement interval (between two packers instrumented with pressure sensors) and that a small amount of the conservative dye tracer included with the doped bentonite has appeared at both a near-field monitoring borehole (located several cm from the main emplacement hole) and at the access tunnel wall where a surface packer is being used as a controlled



hydrologic sink. It also appears that the near-field monitoring borehole is registering a slight increase in groundwater turbidity, which suggests the appearance of colloids eroding from the bentonite plug. These results are all very preliminary, and as a courtesy to the CFM project participants, it would not be appropriate to present them in written form for the first time in this report.

## 2.2 State of the Art

The current state of the art in conducting colloid-facilitated contaminant/radionuclide transport experiments and in modeling colloid-facilitated transport has been addressed at length in the literature. Excellent reviews are provided by Grolimund et al. (2007), Bertetti et al. (2006), Kanti and Khilar (2006), Grolimund and Borkovec (2005), Painter et al., (2002), and Kersting and Reimus (2003). These reviews cite many earlier efforts. Modeling of colloid-facilitated contaminant transport has progressed very little in the past 20 years, but incremental advances have been made in parameterizing models and reducing uncertainty in model predictions by designing and conducting experiments that better interrogate the processes that result in colloid-facilitated transport over long time and distance scales (i.e., slow desorption colloids and slow or reversible colloid filtration). For example, in Dittrich et al. (2014 and 2015a), we introduced a method of reinjecting effluent from colloid-facilitated radionuclide transport column experiments into subsequent columns to allow better interrogation of slow desorption kinetics from colloids, which are very important for predicting colloid-facilitated transport in upscaled systems. In this study, we build on that approach and apply it to a study of the colloid-facilitated transport of Cs.

## 2.3 Technical Approaches (Materials and Methods)

We conducted a series of batch adsorption and desorption experiments, as well as three flow-through experiments in small columns to evaluate the colloid-facilitated transport of Cs in the shear zone at the GTS. The materials and methods are described in this section.

### 2.3.1 Groundwater

The groundwater used in all experiments was synthetic shear zone water (SZW) that matched the water chemistry of the water in the shear zone at the Grimsel Test Site. The SZW was prepared by adding analytical grade reagents to filtered, high-purity water ( $> 18 \text{ M}\Omega \text{ cm}$  resistivity) according to the concentrations of constituents listed in Table 2-1.

The ionic strength (0.66 mM) was calculated from the added reagents and a pH of 8.0 was measured the solution equilibrated with the atmosphere in Los Alamos, NM (2,231 m above sea level). The carbonate concentration listed in Table 3-1 is as prepared, not after equilibration with the atmosphere.

Table 2-1. Synthetic shear zone water constituents.

Constituent	mg/L
Na	14.97
K	0.20
Mg	0.02
Ca	5.60
Cl	5.67
SO <sub>4</sub>	5.85
F	6.00
Si	9.96
CO <sub>3</sub> +HCO <sub>3</sub>	20.06
Ionic Strength	0.66 mM
pH	8.0

### 2.3.2 Geologic Media

Weathered fracture fill material, or FFM (also known as fault gouge), was collected by coring the MI shear zone at the Grimsel Test Site (GTS) in Switzerland. The shear zone is not currently exposed in the CFM tunnel (where the field transport experiments were conducted), so the material was collected in an adjacent tunnel. The shear zone occurs where a fracture in the granite rock had been exposed to hydrothermal solutions and was altered over time. Samples were shipped to Los Alamos National Laboratory in pieces ranging from micron size up to 10-15 cm long. Due to the small quantity of material available, all pieces less than 1 cm in size were combined and crushed using a percussion mortar, sieved into 75-150, 150-355, and 355-500  $\mu\text{m}$  size fractions, and thoroughly rinsed in high-purity water to removal all fines. The samples were then rinsed with synthetic Grimsel shear zone water (SZW) until the electrical conductivity of solution in contact with the material for 24 hours was within 5% of the electrical conductivity of the SZW. Samples were then oven dried for 12 hours at 60 °C and stored in glass jars. Optical microscope (Wild Heerbrugg, M420) photographs of the 150-355  $\mu\text{m}$  size fraction of the FFM and the unaltered granodiorite matrix show that the FFM appears to have a larger fraction of dark grains (Figure 2-2).

The mineralogy of the granodiorite and FFM were determined by quantitative x-ray diffraction (QXRD) at Los Alamos. Table 2-2 lists the major fractions for the unaltered granodiorite, a scraping from the shear zone surface and a bulk sample of the crushed FFM that we used for all experiments discussed in this report.

Table 2-3 shows the bulk chemical analysis of the granodiorite and bulk FFM by x-ray fluorescence spectroscopy. The main differences between the unaltered granodiorite and FFM were a significant

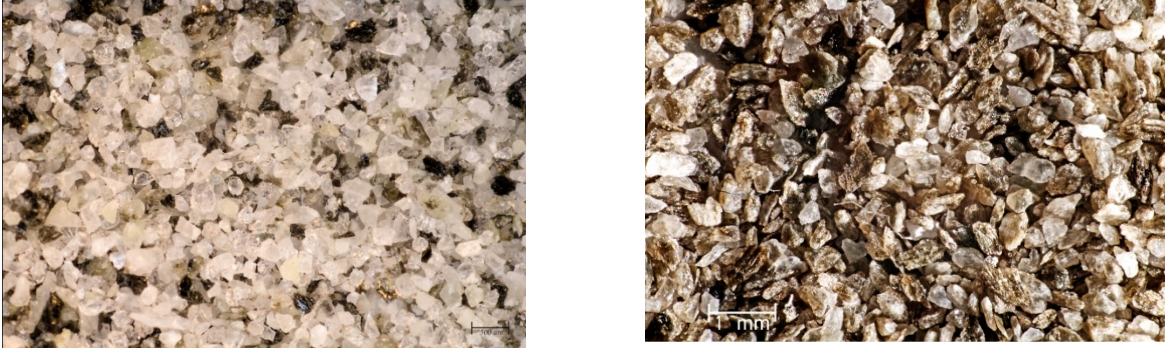


Figure 2-2. Microphotographs of crushed and sieved Grimsel granodiorite (left) and fracture fill material (right) in the 150-355  $\mu\text{m}$  size fraction (from Dittrich and Reimus, 2015 and Dittrich et al., 2015a).

Table 2-2. Quantitative X-ray diffraction interpretation (wt%) of Grimsel granodiorite, shear zone surface, and bulk FFM materials.

Mineral	Shear Zone		
	Granodiorite	Surface	FFM
Quartz	32	18	13
Microcline	10	8	5
Albite	42	44	34
Biotite	5	11	31
Chlorite	1	--	
Muscovite	10	19	16
Epidote	<1	--	--
Smectite	--	--	1
Calcite	--	<1	<1

Table 2-3. Bulk chemical analysis of granodiorite and FFM materials by X-ray fluorescence analysis (wt%).

Constituent	Granodiorite bulk	FFM bulk	Detection Limits
fuse ratio	7:1	7:1	7:1
Na <sub>2</sub> O	4.01	3.15	0.0451
MgO	0.725	4.28	0.0300
Al <sub>2</sub> O <sub>3</sub>	14.0	14.3	0.0313
SiO <sub>2</sub>	70.9	63.4	0.1507
P <sub>2</sub> O <sub>5</sub>	0.115	0.124	0.0049
K <sub>2</sub> O	4.22	4.90	0.0112
CaO	1.90	1.03	0.0084
TiO <sub>2</sub>	0.436	0.491	0.0092
MnO	0.081	0.086	0.0252
Fe <sub>2</sub> O <sub>3</sub>	3.10	3.83	0.0041
V	29	41	13
Cr	bdl	bdl	10
Co	bdl	bdl	15
Ni	bdl	bdl	5
Cu	bdl	bdl	5
Zn	31	53	5
Ge	bdl	bdl	24
As	bdl	bdl	15
Rb	110	192	4
Sr	135	71	5
Zr	217	236	6
Ba	403	372	19
W	bdl	bdl	43
U	bdl	bdl	4
LOI	0.35	4.28	
total	99.931	99.970	

bdl = below detection limit  
LOI = loss on ignition

enrichment in Mg, minor enrichment in K and Fe, and minor depletions of Si, Na, and Ca in the FFM relative to the parent granodiorite.

The surface area of the FFM was determined by the BET method with krypton gas (Micromeritics Analytical Services) and was measured as 0.23 m<sup>2</sup> g<sup>-1</sup> for the 150-355 μm size fraction used in all experiments.

### 2.3.3 Bentonite Colloids

Bentonite colloids were processed from a brick of compressed bentonite from the Corijo de Archidona deposit (Almeria, Spain) that was shipped to us by our colleagues from the Grimsel Test Site in Switzerland. This material is also called FEBEX bentonite because it was used in the Full-scale high-level waste Engineered Barriers EXperiment at the GTS, which goes by the acronym FEBEX. The major mineralogy of this bentonite, as determined by quantitative XRD by our European colleagues, is given in Table 2-4. Samples of the brick were crushed in a ceramic mortar and pestle and sieved to retain the size fraction less than 75  $\mu\text{m}$ . The bentonite colloids were sodium saturated to enable comparison of our results with other published results (Huber et al., 2011). 50 g of material was added to 1 L of 1 M NaCl and was placed on a shaker table for 7 days. The supernatant was decanted and the removed liquid was replaced with new 1 M NaCl and placed on the shaker for 7 additional days. This process was repeated 3 times and the solution conductivity was measured (VWR Series 500, Model 2052 meter and VWR 525 conductivity dip cell/electrode, Model 23198-020) to ensure completeness of the exchange process. The resulting suspension was settled and the supernatant was decanted and replaced with SZW. This process was repeated 6 times until the conductivity of the supernatant was reduced below 2.5 mS/cm and the colloids did not readily settle. The suspension was then placed in a sonic bath for 30 min, centrifuged for 12 hr, and the supernatant removed and replaced with SZW. This process was repeated 10 times until the resulting conductivity of the bentonite suspension was within 1% of the SZW. Various steps of the process are depicted in Figure 2-3.

The suspension was then diluted to 1 g L<sup>-1</sup> with SZW and was settled in 1 L graduated cylinders for 2 weeks to obtain a stable experimental suspension. The top 700 mL was decanted and Stokes' Law was applied to calculate a theoretical maximum particle size of less than 1  $\mu\text{m}$ . The final stock suspension was then passed through a 0.8- $\mu\text{m}$  filter to remove any larger particles. A single particle counter was used to measure the particle size distribution of the stock suspension. Very few particles larger than 220  $\mu\text{m}$  were present (Figure 2-4).

The concentration of the stock suspension was calculated to be (1540 mg L<sup>-1</sup>) by drying 25 mL of suspension on a watch glass (in triplicate) and determining the weight difference after drying. The stock suspension was diluted to 100 mg L<sup>-1</sup> and was stored in a sealed glass bottle. Surface area of the dried colloids was measured by the BET method with nitrogen gas to be 56.1 m<sup>2</sup> g<sup>-1</sup>.

Table 2-4. Quantitative X-ray diffraction interpretation (wt%) of FEBEX bentonite.

Mineral	Bentonite
Quartz	2 ± 1
Plagioclase (Na, Ca)	3 ± 1
Cristobalite	2 ± 1
Feldspars	Trace
Smectite	92 ± 3
Calcite	1 ± 0.5

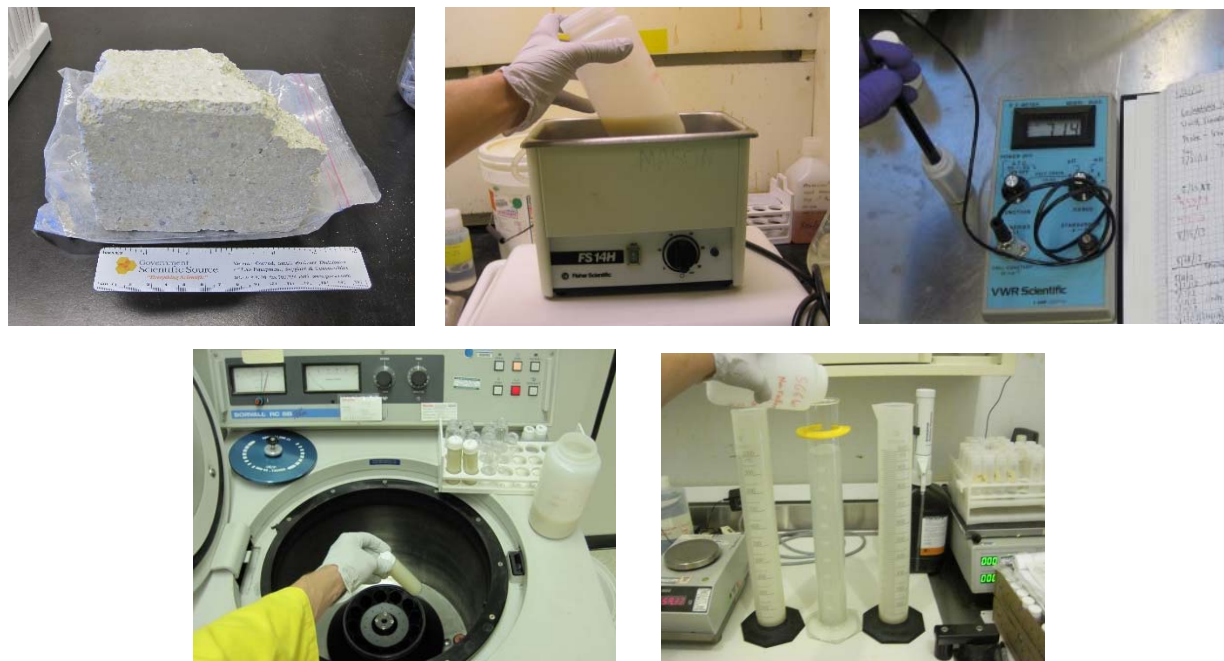


Figure 2-3. Various steps in preparation of colloid suspension from FEBEX bentonite brick.

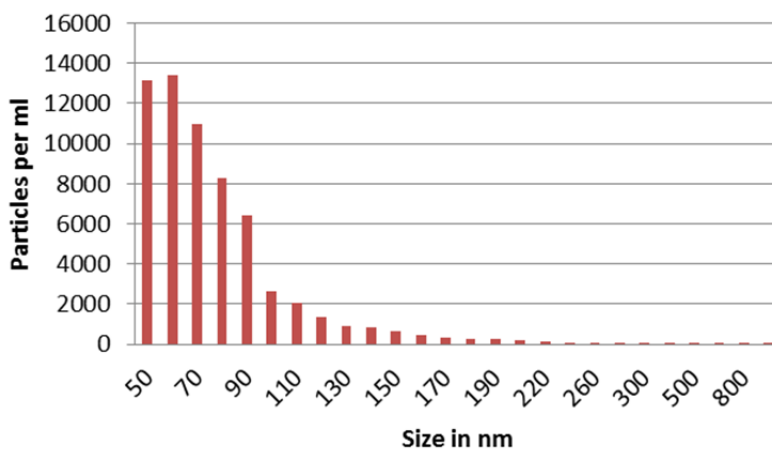


Figure 2-4. Particle size distribution of FEBEX bentonite colloid suspension as measured by a single particle counter. Note that the concentration scale on the y-axis does not account for sample dilution in the final suspension used in the experiments.

### 2.3.4 Cesium and Tritiated Water

The Cs used in all experiments was taken from a  $^{137}\text{CsCl}$  stock in 0.1 M HCl (Eckert and Ziegler). The stock solution contained 3.056  $\mu\text{Ci}$  of  $^{137}\text{Cs}$  (referenced to 10/1/2011) in 100 ml of aqueous solution, corresponding to a concentration of  $2.6\text{e-}9$  M  $^{137}\text{Cs}$ . The solution contained 10  $\mu\text{g/ml}$ , or  $7.5\text{e-}5$  M, of carrier (nonradioactive) Cs. When the SZW with 100 mg/L of suspended bentonite colloids was initially spiked with a small amount of this solution, NaOH was added to the suspension to neutralize the HCl from the stock solution and re-establish the pH of 8. This NaOH addition resulted in exceeding the ionic strength threshold for colloid stability, which led to the colloids aggregating and settling to the bottom of

the container. The colloids were resuspended by decanting off most of the supernatant and adding enough fresh SZW to re-establish the 100 mg/L colloid concentration (and also to re-establish the unaltered or only slightly-altered Na and Cl concentrations in the SZW). The resulting solution was sonicated to re-disperse the colloids, and after sonication and settling, the colloid size distribution was found to be essentially indistinguishable from the original size distribution shown in Figure 2-4. After this procedure, the  $^{137}\text{Cs}$  concentration in the suspension was about  $3\text{e-}11\text{ M}$ , and the total Cs concentration was inferred to be  $\sim 9\text{e-}7\text{ M}$ . This process was repeated for subsequent batches of Cs-spiked colloid suspensions. The suspensions were allowed to equilibrate for at least 1 week. All suspensions were stored in Teflon® bottles until used in experiments.

Tritium in the form of tritiated water ( $^3\text{HHO}$ ) was added to the Cs and bentonite suspensions and was used as a conservative tracer to provide groundwater residence times and dispersivities in the column experiments.

### 2.3.5 Analytical Measurements

$^{137}\text{Cs}$  and tritium concentrations were measured by liquid scintillation counting, or LSC (Perkin Elmer Tri-Carb 2550) with energy ranges of 0-15 keV for tritium and 15-225 keV for  $^{137}\text{Cs}$  (energies uncorrected for quenching). A 1 mL aliquot of sample was combined with 5 mL of deionized water and 14 mL of liquid scintillation cocktail (Packard, Ultima Gold AB) in a polypropylene scintillation vial to yield 20 mL total. The vial was vigorously shaken for at least 15 seconds to ensure mixing between the cocktail and the sample, and samples were counted for two 15 minute increments and the results were averaged. The transformed index of an external  $^{133}\text{Ba}$  standard (tSIE) was used to correct for variable quenching of the samples, especially with respect to tritium.

Total  $^{137}\text{Cs}$  concentrations were measured with uncentrifuged column effluent and dissolved  $^{137}\text{Cs}$  was measured by centrifuging the sample at 15,000 RPM for 12 hours and then analyzing 1 mL of the supernatant for  $^{137}\text{Cs}$  concentration. Colloid-associated  $^{137}\text{Cs}$  was then calculated as the difference between the total and dissolved  $^{137}\text{Cs}$  concentration for each sample.

pH of the solutions, suspensions, and breakthrough experiment samples were measured using a pH meter (Orion, Model 290) and a glass pH electrode (Fisher, AccupHast) calibrated with 4.01, 7.00, and 9.01 pH buffer solutions (Ricca Chemical Corp.).

Colloid concentrations of the bentonite suspensions in the column breakthrough experiments were measured using turbidimetry. The turbidimeter (Hach, 2100N) was calibrated with standards (0.1, 1, 5, 10, 20, 40, 60, 80, 100  $\text{mg L}^{-1}$ ) and the same 12 mm borosilicate glass test tube was used for every measurement to reduce error from test tube variability. Colloid concentrations were calculated using a correlation function derived to relate colloid concentration with the measured NTU (nephelometric turbidity units) of the samples.

### 2.3.6 Batch Experiments

Batch adsorption and desorption experiments were conducted to evaluate the interaction of Cs with crushed FFM that was used in the column experiments. The experiments were performed in duplicate in polycarbonate centrifuge tubes, and a control experiment without the FFM was also conducted to allow corrections for any interaction of the Cs with the centrifuge tube walls. All sorption experiments were conducted using colloid-free SZW spiked with  $^{137}\text{Cs}$  to the same concentration as in the colloid suspensions (with appropriate dilution with SZW to match the Na and Cl concentrations; see Section 7.3.4). In the reactors containing FFM, 20 ml of  $^{137}\text{Cs}$ -spiked colloid-free SZW was placed in contact with 0.25 g of the FFM. The sorption experiments were conducted for  $\sim 70$  hours, with samples collected from the centrifuge tubes after 2.5 and 30 min, and also after 3.1, 5.25, 20.3, 40.6 and 68.9 hr. All but approximately 1 ml of the remaining solution was then decanted off, and 20 ml of  $^{137}\text{Cs}$ -free SZW was added to start duplicate desorption experiments (with a control as well). In the desorption experiments, samples were collected after 1, 7, 22 and 48 min, and also after 3.7, 6.1, 21.5, 46.1 and 70 hrs. All but 1

ml of the remaining solution was then again decanted off and 20 ml of  $^{137}\text{Cs}$ -free SZW was added to start a second desorption step/experiment. However, for this step, one of the centrifuge tubes containing FFM received SZW that contained suspended colloids at 100 mg/L while the other received colloid-free SZW. In these desorption experiments, samples were collected after 1, 10, 20, 45, 70 min, and also after 3.6, 5.75, 21.4, 28.6, 48.5, 76 and 142 hrs.

Formal sorption and desorption experiments were not conducted to evaluate  $^{137}\text{Cs}$  partitioning between the bentonite colloids and the SZW, but this partitioning was measured numerous times throughout the course of the study, and the  $^{137}\text{Cs}$  was consistently found to be about 23-25% associated with the colloids and 75-77% in the solution phase. This result translates to a partition coefficient, or  $K_d$  value, of approximately 3700 ml/g, which is consistent with the results of Missana et al. (2004) for concentrations exceeding about  $1\text{e-}8$  M Cs (see Figure 2-1).

### 2.3.7 Column Transport Experiments

Column transport experiments were conducted by eluting Cs and bentonite suspensions through columns packed with FFM in the 150-355  $\mu\text{m}$  size range. Small columns were constructed from 1.5 cm lengths of 0.95 cm diameter Teflon<sup>®</sup> tubing (Dittrich et al., 2015b). The ends of the tubes were tapped to accept Teflon<sup>®</sup> compression fittings. The inside openings were covered with a small disk of 75  $\mu\text{m}$  PEEK screen to retain the column material while providing minimum resistance to flow and causing negligible straining of colloids. Teflon<sup>®</sup> tubing (1/16<sup>th</sup>-inch ID) and 3-way polycarbonate stopcocks were used to connect the columns to 60 mL polypropylene syringes (Becton Dickinson) installed on syringe pumps (KD Scientific, Model 100). 3-way stopcocks allowed for refilling syringes and switching suspensions or solutions while minimizing flow and pressure disturbances that may affect colloid retention. Flow was directed upward to help maintain saturation and to minimize the potential for air bubbles collecting in the columns. An additional length of 1/16<sup>th</sup>-inch ID Teflon<sup>®</sup> tubing was connected to the top (outlet side) of the column and directed column effluent to a fraction collector (Gilson, FC-220) filled with 13  $\times$  100 mm polystyrene test tubes. The fraction collector was enclosed in an acrylic plastic chamber with evaporation pans filled with deionized water to minimize evaporation before sample analysis. Figure 2-5 shows a picture of the column experiment setup.

Columns were packed with 1.5 g of dry FFM, resulting in a porosity of approximately 0.4 and a bulk density of about 1.6 g/cm<sup>3</sup>. The columns were initially flushed at  $\sim$ 0.3 ml/hr with  $^{137}\text{Cs}$ -,  $^3\text{HHO}$ -, and colloid-free SZW for 7 days and the pH was monitored to ensure effluent pH stabilized within 0.1 pH units of the influent solution (pH  $8.0 \pm 0.1$ ) before the start of a radionuclide/colloid injection.

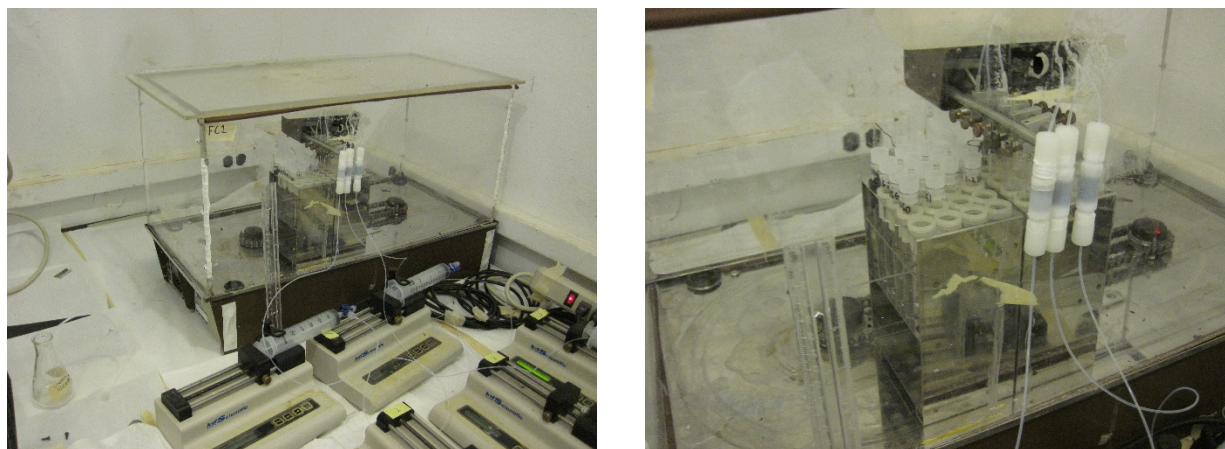


Figure 2-5. Photos of column experiment setup with three 1.5-cm-long columns running in parallel with syringe pumps, tubing, and fraction collector.



To begin each breakthrough experiment, the background solution was switched to either a bentonite suspension in SZW (100 mg/L bentonite) that contained  $^3\text{HHO}$  and  $^{137}\text{Cs}$  ( $3\text{e-}11\text{ M }^{137}\text{Cs}$ ,  $9\text{e-}7\text{ M}$  total Cs, see Section 7.3.4) or to colloid-free SZW containing the same concentrations of  $^3\text{HHO}$  and  $^{137}\text{Cs}$ . Two identical columns were used; one received the  $^{137}\text{Cs}$ -spiked colloid suspension and the other received the colloid-free spiked solution. The flow rates through the columns were nominally  $\sim 0.28\text{ ml/hr}$ . Syringes were refilled several times during the experiment and were eventually changed to SZW free of  $^3\text{HHO}$ ,  $^{137}\text{Cs}$ , and bentonite colloids to observe the flushing of the colloids and  $^{137}\text{Cs}$  from the columns. Samples were collected at 12 hr intervals and the sample mass was weighed with a digital balance (Mettler, PL1200) and subtracted from the empty test tube weight to calculate the actual flow rates. Total and dissolved  $^{137}\text{Cs}$  activity, tritium activity, and colloid concentrations were measured (see Section 7.3.5) for every sample early in the breakthroughs and then less often as the experiments progressed.

Once the  $^{137}\text{Cs}$  concentration in the effluent from the column injected with the colloid suspension reached the inlet  $^{137}\text{Cs}$  concentration, the effluent that wasn't used for radionuclide or colloid analyses was stored in a Teflon<sup>®</sup> bottle for re-use. This combined effluent was then injected into another FFM-filled column that had not been previously exposed to colloids or  $^{137}\text{Cs}$ . The same procedure was followed as the other two columns except that after the injection solution was exhausted, the solution in the syringes was changed to  $^3\text{HHO}$ - and  $^{137}\text{Cs}$ -free SZW that contained suspended colloids at the same concentration as the combined effluent injected at the beginning of the experiment. Thus, while the injection of  $^3\text{HHO}$  and Cs ceased, the injection of colloids continued without interruption for the remainder of the experiment.

At the end of each column experiment, a 0.1 M HCl solution was flushed through the column to desorb any  $^{137}\text{Cs}$  remaining in the column and attempt to close the Cs mass balance for the experiment.

Control column experiments containing no FFM but with all the other experimental components were also conducted to evaluate interaction of Cs with any of the components other than the FFM, and it was found that interactions were negligible, so the results of these experiments are not presented in this report.

### 2.3.8 Interpretive Modeling

The batch experiments were interpreted by simply calculating  $^{137}\text{Cs}$  partition coefficients near the end of the experiments for either adsorption or desorption. The partition coefficients were calculated as:

$$\text{Adsorption: } K_d = \frac{V(C_0 - C)}{M} \quad (2-1)$$

$$\text{Desorption: } K_d = \frac{V_{des} [(C_0 - C)_{ads} V_{ads} + C_{ads} V_{res,ads} - CV_{des}]}{M} \quad \text{or} \quad K_d = \frac{V_{des} S}{M} \quad (2-2)$$

where,  $V$  = volume of solution, ml

$M$  = mass of FFM or colloids, g

$C$  = concentration at end of experiment, mol/ml

$C_0$  = concentration at beginning of experiment, mol/ml

$S$  = concentration on FFM or colloids, mol/g (calculated using data from previous step)

$ads$  = subscript for adsorption step

$des$  = subscript for desorption step

$V_{res,ads}$  = volume of residual solution remaining behind after adsorption step, ml

The adsorption and desorption rate constants were not estimated from the batch experiments because the rates were observed to be very rapid – so much so that they were thought to be potentially limited by mass transfer rates in the batch reactors, especially considering the large volume to solid mass ratios in the centrifuge tubes. Also, when sorption site capacities are allowed to vary, estimates of rate constants from batch experiments are notoriously nonunique (a smaller site capacity and faster rate constants will often yield equally good fits to a data set as a larger site capacity and smaller rate constants). Thus, rather than

attempt to estimate rate constants from the batch experiments, the rate constants were estimated by interpreting the column experiment data, and then the rates deduced from the columns were used to do a forward prediction of the batch sorption/desorption experiments. The forward batch experiment model was embodied in a Fortran program that allowed multiple sites with different rate constants and adsorption capacities (Dittrich et al., 2014). The governing equations of the model were:

$$\text{Solution: } \quad \frac{\partial c}{\partial t} = \frac{M}{V} \left[ -\sum_i k_{fi} c \left( 1 - \frac{s_i}{s_{mi}} \right) + \sum_i k_{ri} s_i \right] \quad (2-3)$$

$$\text{Solids: } \quad \frac{\partial s_i}{\partial t} = k_{fi} c \left( 1 - \frac{s_i}{s_{mi}} \right) - k_{ri} s_i \quad (2-4)$$

where,  $c$  = concentration in aqueous phase, mol/ml

$s_i$  = concentration on surface sorption site  $i$ , mol/g

$t$  = time, hr

$k_{fi}$  = adsorption rate constant for sorption site  $i$ , ml/g-hr

$k_{ri}$  = desorption rate constant for site  $i$ , hr<sup>-1</sup>

$s_{mi}$  = surface site density (maximum adsorption capacity) for sorption site  $i$ , mol/g

$M$  = mass of solids, g

$V$  = volume of solution, ml.

In addition to solving equations (3) and (4), the batch model allowed the volume of solution in the reactor to be changed at specified times to simulate sampling, and it also allowed for a specified volume of Cs-free water to be added to the reactor to simulate the start of the desorption phase of the experiments. Equations (3) and (4) were solved using a 4<sup>th</sup>-order Runge-Kutta algorithm.

The model used to interpret the column transport experiments was also embodied in a Fortran program that was described previously in Dittrich et al. (2014). Although the model allows for dual-porosity transport (including diffusion into a stagnant secondary porosity that has sorption properties), it was found that the model matches to the column breakthrough curves were not improved by including a secondary porosity, so the secondary porosity features of the model are not described below.

#### Colloid Transport in Flowing Porosity:

$$\text{Mobile: } \quad \frac{\partial C_{col}}{\partial t} + v_f \frac{\partial C_{col}}{\partial x} - D_c \frac{\partial^2 C_{col}}{\partial x^2} + k_{fc} C_{col} - k_{rc} S_{col} + k_{fci} C_{col} - P_{col} = 0 \quad (2-5)$$

$$\text{Immobile: } \quad \frac{\partial S_{col}}{\partial t} - k_{fc} C_{col} + k_{rc} S_{col} - k_{fci} C_{col} = 0 \quad (2-6)$$

#### Solute Transport in Flowing Porosity:

$$\begin{aligned} & \frac{\partial C}{\partial t} + v_f \frac{\partial C}{\partial x} - D_f \frac{\partial^2 C}{\partial x^2} + k_{1f} C C_{col} \left( 1 - \frac{C_1}{C_{col} S_1^0} \right) + k_{2f} C C_{col} \left( 1 - \frac{C_2}{C_{col} S_2^0} \right) + \\ & \left( \frac{\rho_f}{\eta} \right) \left[ \sum_i k_{fi} C \left( 1 - \frac{s_i}{s_{mi}} \right) - \sum_i k_{ri} s_i \right] + k_{1f} C S_{col} \left( 1 - \frac{C_{filt,1}}{S_{col} S_1^0} \right) + k_{2f} C S_{col} \left( 1 - \frac{C_{filt,2}}{S_{col} S_2^0} \right) - \\ & k_{1b} C_1 - k_{2r} C_2 - k_{1b} C_{filt,1} - k_{2r} C_{filt,2} = 0 \end{aligned} \quad (2-7)$$

#### Solute Transport on mobile colloids while adsorbed to colloid sites 1 and 2:

$$\frac{\partial C_1}{\partial t} + v_f \frac{\partial C_1}{\partial x} - D_c \frac{\partial^2 C_1}{\partial x^2} - k_{1f} C C_{col} \left( 1 - \frac{C_1}{C_{col} S_1^0} \right) - k_{rc} C_{filt,1} + k_{1r} C_1 + k_{fc} C_1 - P_{col} S_a = 0 \quad (2-8)$$

$$\frac{\partial C_2}{\partial t} + v_f \frac{\partial C_2}{\partial x} - D_c \frac{\partial^2 C_2}{\partial x^2} - k_{2f} C C_{col} \left( 1 - \frac{C_2}{C_{col} S_2^0} \right) - k_{rc} C_{filt,2} + k_{2r} C_2 + k_{fc} C_2 - P_{col} S_b = 0 \quad (2-9)$$

Immobile Solute in Fractures (sorption sites a and b):

$$\frac{\partial S_i}{\partial t} - \sum_i k_{fi} C \left( 1 - \frac{S_i}{S_{mi}} \right) + \sum_i k_{ri} S_i = 0 \quad (2-10)$$

Immobile Solute adsorbed onto Immobile Colloids in Fractures (colloid sites 1 and 2):

$$\frac{\partial C_{filt,1}}{\partial t} - k_{1f} C S_{col} \left( 1 - \frac{C_{filt,1}}{S_{col} S_1^0} \right) - (k_{fc} + k_{fci}) C_1 + k_{rc} C_{filt,1} + k_{1r} C_{filt,1} = 0 \quad (2-11)$$

$$\frac{\partial C_{filt,2}}{\partial t} - k_{2f} C S_{col} \left( 1 - \frac{C_{filt,2}}{S_{col} S_2^0} \right) - (k_{fc} + k_{fci}) C_2 + k_{rc} C_{filt,2} + k_{2r} C_{filt,2} = 0 \quad (2-12)$$

where,  $C_{col}$  = concentration of colloids in solute phase, mol/cm<sup>3</sup>

$S_{col}$  = colloid concentration on media surfaces, mol/cm<sup>3</sup>

$C$  = solution concentration of solute in flowing porosity, mol/cm<sup>3</sup>

$S_i$  = sorbed concentration of solute on media surface site  $i$ , mol/g

$C_1$  = concentration of solute sorbed to site 1 on mobile colloids, mol/cm<sup>3</sup>

$C_2$  = concentration of solute sorbed to site 2 on mobile colloids, mol/cm<sup>3</sup>

$C_{filt,1}$  = concentration of solute sorbed to site 1 on immobile colloids, mol/cm<sup>3</sup>

$C_{filt,2}$  = concentration of solute sorbed to site 2 on immobile colloids, mol/cm<sup>3</sup>

$P_{col}$  = colloid production rate in flowing porosity, g/cm<sup>3</sup>-hr

$v_f$  = fluid velocity in flowing porosity, cm/hr

$D_f$  = solute dispersion coefficient in flowing porosity, cm<sup>2</sup>/hr

$D_c$  = colloid dispersion coefficient in flowing porosity, cm<sup>2</sup>/hr

$\rho_f$  = effective bulk density within flowing porosity, g/cm<sup>3</sup>

$\eta$  = porosity in flow domain

$k_{fc}$  = colloid filtration rate constant (1/hr) =  $\lambda v_f$ , where  $\lambda$  = filtration coefficient (1/cm)

$k_{rc}$  = reverse colloid filtration (detachment) rate constant, 1/hr

$k_{fci}$  = irreversible colloid filtration rate constant, 1/hr

$k_{fi}$  = rate constant for sorption of solute onto media surface site  $i$ , ml/g-hr

$k_{ri}$  = rate constant for desorption of solute from media surface site  $i$ , 1/hr

$k_{1f}$  = rate constant for sorption of solute onto colloid surface site 1, ml/g-hr

$k_{1r}$  = rate constant for desorption of solute from colloid surface site 1, 1/hr

$k_{2f}$  = rate constant for sorption of solute onto colloid surface site 2, ml/g-hr

$k_{2r}$  = rate constant for desorption of solute from colloid surface site 2, 1/hr

$S_1^0$  = maximum solute capacity on colloid sorption site 1, mol/g colloid

$S_2^0$  = maximum solute capacity on colloid sorption site 2, mol/g colloid

$S_{mi}$  = maximum solute capacity on media sorption site  $i$ , mol/g solid

The model allows for up to 5 different types of sorption sites, with different rate constants and sorption capacities, to be specified on the immobile media surfaces (the FFM), but it only allows for 2 different types of sorption sites on the colloids. Both reversible and irreversible colloid filtration can be simulated, although the bentonite colloids in this study transported essentially conservatively through the 1.5-cm columns, so the filtration rate constants were set to zero and filtration was effectively ignored.

The column modeling procedure involved first using the  $^3\text{HHO}$  breakthrough curves to obtain estimates of the mean residence time and dispersivity in the columns, and then these parameters were assumed to apply to the transport of colloids and Cs through the columns. Rapid and reversible adsorption of the Cs onto the colloids was assumed based on observations that the Cs partitioning to the colloids occurred as rapidly as could be measured when  $^{137}\text{Cs}$ -spiked suspensions were prepared. The ratios of adsorption rate constants to desorption rate constants for the Cs on both the colloids and the FFM were constrained by the partitioning observed in the batch experiments, but the rate constants themselves were allowed to vary to match the observed breakthrough curves. Further details of the procedure are provided in the next section.

## 2.4 Technical Results

### 2.4.1 Batch Experiment Results

The results of batch adsorption experiments of the Cs onto the FFM are shown in Figure 2-6. The duplicate FFM experiments are in excellent agreement, and the control experiment shows no evidence of any interaction of Cs with the centrifuge tubes. The partition coefficient, or  $K_d$  value, at the end of the experiment is calculated (eq. 2-1) to be approximately 51 ml/g. This value is much lower than the  $K_d$  value of  $\sim 3600$  ml/g calculated for Cs partitioning to the bentonite colloids, but when one considers the much larger specific surface area of the colloids vs. the FFM ( $56.1 \text{ m}^2/\text{g}$  vs.  $0.23 \text{ m}^2/\text{g}$ ), the Cs partition coefficient on a surface area basis is actually slightly larger for the FFM than for the colloids:  $220 \text{ ml}/\text{m}^2$  for the FFM vs.  $64 \text{ ml}/\text{m}^2$  for the colloids. The model curves shown in Figure 2-6 were generated using the batch adsorption model described in Section 7.3.8 with the sorption and desorption rate constants that provided the best matches to the column data (see Section 7.4.2), so they were not optimized to offer the best fits to the batch data. It is apparent that the parameters yielding a good match to the column data also provided reasonably good matches to the batch data, particularly in the case of the two-site model.

The results of the two desorption experiments evaluating Cs desorption from the FFM are shown in Figures 2-7 and 2-8, respectively. Figure 2-7 shows that the duplicate experiments are again in excellent agreement. The  $K_d$  value at the end of this experiment is calculated (eq. 2-2) to be approximately 200 ml/g, or nearly 4 times greater than the  $K_d$  value at the end of the adsorption experiment. This result indicates that there is some adsorption-desorption hysteresis, with at least a portion of the adsorbed Cs not readily desorbing from the FFM or desorbing at a slower rate than the remainder of the Cs. This result might also be interpreted as an indication of a nonlinear adsorption isotherm, as the Cs concentration in solution at the end of the desorption experiment is about a factor of 5.5 lower than at the end of the adsorption experiment. Either way, it appears that Cs was desorbed preferentially from weaker sorption sites and the Cs remaining on the FFM after desorption is, on average, more strongly associated with the FFM than the Cs at the end of the adsorption experiment. As in the case of Figure 2-6, the model curves in Figure 2-7 show the desorption of Cs from the FFM predicted using the model parameters that provided good matches to the column transport data (see Section 7.4.2). They are not optimized fits to the batch desorption data.

In Figure 2-8, there is a difference between the two desorption curves because the desorption solution added to one of the centrifuge tubes included Cs-free bentonite colloids at  $\sim 100$  mg/L while the other solution was colloid-free SZW. The data points for the experiment with colloids are measurements of samples that were not centrifuged to remove the colloidal fraction of Cs, so these data represent dissolved plus colloidal Cs concentrations. It is apparent that more of the Cs desorbed from the FFM when the

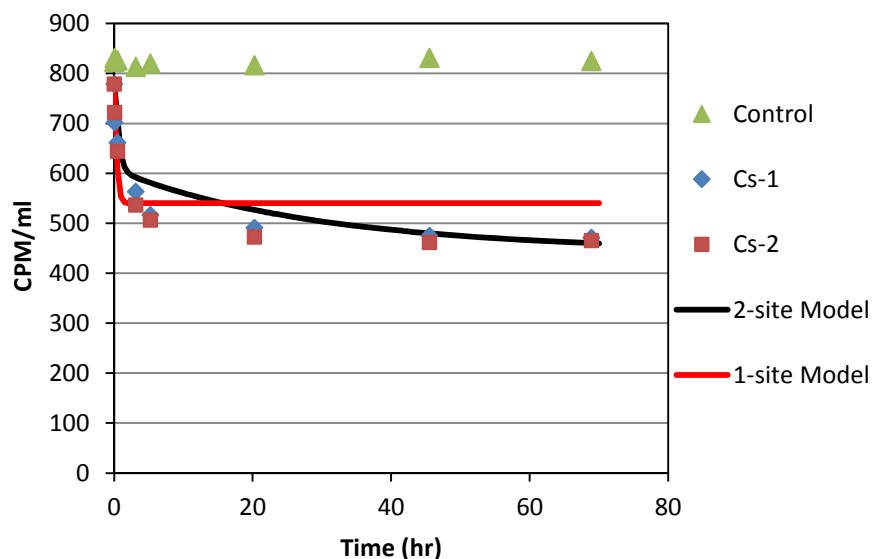


Figure 2-6. Results of batch adsorption experiment of <sup>137</sup>Cs onto FFM in SGW. 800 CPM/ml (starting concentration) corresponds to about 3e-11 M <sup>137</sup>Cs and about 9e-7 M total Cs. The one-site and two-site model curves were generated using the best-fitting parameters for the column experiments and do not represent fits to the batch data.

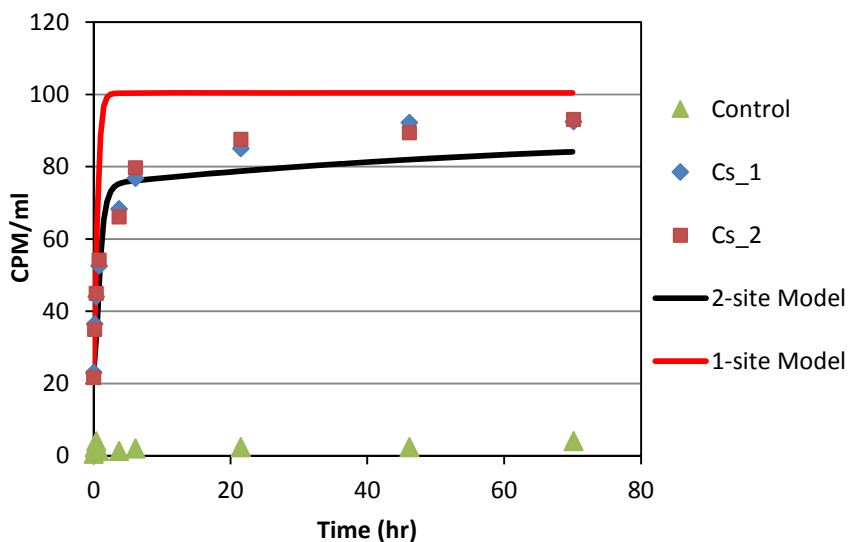


Figure 2-7. Results of batch experiment of first desorption step of <sup>137</sup>Cs from FFM in SGW. The one-site and two-site model curves were generated using the best-fitting parameters for the column experiments and do not represent fits to the batch data.

colloids were present. Furthermore, if one assumes that 25% of the solution-phase Cs in the colloid experiment is associated with the colloids (consistent with Cs partitioning to colloids in the absence of FFM), the concentration of dissolved Cs is nearly the same at the end of both experiments. The Cs-FFM  $K_d$  value at the end of this experiment is calculated to be approximately 320 ml/g, or nearly 6.5 times greater than the  $K_d$  value at the end of the adsorption experiment, and about 60% greater than at the end of

the first desorption experiment. This result indicates that as successively more Cs is desorbed from the FFM, the remaining adsorbed Cs is, on average, more and more strongly associated with the FFM. Note

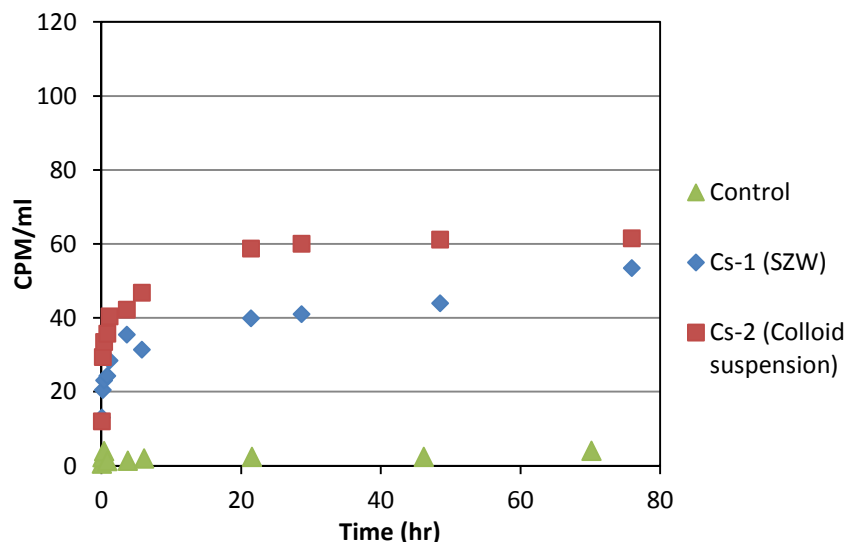


Figure 2-8. Results of batch experiment of second desorption step of  $^{137}\text{Cs}$  from FFM in SGW (starting with FFM remaining after first desorption step shown in Figure 2-7). Note that the Cs-1 experiment involved desorption in colloid-free SZW, while Cs-2 involved desorption in SZW containing 100 mg/L of bentonite colloids. Model curves are not shown because there was no column experiment that corresponded to a second desorption step. The y-axis scale is the same as in Figure 2-7 to allow comparison of the amounts of  $^{137}\text{Cs}$  desorbed.

that model curves are not shown in Figure 2-8 because the column experiments did not include the equivalent of a second desorption step.

Collectively, the batch experiment results suggest that there are multiple sorption sites on the FFM with different sorption and desorption rate constants and likely different sorption capacities. The batch data do not support a highly-refined determination of the rate constants and capacities of the different types of sites, but they certainly support the use of multiple sites when matching the column experiment data, which is important because it was found that the column data were much better matched when multiple sites were assumed.

## 2.4.2 Column Experiment Results

Figure 2-9 shows the Cs breakthrough curves in the FFM column experiments with and without colloids in the injection pulse. It is immediately apparent that the colloids transported through the column without significant filtration, as the colloid concentration jumped to its injection concentration ( $C/C_0 = 1$ ) after one pore volume and remained there until the injection pulse ended. This result greatly simplified the modeling of the experiments, making it possible to assume a colloid filtration rate constant of zero. The mean water residence time in the columns, as determined from the  $^3\text{HHO}$  breakthrough curves was approximately 1.5 hours, and the column Peclet number (column length divided by longitudinal dispersivity) was estimated to be around 100. Neither of these parameters were tightly constrained by the data because of the extremely rapid breakthrough of the  $^3\text{HHO}$ , which resulted in only one to three samples being collected that contained  $C/C_0$  values between 0 and 1.0.

The model fits to the Cs breakthrough curves in Figure 2-9 assume only a single type of sorption site on both the FFM and the colloids. However, the FFM sorption site was allowed to have a different

desorption rate constant once the Cs and colloid injection pulse ended so that the hysteretic sorption behavior could be simulated. Changing the desorption rate constant effectively changed the  $K_d$  value because the  $K_d$  value is the ratio of the adsorption to the desorption rate constants. This adjustment is

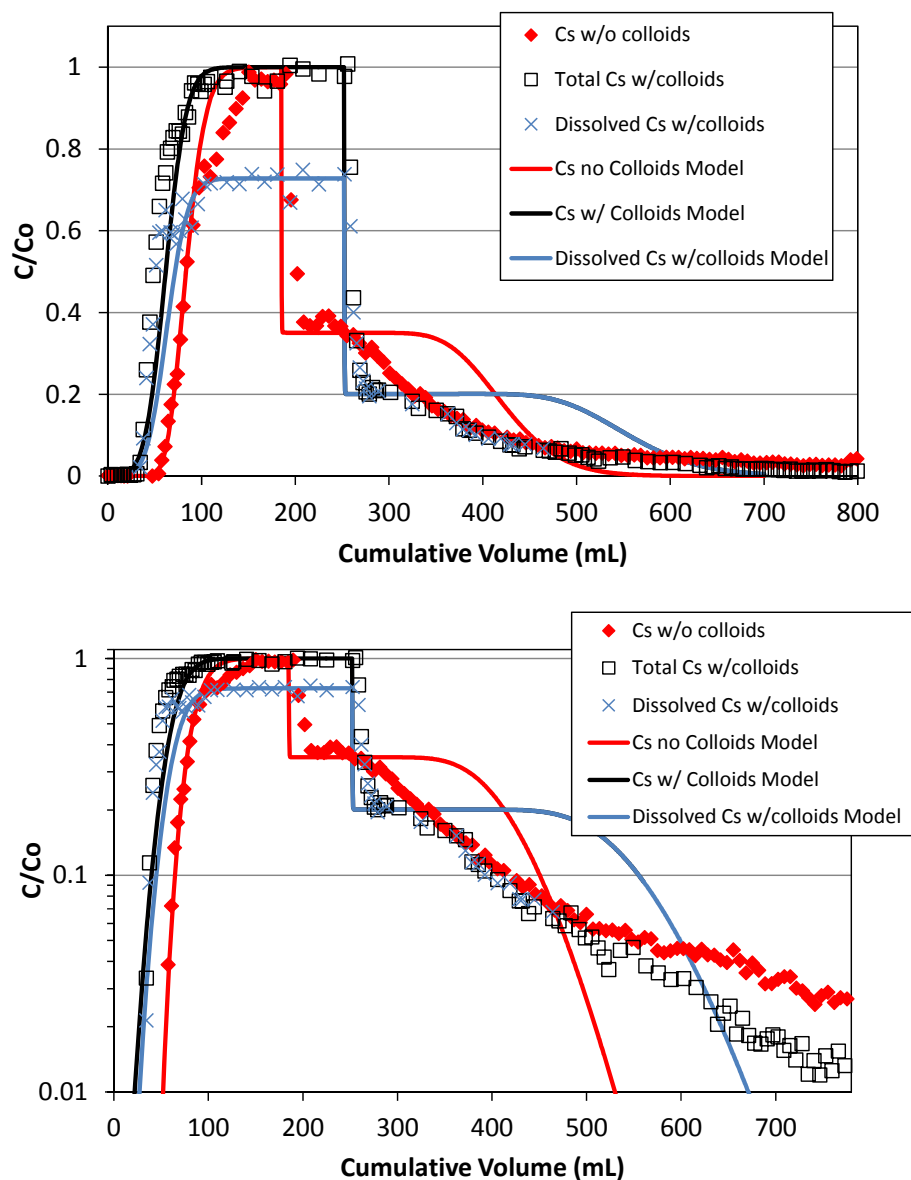


Figure 2-9. Normalized breakthrough curves of  $^{137}\text{Cs}$  in column experiments with and without colloids in the injection pulse (top – linear concentration scale; bottom - log concentration scale). Lines are model matches to the data assuming only a single type of sorption site on both the colloids and the FFM. Note that the injection pulses ended when the model curves show sudden drops in concentration.  $^3\text{HHO}$  and colloid breakthrough curves are not shown, but the colloids essentially mirrored the  $^3\text{HHO}$  curves and showed no evidence of any filtration. Model parameters are listed in Tables 2-5 and 2-6.

consistent with the hysteretic behavior observed in the batch sorption and desorption tests; in fact, it was initially assumed that the  $K_d$  values during adsorption and desorption in the column experiments were equal to the values deduced from the corresponding batch tests (with the desorption  $K_d$  value taken to be the  $K_d$  value observed at the end of the first batch desorption experiment, not the second one). These values were adjusted only slightly to achieve better matches to the column data.

It is apparent in Figure 2-9 that while the initial arrival and rising portion of the Cs breakthrough curves were matched reasonably well with a single sorption site, the desorption portions of the curves were poorly matched. The observed sudden drop in concentration at the end of the injection pulse can be matched quite well by adjusting the desorption rate constant. However, the larger desorption  $K_d$  value also results in a relatively steady concentration plateau for a much longer time than observed in the data, and then there is a much more rapid decline in concentration than the observed late-time tailing behavior. It should be noted that the  $K_d$  value for Cs partitioning to the bentonite colloids was fixed in all column simulations to be exactly that observed in the prepared colloid suspensions, i.e., 3700 ml/g. The rate constants for Cs partitioning to the colloids were allowed to vary to achieve better fits to the column data, but the ratio of the rate constants was fixed to be equal to the observed  $K_d$  value. The main constraint was that the rates had to exceed a lower threshold to avoid unrealistically early breakthrough of colloid-associated Cs.

As the model curves of Figure 2-9 suggest, it was not possible to obtain a reasonable match to the Cs tailing behavior in the column experiments using a single sorption site. Decreasing the desorption  $K_d$  value resulted in increasing the height of the concentration plateau, shortening the plateau, and steepening the eventual decline in concentration relative to the curves shown in Figure 2-9. Increasing the desorption  $K_d$  value had the opposite effect: it lowered and lengthened the plateau, and although it decreased the steepness of the eventual concentration decline, the decline was still considerably faster than the observed data. Attempts to manipulate the adsorption and desorption rate constants while keeping their ratios the same (i.e., keeping  $K_d$  values fixed) only marginally improved the matches to the desorption portion of the breakthrough curves, but it degraded the matches to the rising portion of the curves. The adsorption and desorption rate constants yielding the model curves of Figure 2-9 were used to obtain the one-site model curves for the batch experiments shown in Figures 2-6 and 2-7. It is apparent that these values provided reasonably good approximate matches to the batch data, although the rate constants that were assumed in the column experiments to avoid early breakthrough of Cs were clearly too fast to match the batch data.

Figure 2-10 shows the results of matching a two-site model (on both the FFM and colloids) to the column experiment Cs breakthrough curves with and without colloids present in the injection pulse. It is obvious that the two-site model offers a significant improvement over the one-site model, especially during the desorption portion of the column experiments. The inclusion of a second site with slower adsorption and desorption kinetics than the first site allows the Cs tailing behavior to be much better matched than when only a single site is allowed. Some discrepancies between the model and data remain in the early part of the desorption portion of the breakthrough curves, but these could be reduced by including a third sorption site on the FFM. We did not attempt to include a third site because we felt that the two-site model effectively captured the main features of the breakthrough curves. The adsorption and desorption rate constants and the sorption site capacities on the FFM yielding the model curves of Figure 2-10 are listed in Table 2-5. The one-site model parameters corresponding to the curves of Figure 2-9 are also listed in Table 2-5. The parameters of Table 2-5 were used to obtain the batch experiment model curves of Figures 2-6 and 2-7. It is apparent in Figures 2-6 and 2-7 that the two-site model parameters yielding good matches to the column transport data provided much better matches to the batch data than the one-site model parameters.

The colloid sorption site parameters assumed in all the model runs to interpret the column experiments are listed in Table 2-6. In the case where only a single sorption site on the colloids was assumed (Figure 2-



9), the parameters for the second site were set to zero, but the same parameters were used for the first site regardless of whether a second site was assumed to be present or not.

It is worthwhile to make a couple of comments about the two-site model parameters of Tables 2-5 and 2-6. First, while a second sorption site is assumed on the colloids, this site has negligible impact on the model results because the capacity of the site is extremely small relative to the  $C_s$  concentrations in the experiments. The parameters of the second site were chosen to be consistent with the results of Missana

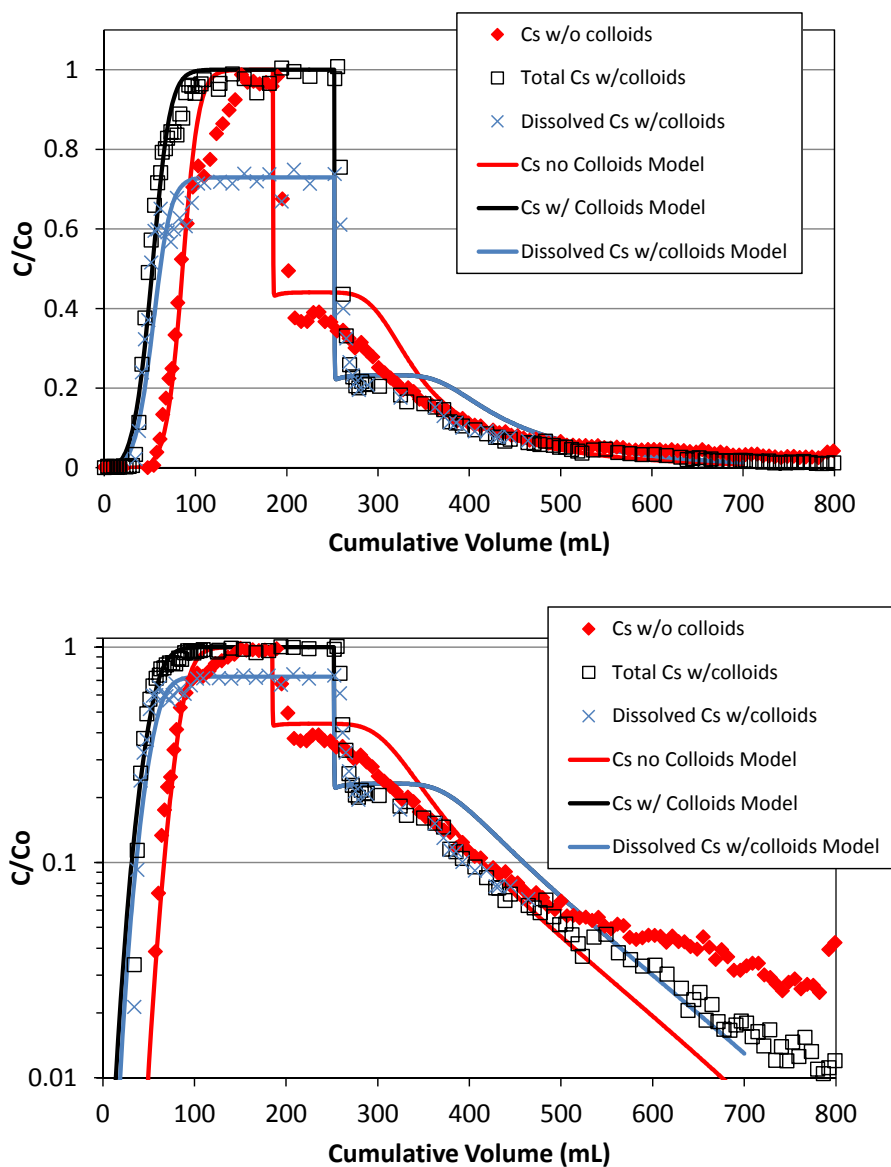


Figure 2-10. Normalized breakthrough curves of Figure 2-9 showing model matches to the data assuming two types of sorption sites on both the colloids and the FFM. Model parameters are listed in Tables 2-5 and 2-6.

et al. (2004), who noted a strong  $C_s$  sorption site with very low capacity on FEBEX bentonite colloids in Grimsel groundwater, which was not apparent until  $C_s$  concentrations decreased below about  $1e-8$  M (Figure 2-1). The effective  $K_d$  values on the colloids as a function of  $C_s$  concentration using the two-site

model parameters of Table 2-6 is shown in Figure 2-11; the similarity of this figure to Figure 2-1 is readily apparent.

Table 2-5. FFM sorption parameters yielding the model curves shown in Figures 2-9, 2-10, and 2-12.

<b>Cs Transport with No Colloids</b>						
<b>Parameter</b>	<b>Figure 2-9 (1 site)</b>		<b>Figure 2-10 (2 sites)</b>		<b>Figure 2-12 (2 sites)</b>	
	<b>Ads.</b>	<b>Des.</b>	<b>Ads.</b>	<b>Des.</b>	<b>Ads.</b>	<b>Des.</b>
Sorption rate constant, 1 <sup>st</sup> site (ml/g-hr)	102	102	50	50	--	--
Desorption rate constant, 1 <sup>st</sup> site (1/hr)	2	0.7	1.4	0.6	--	--
Max. site capacity, 1 <sup>st</sup> site (mol/g)	1e-5	1e-5	1e-5	1e-5	--	--
Sorption rate constant, 2 <sup>nd</sup> site (ml/g-hr)	--	--	1.02	1.02	--	--
Desorption rate constant, 2 <sup>nd</sup> site (1/hr)	--	--	0.014	0.008	--	--
Max. site capacity, 2 <sup>nd</sup> site (mol/g)	--	--	4e-8	4e-8	--	--
<b>Cs Transport with Colloids</b>						
<b>Parameter</b>	<b>Figure 2-9 (1 site)</b>		<b>Figure 2-10 (2 sites)</b>		<b>Figure 2-12 (2 sites)</b>	
	<b>Ads.</b>	<b>Des.</b>	<b>Ads.</b>	<b>Des.</b>	<b>Ads.</b>	<b>Des.</b>
Sorption rate constant, 1 <sup>st</sup> site (ml/g-hr)	102	102	50	50	50	50
Desorption rate constant, 1 <sup>st</sup> site (1/hr)	2	0.55	2	0.6	2	0.8
Max. site capacity, 1 <sup>st</sup> site (mol/g)	1e-5	1e-5	1e-5	1e-5	1e-5	1e-5
Sorption rate constant, 2 <sup>nd</sup> site (ml/g-hr)	--	--	1.02	1.02	1.02	1.02
Desorption rate constant, 2 <sup>nd</sup> site (1/hr)	--	--	0.02	0.008	0.02	0.011
Max. site capacity, 2 <sup>nd</sup> site (mol/g)	--	--	4e-8	4e-8	4e-8	4e-8

Note: Grey-shaded cells highlight increases in desorption rate constants in the presence of colloids during the adsorption phase of Figure 2-10 experiments (when colloids were present during adsorption phase), and green-shaded cells highlight increases in desorption rate constants in the presence of colloids during the desorption phase of Figure 2-12 experiment (vs. Figure 2-10 experiment where colloids were not present during desorption). Rate constants for the 1-site model (Figure 2-9) were adjusted to achieve good matches to the data without consideration of the presence or absence of colloids.

Table 2-6. Colloid sorption parameters used in all model simulations.

<b>Parameter</b>	<b>Value</b>
Sorption rate constant, 1 <sup>st</sup> site (ml/g-hr)	29600
Desorption rate constant, 1 <sup>st</sup> site (1/hr)	8
Max. site capacity, 1 <sup>st</sup> site (mol/g)	1e-3
Sorption rate constant, 2 <sup>nd</sup> site (ml/g-hr)	59200
Desorption rate constant, 2 <sup>nd</sup> site (1/hr)	0.4
Max. site capacity, 2 <sup>nd</sup> site (mol/g)	6e-8
$K_d$ value, 1 <sup>st</sup> site	3700
$K_d$ value, 2 <sup>nd</sup> site	148000

A second comment about the two-site model parameters of Tables 2-5 and 2-6 is that slightly larger desorption rate constants from the FFM (Table 2-6) were assumed during the adsorption portion of the column experiment with colloids than during the adsorption portion of the experiment without colloids. This adjustment was not arbitrary; it was made to honor the larger apparent desorption rate of Cs from the FFM in the presence of colloids than in the absence of colloids in the second batch desorption experiment (Figure 2-8). The relative difference in the desorption rate constants was approximately the same as that necessary to explain the difference in the two desorption data sets of Figure 2-8.

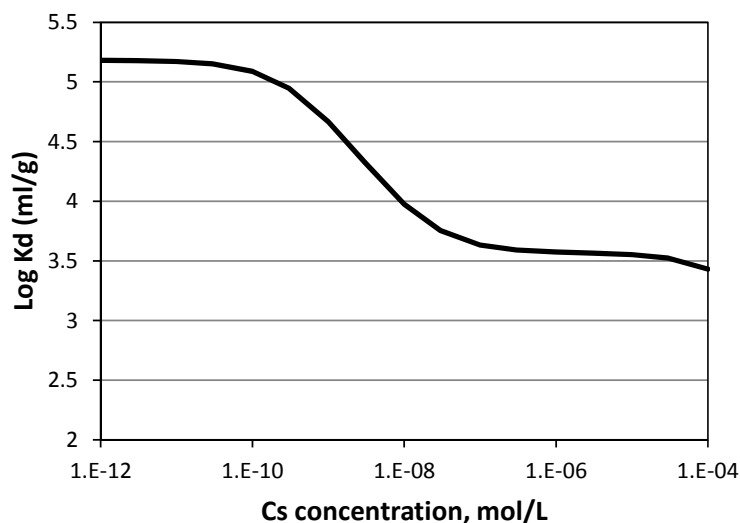


Figure 2-11. Cs  $K_d$  values on colloids as a function of Cs concentration using the sorption parameters of Table 2-6.

Figure 2-12 shows the breakthrough curves in the experiment in which a portion of the effluent from the column experiment containing colloids was injected into a second column. In this experiment, colloids continued to be injected after the end of the Cs injection pulse. This experiment was not modeled using a one-site model but rather was modeled using the same two-site model parameters as in the first column experiment involving colloids. The only difference in the model parameters between the two experiments was that a slightly larger Cs desorption rate constant from the FFM was assumed during the desorption portion of the second experiment to account for the increased desorption rate from the FFM in the presence of colloids (there were no colloids present during the desorption portion of the first experiment). It is apparent that there is good agreement between the model and data without any adjustment of the model parameters obtained from the first colloid experiment (other than the desorption rate constant adjustment to account for the presence of colloids during tailing in the second experiment). However, it is also apparent that if the model had been extended to longer times, it would have been necessary to include a third sorption site on the FFM to effectively capture the late-time tailing behavior.

An intriguing result of the second experiment was that the ratio of dissolved Cs to total Cs exiting the column became increasingly smaller as the tailing portion of the experiment progressed. Figure 2-13 shows this ratio as a function of eluted volume during the experiment, and Figure 2-14 shows the fraction as a function of total Cs concentration exiting the column, irrespective of time or volume eluted. These results are consistent with a second and stronger sorption site on the colloids that is just beginning to exert its influence as Cs concentrations decrease late in the experiment. That is, it is consistent with the results of Missana et al. (2004) that show evidence for a strong sorption site with low site abundance on the bentonite colloids that is apparent only at low Cs concentrations. The model curves of Figure 2-12 actually reflect a minor decrease in the ratio of dissolved to total Cs late in the experiment because of the inclusion of a second stronger sorption site on the colloids, but this decrease is not nearly as large as that observed in the experimental data.

Figure 2-15 shows the Cs recoveries as a function of volume eluted in each of the three column experiments. Over 90% of the Cs was recovered during each of the experiments, with the mass balance being closed to within a few percent by the final 0.1 M HCl flush. This flush confirmed that there was a small amount of remaining Cs in the columns at the end of each experiment.

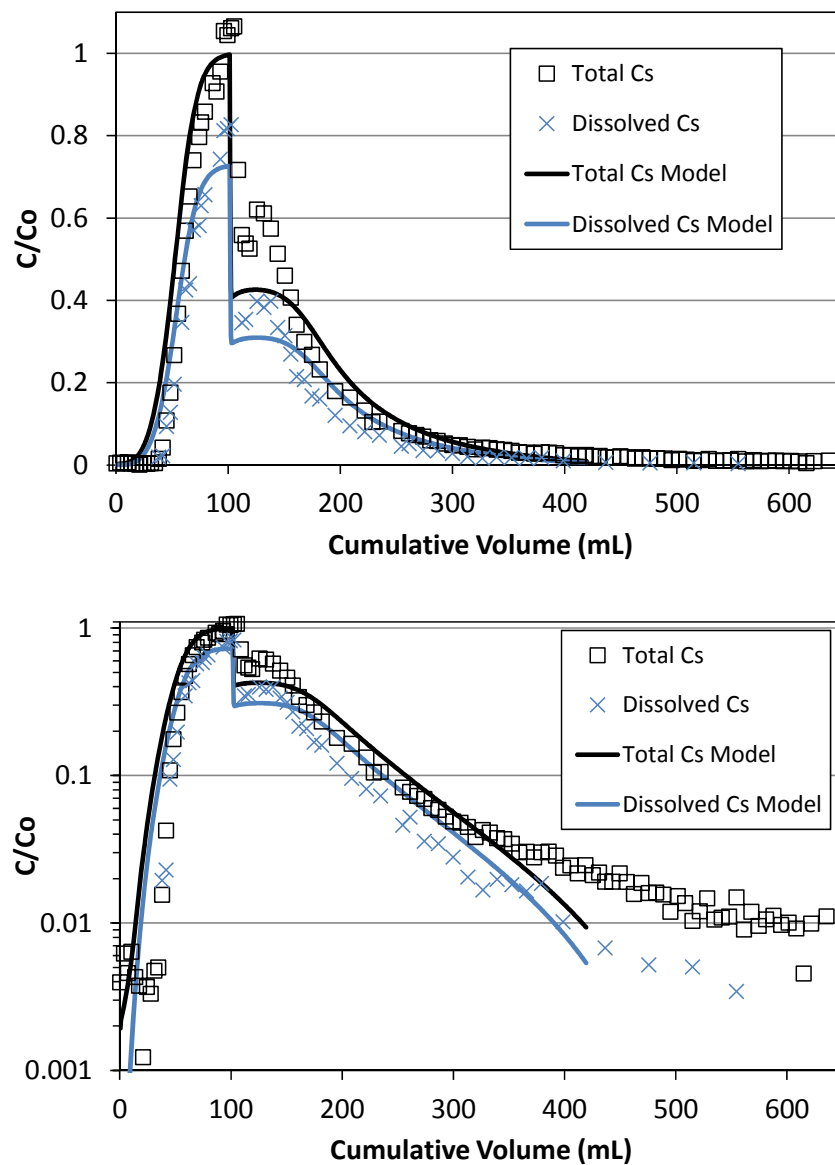


Figure 2-12. Normalized breakthrough curves of  $^{137}\text{Cs}$  in column experiment in which a portion of the effluent from the experiment with colloids shown in Figures 2-9 and 2-10 was passed through another column. Colloids continued to be injected through the column even after the Cs pulse had ended. Lines are model matches to the data assuming two types of sorption sites on both the colloids and the FFM. Note that the Cs injection pulse ended when the two model curves show sudden drops in concentration.  $^3\text{HHO}$  and colloid breakthrough curves are not shown, but the colloids essentially mirrored the  $^3\text{HHO}$  curves and showed no evidence of any filtration. Model parameters are listed in Tables 2-5 and 2-6.

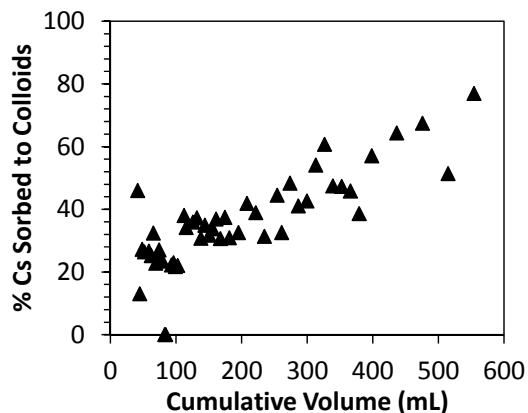


Figure 2-13. Fraction of Cs sorbed to colloids a function volume eluted in the experiments of Figure 2-12.

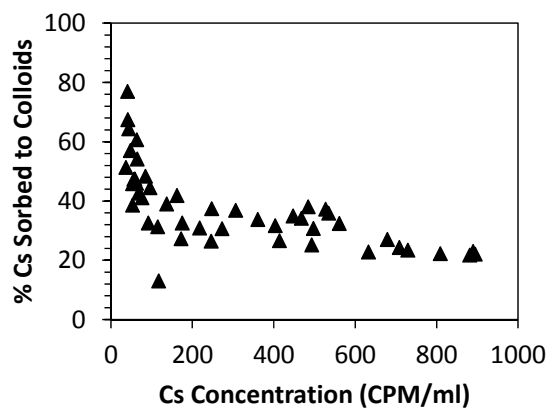


Figure 2-14. Fraction of Cs sorbed to colloids a function of Cs concentration in the experiments of Figure 2-12. Note that 50 CPM/ml is equivalent to about  $5e-8$  M total Cs concentration.

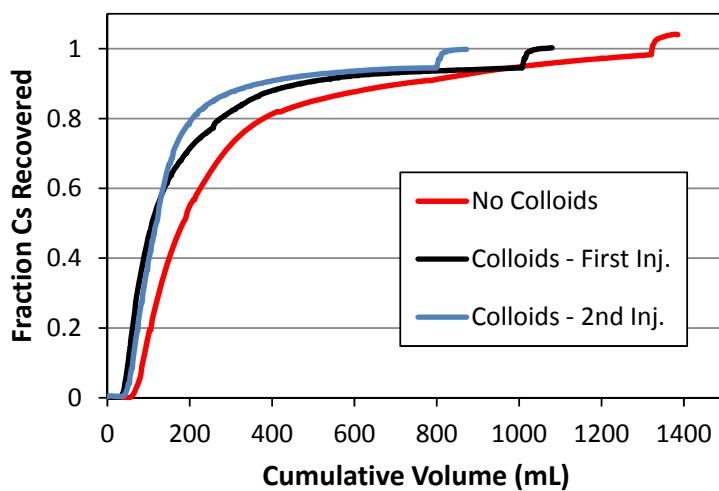


Figure 2-15. Fraction of Cs recovered in each of the column experiments.

### 2.4.3 Implications for Repository Performance Assessments

The implications of the batch and column experiments in this study are that Cs radioisotopes appear unlikely to transport over significant time and distance scales in association with bentonite colloids *unless* steady-state mobile colloid concentrations are quite high. Although Cs partitioning to the bentonite colloids is quite strong, the sorption process appears to be reversible, with the desorption kinetics being rapid enough that Cs would be expected to completely dissociate from mobile colloids over long time and distance scales that are relevant to repository performance assessments. We hasten to point out that greater facilitation of Cs transport by bentonite colloids would be expected if Cs concentrations were lower than in our experiments because of the stronger partitioning of Cs to the colloids at lower concentrations (observed by Missana et al., 2004, and also evident at late times in our second Cs/colloid column experiment). This greater Cs partitioning and slower desorption rates from bentonite colloids at lower Cs concentrations may have been responsible for the much greater apparent (relative to our experiments) colloid-facilitated transport of Cs in a 2012 GTS field transport experiment (described in Wang et al., 2013), and in a 2002 GTS field experiment (Geckeis et al., 2004; Möri, 2004). In those field experiments, which were conducted in nominally the same geochemical system as our experiments, the colloid concentrations were comparable to ours (~100 mg/L), but the Cs concentrations were less than 1e-9 M, as opposed to about 1e-6 M in our experiments. The much lower Cs concentrations (due to the lack of non-radioactive carrier Cs associated with the <sup>137</sup>Cs) would have resulted in significantly stronger Cs partitioning to the colloids than in our experiments because of the much greater influence of the low-abundance strong sorption sites on the colloids at these lower Cs concentrations.

Under our experimental conditions of near-equilibrium Cs partitioning to both colloids and stationary media, as well as the nearly constant mobile colloid concentrations, the 1-D transport equation describing colloid-facilitated solute transport can be reduced to:

$$\frac{\partial C}{\partial t} + v_f \frac{\partial C}{\partial x} - D_c \frac{\partial^2 C}{\partial x^2} + \frac{\rho_f}{\eta} K_d \frac{\partial C}{\partial t} + K_c C_{col} \frac{\partial C}{\partial t} + v_f K_c C_{col} \frac{\partial C}{\partial x} = 0 \quad (2-13)$$

which can be further simplified to:

$$\left(1 + \frac{\rho_f}{\eta} K_d + K_c C_{col}\right) \frac{\partial C}{\partial t} + (1 + K_c C_{col}) v_f \frac{\partial C}{\partial x} - D_c \frac{\partial^2 C}{\partial x^2} = 0 \quad (2-14)$$

where  $K_c$  = equilibrium partition coefficient of the solute to the colloids, ml/g.

Equation (14) implies an effective solute velocity of  $(1 + K_c C_{col}) v_f$  with a retardation factor of

$1 + \frac{\rho_f}{\eta} K_d + K_c C_{col}$ , so the overall effective retardation factor of the solute in the presence of the colloids,  $R_c$ , becomes:

$$R_c = \frac{1 + \frac{\rho_f}{\eta} K_d + K_c C_{col}}{1 + K_c C_{col}} \quad (2-15)$$

Figure 2-16 shows the result of applying this simple expression in an analytical solution of 1-D advection-dispersion equation to predict the rising portion of the breakthrough curves of Figures 2-9 and 2-10. The measured values of  $K_d$  and  $K_c$  from the batch sorption experiments and the known colloid concentrations in the column experiments were used to calculate the colloid-facilitated transport retardation factor (eq. 2-15)

and also the solute-only retardation factor,  $R = 1 + \frac{\rho_f}{\eta} K_d$ . It is apparent that these simple retardation

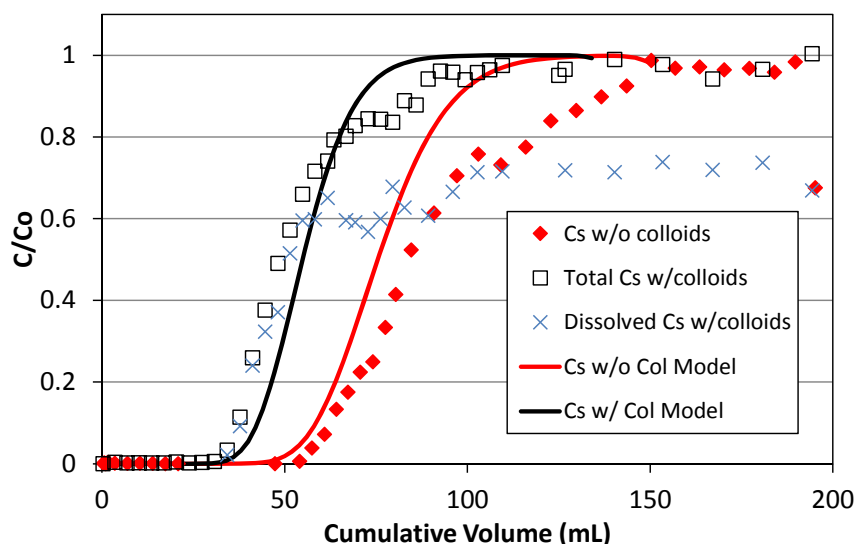


Figure 2-16. Predictions of the rising portion of the Cs breakthrough curves of Figures 2-9 and 2-10 using eq. (2-15) as a retardation factor for colloid-facilitated transport in an analytical solution of 1-D advection-dispersion equation. The  $K_d$  and  $K_c$  values from the batch experiments were used in eq. (2-15).

factors provide good predictions of the Cs breakthroughs in the column experiments. The analytical solution cannot be used to predict the desorption portion of the breakthrough curves because of the sorption-desorption hysteresis. Nevertheless, when solute partitioning to mobile colloids and immobile surfaces are fast and colloid concentrations are relatively constant, the retardation factor of eq. (15) can serve as a good approximation to estimate the potential for colloid-facilitated transport. Typically the

value of  $K_c C_{col}$  will be small compared to the value of  $\frac{\rho_f}{\eta} K_d$  in the numerator of eq. (2-15) (in our experiments  $K_c C_{col}$  was  $\sim 0.37$  compared to about 200 for  $\frac{\rho_f}{\eta} K_d$ ) because  $C_{col}$  is usually very small

relative to  $\frac{\rho_f}{\eta}$ , so the main effect of the presence of colloids is in the denominator of eq. (2-15), where

$K_c C_{col}$  must be greater than about 0.1 to have a significant impact on solute transport relative to transport in the absence of colloids.

## 2.5 Conclusions and Future Work

In this study, we demonstrate how a combination of batch sorption/desorption experiments and column transport experiments were used to effectively parameterize a model describing the colloid-facilitated transport of Cs in the Grimsel granodiorite/FFM system. Cs partition coefficient estimates onto both the colloids and the stationary media obtained from the batch experiments were used as initial estimates of partition coefficients in the column experiments, and then the column experiment results were used to obtain refined estimates of the number of different sorption sites and the adsorption and desorption rate constants of the sites. The desorption portion of the column breakthrough curves highlighted the importance of accounting for adsorption-desorption hysteresis (or a very nonlinear adsorption isotherm) of the Cs on the FFM in the model, and this portion of the breakthrough curves also dictated that there be at least two different types of sorption sites on the FFM. In the end, the two-site model parameters

estimated from the column experiments provided excellent matches to the batch adsorption/desorption data, which provided a measure of assurance in the validity of the model.

It was also demonstrated how a relatively simple retardation factor expression could be used to provide a good approximation of colloid-facilitated solute transport under conditions of near-constant mobile colloid concentrations and rapid and reversible solute sorption/desorption onto both the colloids and immobile surfaces. This expression provided a very good approximation to the column breakthrough curves using the partition coefficients observed in the batch experiments and the known colloid concentrations in the column experiments.

For future work, the model developed in this study will be applied to do a forward prediction of the Cs breakthrough curve in the 2012 colloid-facilitated transport experiment at the GTS. A previous interpretation of this experiment (Wang et al., 2013) indicated that Cs transported much differently than in the laboratory experiments of this study. Desorption of Cs from the colloids in the field test was much slower than in the laboratory tests, resulting in an essentially unretarded breakthrough of a fraction of the injected Cs. There was no unretarded Cs transport in the lab column experiments despite the fact that the lab experiments had shorter residence times than in the field. The Cs partition coefficient to the colloids that provided a good match to the field Cs breakthrough curve was larger than for the stronger of the two sites in the laboratory-based model. However, it must be kept in mind that the Cs concentrations in the field experiment were lower than in the laboratory experiments by about three orders of magnitude, which would have increased the influence of the stronger sorption sites on the colloids. A goal of the future effort will be to refine the model and model parameters developed here to allow the model to explain both the laboratory and field Cs transport data. The key to this effort will be making adjustments to the parameters of the stronger of the two sorption sites on the colloids so that the strong site can account for essentially all of the Cs transport observed in the field test while the weaker site still accounts for most of the Cs transport observed in the laboratory tests. It may also be necessary to introduce an additional site to the model.

Additional future work for the Used Fuel Disposition Campaign (UFDC) in FY 2016 will include a comprehensive evaluation report on the state of knowledge of colloid-facilitated radionuclide transport as it applies to repository performance assessments. This effort will include interactions with performance assessment modelers on the project to develop an approach to efficiently account for colloid-facilitated transport in repository performance assessments. The evaluation report will include a summary of the results from this study as well as previous work in the UFDC program on the colloid-facilitated transport of americium in the Grimsel granodiorite system and the association of plutonium with intrinsic colloids (efforts at Lawrence Livermore National Laboratory), and it will also summarize and incorporate the results of field colloid-facilitated transport experiments at the GTS. The report will also draw heavily from numerous studies conducted outside the UFDC over the past 20+ years. A major emphasis of the report will be on how the collective observations and knowledge of colloid-facilitated radionuclide transport can be effectively upscaled to time and distance scales relevant to repository performance assessments.

## 2.6 References

- Bertetti, F.P., Klar, R.V., and Vaught, M.M. (2006) *Colloid-Facilitated Transport of Radionuclides in Natural Groundwater Systems – Literature Review*. Report prepared for U.S. Nuclear Regulatory Commission by Center for Nuclear Waste Regulatory Analysis, San Antonio, TX.
- Dittrich, T. Gable, C.W., Hyman, J., Karra, S., Makedonska, N., Painter, S.L. and Reimus, P.W. (2014) Crystalline and Crystalline International Disposal Activities, Chapters 4 and 6, *FCRD-UFD-2014-000495*, prepared for Used Fuel Disposition Campaign of Fuel Cycle Research and Development, Los Alamos National Laboratory, Los Alamos, NM.



- Dittrich, T.M. and Reimus, P.W. (2015) Uranium transport in a crushed granodiorite: Experiments and reactive transport modeling. *J. Contam. Hydrol.* 175-176, 44-59. doi: 10.1016/j.jconhyd.2015.02.004.
- Dittrich, T.M., Boukhalfa, H., Ware, S.D., and Reimus, P.W. (2015a) Laboratory investigation of the role of desorption kinetics on americium transport associated with bentonite colloids. *J. Environ. Radioactiv.* 148, 170-182. doi: 10.1016/j.jenvrad.2015.07.001.
- Dittrich, T.M., Ware, S.D., and Reimus, P.W. (2015b) Mini-columns for conducting breakthrough experiments: Design and construction. *LA-UR-15-24392*; Los Alamos National Laboratory, Los Alamos, NM. doi: 10.2172/1184604.
- Geckeis, H., Schäfer, T., Hauser, W., Rabung, Th., Missana, T., Degueudre, C., Möri, A., Eikenberg, J., Fierz, Th., and Alexander, W. (2004) Results of the colloid and radionuclide retention experiment (CRR) at the Grimsel Test Site (GTS), Switzerland – impact of reaction kinetics and speciation on radionuclide migration. *Radiochim. Acta.*, 92, 765-774.
- Grolimund, D., Barmettler, K., and Borkevic, M. (2007) Colloid-facilitated transport in natural porous media: Fundamental phenomena and modelling, in *Colloid Transport in Porous Media*, Frimmel, F., von der Kammer, F, and Flemming, H-C., eds., Springer, Berlin, Germany.
- Grolimund, D., and Borkevic, M. (2005) Colloid-facilitated transport of strongly sorbing contaminants in natural porous media: Mathematical modeling and laboratory column experiments, *Environ. Sci. Technol.*, 39, 6378-6386.
- Huber, F., Kunze, P., Geckeis, H., and Schäfer, T. (2011) Sorption reversibility kinetics in the ternary system radiocluide-bentonite colloids/nanoparticles-granite fracture filling material. *Appl. Geochem.*, 26, 2226-2237.
- Iijima, K., Tomura, T., Tobita, M., and Suzuki, Y. (2010) Distribution of Cs and Am in the solution-bentonite colloids-granite ternary system: effect of addition order and sorption reversibility. *Radiochim. Acta* 98, 729-736.
- Iijima, K., Shoji, Y., and Tomura, T. (2008) Sorption behavior of americium onto bentonite colloid. *Radiochim. Acta*, 96, 721-730.
- Kanti, S.T. and Khilar, K.C. (2006) Review on subsurface colloids and colloid-associated contaminant transport in saturated porous media, *Adv. Colloid. Interface Sci.*, 119(2-3), 71-96.
- Kersting, A. B. and P. W. Reimus, eds. 2003. “Colloid-Facilitated Transport of Low-Solubility Radionuclides: A Field, Experimental, and Modeling Investigation,” *UCRL-ID-149688*, Lawrence Livermore National Laboratory, Livermore, CA.
- Murali, M., and Mathur, J. (2002) Sorption characteristics of Am(III), Sr(II) and Cs(I) on bentonite and granite. *J. Radioanal. Nucl. Ch.* 254(1), 129-136.
- Painter, S., Cvetkovic, V., Pickett, D. and Turner, D.R. (2002) Significance of kinetics for sorption on inorganic colloids: Modeling and experiment interpretation issues, *Environ. Sci. Technol.*, 36, 5369-5375.
- Wang, Y., et al. (2013) Natural System Evaluation and Tool Development – International Collaborations: FY13 Progress Report, Used Fuel Disposition Campaign Milestone Report *FCRD-UFD-2013-000628*; Chapter 2, Interpretations of Colloid-Facilitated Transport Experiments at the Grimsel Test Site from 2008 through 2012.